This is to certify that the
dissertation entitled

Proximity Effect in Ferromagnet/Superconductor Hybrid Systems

presented by

Ion Cătălin Moraru

has been accepted towards fulfillment
of the requirements for the

Ph.D. degree in Physics and Astronomy

Norman O. Birge

Major Professor's Signature

July 21, 2006

Date

MSU is an Affirmative Action/Equal Opportunity Institution

Proximity Effect in Ferromagnet/Superconductor Hybrid Systems

By

Ion Cătălin Moraru

A DISSERTATION

Submitted to
Michigan State University
in partial fulfillment of the requirements
for the Degree of

DOCTOR OF PHILOSOPHY

Department of Physics and Astronomy

2006

ABSTRACT

Proximity Effect in Ferromagnet/Superconducor Hybrid Systems

By

Ion C. Moraru

The bulk of this thesis deals with proximity effects resulting from placing a ferromagnet (F) in contact with a superconductor (S). The hybrid structure combines conventional superconductivity, which brings about the coupling of electrons with opposite spins, with ferromagnetism, which favors the parallel alignment of electron spins. The superconducting correlations penetrate inside the ferromagnet over a length scale that depends upon its strength. In addition to its decay, the propagation of the order parameter is spatially modulated by the energy difference between the minority and majority spin bands.

There are several experimental consequences arising from the competing symmetries, including the reduction in the superconducting transition temperature, T_C. The degree of suppression is directly related to the material thicknesses and the quality of the interface that they form. We have performed T_C measurements on several F/S/F trilayer structures with strong ferromagnets. The results yielded slight differences in T_C based on whether the magnetization of the ferromagnet are oriented parallel (P) or anti-parallel (AP), with the latter exhibiting a slightly higher T_C.

The sensitivity of a superconductor to the magnetic orientation of its contacting ferromagnet lies at the heart of a theoretical prediction for the existence of a triplet paring mechanism in a conventional superconductor. Surrounding a superconductor with ferromagnets having non-collinear magnetization is theoretically shown to induce triplet state correlations that extend out to distances much longer than those reached by the conventional singlet state. Using strong ferromagnets, our F/S/F measurements have laid the foundation for systems that may exhibit triplet pairing.

To the reader

Acknowledgments

There are many people who have contributed, both professionally and personally, to the various aspects surrounding this thesis.

The largest number of thanks go to my advisor, Dr. Norman Birge. It has been a pleasure to receive your wisdom, vote of confidence, financial support and concert tickets. I have enjoyed our interactions in the environment that you created, which allowed for freedom of expression and scientific latitude. In addition, I would like to thank Dr. Bill Pratt for the many discussions and expert experimental suggestions that helped me learn the tricks of the trade.

I want to thank my family the best way I know how: Vreau să mulţumesc părinţilor mei, Aura (-Da, am mincat) şi Vladimir (-Vezi tată, sunt mai mult de patru pagini), surorii mele Mădă, şi cumnatului meu Mikie, pentru acoperiş, mîncare, apă caldă, şi rufe curate. Acum presupun că vor incepe salatele sa curgă. Includ in mulţumiri toate rudele şi neamurile care m-au susţinut în spirit de peste hotare.

I would like to thank Dr. Reza Loloee for his support and enormous contribution to my technical expertise with respect to sample fabrication and measurement. I would also like to extend my thanks to Dr. Jack Bass and Dr. Stuart Tessmer for the REU experience that convinced me to make Michigan State University my home.

Many thanks to Sergei Urazhdin, with the ever-present chant of "you've got to do it," and the sportive battles. Michael Crosser, thanks for returning the favor. I feel that we were comrade-in-arms until the last. Gassem Al-zoubi, holding down the fort together was nice. Mustafa al-Haj Darwhish, I have enjoyed tremendously our many philosophical moments that transcended the experimental world. Huseyin Kurt, I know you do know this, but thanks for the games, conversations, and lunches. Toni Zambano, your contribution to my abilities in Spanish is irreplaceable. Amit Sharma, your smiling presence in the office over the last stretch of this thesis made it bearable. "Do you know, what I want to say, to you?" Nineta Theodoropoulou, I

have enjoyed our coffee-break conversations in between the madness and I hope you enjoyed mine.

Special thanks go to Tom Palazzolo, Jim Muns and Tom Hudson for putting up with my shenanigans and allowing me free reign on the professional side of the machine shop, even when I was "eyeball-ing" it. You have helped me discover the machine-tooled world around me. In addition, invaluable was the work of our graduate secretaries, Debbie, Laura, Cathy and Lisa, especially when I needed a band-aid for my chin, a friendly conversation, or a free chocolate break.

Contents

List of Figures

List of Tables

Chapter 1

Introduction

The Ferromagnet/Superconductor (F/S) hybrid system has received a lot of theoretical and experimental attention given the complexities associated with the competing symmetries of order parameters, which continue to offer surprising and interesting results. The superconducting correlations that are present in the superconductor enter the ferromagnet with which it makes contact, similarly to the way they do in Normal/Superconductor systems. However, the extent of the penetration is much shorter, since the effective field set by the magnetization of the ferromagnet breaks the superconducting Cooper pairs, which consist of electrons with opposite spin directions. In addition, the superconducting order parameter has an oscillatory spatial modulation inside the ferromagnet over the same length scale, containing nodes in which the phase changes by π. The physical origin of the oscillations comes from the inherent energy difference between the different spin bands in the ferromagnet. Several reviews on the F/S system have appeared in literature [1, 2, 3, 4, 5] summarizing the various physical implications resulting from the combination of these very different materials.

Historically, the study of the F/S proximity effect goes back to the 1960's with the work of Hauser *et al.* [6]. Since then, a variety F/S systems have been studied in bilayer, trilayer and multilayer heterostructures. Several ferromagnetic materials

have been utilized including Fe, Ni, Co Gd, NiFe and various weakly ferromagnetic alloys. For the superconductors, Nb, Pb, V and Al are typical in experiments (for a review see [2] and references therein). Compared to a bare layer, an important consequence of placing a ferromagnet next to a superconductor is that its critical temperature, T_C, is suppressed to a degree that depends on the thickness of both materials. However, the exact behavior observed experimentally has varied in the literature. One of the main issues of discrepancy has stemmed from the observation of different dependence of the T_C based on the thickness of the ferromagnet in the structures where the thickness of the superconductor was kept constant [7, 8, 9, 10, 11]. Depending on the particular material system studied, rapid or gradual decay, monotonic fall-off, oscillations and even a re-entrant effect was observed as a function of the F layer thickness. The re-entrant effect refers to the complete disappearance of superconductivity for a certain thickness ferromagnet before returning for larger thicknesses. Based on this observation, there were claims that the non-monotonic behavior is due to the oscillatory nature of the condensate that penetrates inside the ferromagnet [7]. In other experiments [9], however, it was shown that it was the interface transparency that dominated the observed T_C behavior. Nonetheless, it was later recognized that the method and conditions during deposition are important as they determine the local structure and properties at the interface between the two materials.

The oscillating nature of the order parameter has several important theoretical and experimental consequences. The presence of superconducting correlations in the ferromagnet alters its density of states (DOS) over the same length scale as the penetration of Cooper pairs [12]. More specifically, for positive values of the order parameter, the DOS has a gap-like feature at zero energy. At distances further away from the interface the order parameter becomes negative, which results in an inverted DOS feature with a smaller amplitude. This behavior has been verified by

tunnel spectroscopy experiments [13], which measured the spatial variation of the ferromagnet DOS with respect to the interface by studying S/F bilayers with various thickness ferromagnets.

Another important effect resulting from the oscillation of the order parameter is the observed behavior in so-called Josephson junctions (JJ). In 1962 Josephson [14] made the prediction that a zero voltage supercurrent, $I_S = I_C \sin \Delta\phi$, flows between two superconducting electrodes when they separated by a thin insulating barrier. The critical current, I_C, is the maximum super-current that the junction can sustain and $\Delta\phi$ is the phase difference between the superconductors. In addition, if a voltage is maintained across the junction, the phase difference evolves according to $d(\Delta\phi)/dt = 2eV/\hbar$. Since the original prediction, an immense body of work has extended the JJ behavior to include weakly coupled superconductors, such as Superconductor-constriction-Superconductor and S/N/S systems, whose critical current depends on temperature, junction type and dimensions. The overlap of the order parameter from both superconductors allows a zero-voltage Josephson coupling between them.

Similarly, a Josephson current can be obtained by placing a sufficiently thin ferromagnet between two superconductors. Theoretically, the first prediction was made by Bulaevskii *et al.* [15] in 1977 for a system containing two superconductors separated by a region with magnetic impurities. It was later shown that a super-current can flow in an S/F/S structure [16]. Since then, a series of other treatments have studied its different aspects [17, 18, 19, 20, 21]. One important prediction resulting from the modulation of the order parameter in the ferromagnet is the existence of a $\pi-$ state. For that case, the ground state for the Josephson energy is attained when the phase difference between the two superconductors is π and not zero. This gives rise to a negative critical current and also an anomalous current-phase relation. A transition from the 0 to the π state leads to a zero crossing of I_C, and because only the absolute value is measured, this results in a sharp cusp in the I_C versus temperature or

ferromagnet thickness.

Experimental verification of the π state was slow to be realized, as the limited range of the superconducting correlations resulted in technical complications that needed to be overcome. The first successful report was given by Ryazanov *et al.* in 2001. By utilizing a weak ferromagnet, the penetration of the order parameter was extended, and the π state was observed as a function of temperature [22] as well as ferromagnet thickness [23]. Furthermore, a recent paper showed a transition from the 0 to the π state and then back to the 0 state [24] as a function of the ferromagnetic interlayer thickness.

1.1 This Work

Our original motivation for studying the F/S system has come from a series of experimental work that showed a long-range proximity effect where none was expected. Given that superconducting correlations cannot penetrate a ferromagnet over a large distance due to the pair-breaking effect of the exchange field, the experiments of Giroud *et al.* [25], Petrashov *et al.* [26] and Lawrence *et al.* [27] posed serious challenges to current theoretical understanding regarding the F/S proximity effect. Several groups [28, 29] attributed these results to the magnetic structure of the ferromagnets and included the effect of inhomogeneous magnetization present close the F/S interface in their models.

In an attempt to answer some of the open questions regarding the observed long-range proximity effect, we have designed an experiment that improved upon previous work by using a sample geometry that controls the magnetic structure of the ferromagnet in an F/S system. More specifically, due to the chosen sample shape one is capable of trapping a domain wall close to the F/S interface. A comparison between proximity effects in the presence of a domain wall can be then compared with those where the magnetization is homogeneous, and in so doing be able to unequivocally

ascertain the influence of inhomogeneous magnetization. In addition, recognizing that the quality of the interface between the F and S layers is critical, we have drawn upon previous methods utilized in obtaining good interface contact. Performing multiple-angle depositions without braking vacuum is one such technique, ensuring an interface free of contamination.

Technical difficulties, however, along with the appearance of a new and interesting opportunity in F/S systems shifted our efforts away from the long-range proximity effect experiments. In a new prediction by Bergeret *et al.* [29], the existence of a triplet pairing mechanism in conventional superconductors was shown to occur. In their work, the authors theoretically demonstrated that by having a superconductor surrounded by ferromagnets with non-collinear magnetization a triplet pairing mechanism is generated, which decays in the ferromagnet over a longer length scale as compared to that of the singlet (for a review see reference [3]). In this manner, a Josephson coupling based on the triplet correlations may be obtained in a F/S/F/S/F structure between the two superconductors [30], where the thickness of the inner ferromagnet extends beyond the penetration of the singlet Cooper pairs. Therefore, by changing the relative magnetization of adjacent ferromagnets from collinear and non-collinear, one should be able to reversibly transition between resistive and zero-voltage transport for bias currents that are less than I_C.

Initial experimental efforts using the Co/Nb system, however, yielded no evidence for the existence of the long-range penetration of the triplet state. However, no unambiguous conclusions could be drawn as to the validity of the prediction given the large number of variables. Based on the various experimental evidence on F/S systems, we quickly recognized that the many parameters influencing the degree to which the ferromagnetism affects superconductivity must be optimized in order to observe the predicted effect. In addition to finding a matching ferromagnet/superconductor pair that yields a good interface transparency, and hence a strong mutual influence, one

must also investigate the thickness dependencies that give a maximal signal.

One approach to this problem is to use the results of a simpler proximity effect experiment, namely critical temperature measurements of F/S/F systems. First performed by Gu *et al.* [11], a critical temperature difference can be observed based on whether the ferromagnet magnetizations are either parallel or antiparallel. Successful observation of this effect, however, requires that the thickness of the superconductor be thin enough to be sensitive to the relative magnetizations of the ferromagnets but thick enough so as not to completely suppress the superconducting transition temperature. Therefore, obtaining a null result in this much more simple experiment would indicate that the F/S system under study is not a good candidate for the triplet state experiment, as the latter relies on the sensitivity of the superconductor to the ferromagnet magnetization directions.

Chapter 2 of this thesis introduces the theoretical tools necessary for understanding the main mechanisms that describe F/S systems. Chapter 3 outlines the experimental techniques used throughout the entire thesis, including those used in early long-range proximity effect studies, sample fabrication methods for our F/S/F and triplet experiments. Chapter 4 gives the experimental results of our F/S/F experiments using the Ni/Nb [31] and NiFe/Nb systems. Chapter 5 outlines the application of current theoretical models to obtain fits to the data, according to Tagirov [32] and Fominov *et al* [33]. The latter chapter also describes the supplemental experiments needed to estimate values for the material parameters that are needed for the fits. Chapter 6 describes the progress achieved on the long-range proximity effect experiments with possible future directions. Chapter 7 explains the triplet state prediction by Bergeret *et al.* along with our efforts towards its experimental observation. Chapter 8 contains conclusions and closing remarks.

Chapter 2

Theoretical Background

Studying the proximity effect between a ferromagnet and a superconductor brings together two monumental fields with their very different mechanisms and subtleties. Although both topics rest on enormous bodies of work, they continue to challenge both theorists and experimentalists alike. This chapter will briefly review some of the concepts in ferromagnetism and superconductivity as they pertain to the treatment of F/S systems.

2.1 Length/Energy Scales

Mesoscopic physics studies systems whose dimensions lie in the range between those of macroscopic and quantum systems. One important length scale is the Fermi wavelength, λ_F, which is much shorter than any length scale in this regime. This allows for the treatment of transport properties in a semi-classical fashion. Another important concept is that of the elastic mean free time, τ, which is the time an electron spends undergoing several collisions without randomizing its momentum. This time determines a distance associated with the elastic scattering processes,

$$l_e = v_F \cdot \tau, \tag{2.1}$$

usually called the elastic mean free path, where v_F is the Fermi velocity. The size of l_e is determined by the specifics of the system under study. For thin films it is usually limited by the size of grain boundaries, imperfections, sample roughness and dimensions. A comparison between a system with a smallest dimension L in the direction of transport and l_e will determine whether it is ballistic or diffusive, namely

$$\lambda_F \ll L \ll l_e \quad \text{ballistic} \tag{2.2}$$

$$\lambda_F \ll l_e \ll L \quad \text{diffusive} \tag{2.3}$$

If L is much larger than l_e an electron will experience several collisions and will undergo random diffusive motion in the sample. Alternatively, if the sample size is smaller, then the electron will reach the boundaries of the sample without having lost its initial momentum. Usually, these ballistic systems are referred to as "clean" systems, whereas a system in which an electron undergoes diffusive motion is said to be "dirty."

In addition to elastic scattering there are also inelastic scattering events, resulting from electron-electron or electron-phonon interactions, which give phase relaxation on a time scale τ_ϕ. The distance traveled is then

$$\tau \sim \tau_\phi \quad L_\phi = v_F \cdot \tau_\phi \quad \text{ballistic} \tag{2.4}$$

$$\tau \ll \tau_\phi \quad L_\phi = \sqrt{D\,\tau_\phi} \quad \text{diffusive} \tag{2.5}$$

where $D = 1/3\, v_F\, l_e$ is the diffusion constant. The distance associated with maintaining phase coherence is termed the phase coherence length and it can be as large as a few microns at low temperatures.

The intrinsic spin of an electron introduces an additional degree of freedom, which translates into an effective travel distance before the orientation of the spin is completely randomized. Spin-orbit interactions and other mechanisms contribute to the

destruction of spin coherence and the distance that an electron covers while maintaining this coherence is termed the spin diffusion length, l_{sf}. This length scale becomes important in spin-dependent transport. One such example includes experiments utilizing the Giant Magneto-Resistance (GMR) effect. In these measurements, the spin orientation of the electron as compared with the direction of the ferromagnet magnetization determines the scattering rate and hence the effective sample resistance. An electron with spin aligned parallel to the magnetization will usually undergo less scattering than one with its spin pointing in the opposite direction. For non-magnetic materials, such as Cu or Au, l_{sf} is as long as a few hundred nanometers, whereas for ferromagnets like Py, Ni, or Co it is considerably shorter, i.e. $l_{sf} = 5, 21$ and 60 nm, respectively. A long l_{sf} is required for experiments where the spin coherence needs to be preserved over large distances, such as the propagation of a triplet order parameter in a Josephson-coupled S/F/S system.

In addition to the length scales already stated, it is also worth mentioning the concept of the Thouless energy, E_{Th}. It was was first introduced in the context of the scaling theory to the Anderson localization problem [34]. Its importance as it applies to the proximity effect between a normal metal in contact with a superconductor was stressed by Courtois and Pannetier in reference [35]. E_{Th} is usually not a dominant energy scale when compared to the ferromagnetic exchange energy E_{ex}, and therefore it is not usually included in theoretical treatments of F/S systems. However, given its importance with respect to the N/S proximity effect its definition will be included for completeness,

$$E_{Th} = \hbar/\tau_D \tag{2.6}$$

where for a diffusive metal $\tau_D = L^2/D$, representing the time required for an electron to reach the sample boundary. E_{Th} is therefore the energy uncertainty associated with the finite time an electron spends in a sample of dimension L.

2.2 Ferromagnetism

A ferromagnetic material has strongly coupled atomic magnetic moments which spontaneously align parallel to each other in the absence of an applied magnetic field. Above a critical temperature, called the Curie temperature, the spontaneous magnetization disappears as the thermal energy is large enough to destroy the ferromagnetic order. The origin of the large interactions between spins is quantum-mechanical in nature and results from the spin-statistics theorem, with the implication that one cannot make changes in the relative direction of two spins without changing the spatial charge distribution in the overlap region. The exchange interaction between two atoms i and j with spins $\mathbf{S}_i$ and $\mathbf{S}_j$ is given by the Hamiltonian [36]

$$\mathcal{H} = -2\,J\,\mathbf{S}_i \cdot \mathbf{S}_j \tag{2.7}$$

where J is the exchange integral. When J is positive, parallel alignment of spin is obtained as a result of energy minimization. Elemental materials, such as Fe, Co, Ni, Gd exhibit this kind of spontaneous ferromagnetic behavior, with exchange energy of the order of an eV.

The energy associated with a ferromagnetic material includes several other components in addition to the exchange energy. They are anisotropy and magnetorestrictive energy, demagnetizing energy, domain wall and also Zeeman energy when an external field is applied. These energies compete to give the overall magnetic structure and their contribution to the energy minimum depends on the shape and thickness of the ferromagnet as well as the growth conditions and substrate material on which it is deposited. For large ferromagnetic samples it is energetically favorable to form domains, which are volumes in the sample where the magnetization points along one direction. Domain walls are the transition regions between neighboring domains in which the magnetization is gradually rotated from one direction to the other. Thin films are

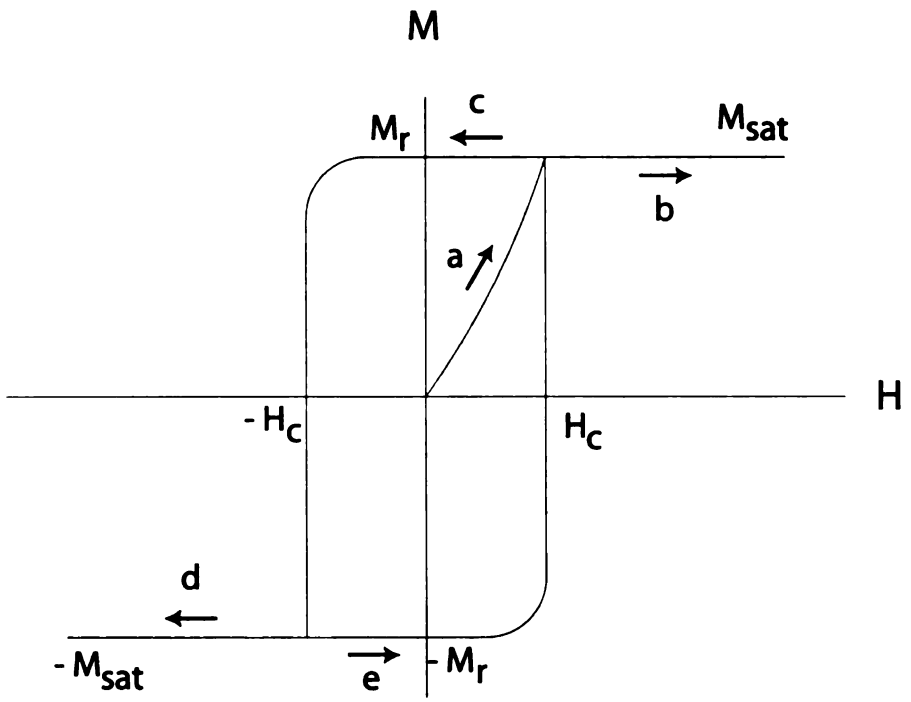

Figure 2.1: M vs. H for ferromagnet. In its virgin state the net magnetization is zero. a) Applying a field quickly reaches the saturation magnetization, M_{sat}. b) Further increasing the field will not increase the net magnetization. c) Reducing the field to zero leaves a remnant magnetization, M_r which may be lower than M_{sat}. d) After switching direction at the coercive field, $-H_C$, the magnetization reaches $-M_{sat}$. e) Reducing the field to zero gives $-M_r$. Further sweeping the field follows steps (b)-(e).

exclusively used in this thesis and they have a large shape anisotropy. As a result, their magnetization direction lies in the plane and the domain walls are Neel-type, where the spins continuously rotate in the plane to join two different domains.

The typical ferromagnetic behavior of the magnetization as a function of an external magnetic field is hysteretic, as shown in Fig. 2.1. The field at which the magnetization switches from one direction to the other is called the coercive field, H_C. The maximum value of the magnetization is called the saturation magnetization, M_{sat}, and occurs when all the spins are pointing along the direction of the field. The net magnetization at zero field is called the remnant magnetization, M_r. When the film is in its virgin state, i.e. no previous history of applied field since deposition, the net magnetization is zero, due to the random orientations of the magnetic

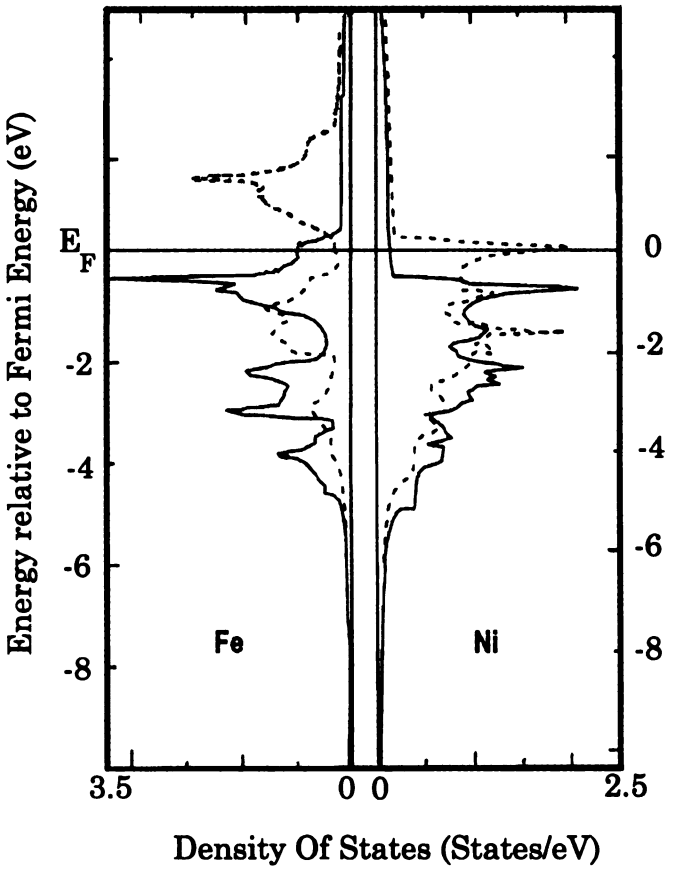

Figure 2.2: Calculated density of states illustrating the complex structure for the different minority and majority spin bands in ferromagnetic Ni and Fe, according to Moruzzi *et al.* [37]. The solid and dashed lines represent the majority and minority spin bands, respectively.

domains after growth. The application of a small field will then set the direction of net magnetization, which is then remembered if the field is removed. If the field is applied along the "easy" axis of the film, the switching behavior is sharp and does not require a large field to reach saturation. By contrast, very large field values are needed to reach saturation if applied along the "hard" axis, and the switching is gradual over a large field range. The directions of the easy and hard axes are related to the magnetocrystalline anisotropy, which has its origin in the spin-orbit interaction of the electrons. The electron orbits are linked to the crystallographic structure, and by

their interaction with the spins they make the latter prefer to align along well-defined crystallographic axes. Consequently, ferromagnetic materials are easier to magnetize along certain directions in space as compared to others.

In addition to the hysteretic magnetization behavior, another important characteristic of the ferromagnet is the density of states (DOS). Its shape is usually complex, exhibiting different features for the minority and majority spin bands, as illustrated in Fig. 2.2. This leads to spin-specific transport properties of the different spin carriers including conductivities, Fermi velocities and scattering potentials. These differences are at the core of spin-dependent transport.

2.3 Superconductivity

Three years after successfully obtaining liquid He^4 in 1908, Kamerlingh Onnes was the first to observe the sudden loss of resistance of mercury upon cooling. Shortly thereafter it was seen that there exists a maximum current or field beyond which superconductivity is destroyed. In addition to the property of perfect conductivity, it was later discovered that a superconductor also expels magnetic flux. Results from experiments involving different isotopes of mercury gave hints about the basic nature of superconductivity, involving a phonon-mediated attraction of electrons. In 1956 Cooper proposed a mechanism involving the formation of a pair of electrons with opposite spin and momentum and showed that the Fermi sea of electrons is unstable against the formation of a bound pair even with a weak attraction.

2.3.1 BCS Theory

According to the theory of superconductivity pioneered by Bardeen, Cooper and Schrieffer [38], one can apply a variational method to a proposed ground state wave-

function of the the form [39]

$$\Psi_k = \prod_k (u_k + v_k c^*_{k,\uparrow} c^*_{k,\downarrow}) |\phi_0\rangle \tag{2.8}$$

The probability that a state is filled with a pair of opposite spin and momentum, $(\mathbf{k}\uparrow, -\mathbf{k}\downarrow)$, is given by $|v_k|^2$. The probability that it is not occupied is given by $|u_k|^2 = 1 - |v_k|^2$. Using this form it can be shown that the ground state energy is less than that of the normal state. The single particle excitation spectrum is then given by

$$E_k^2 = \epsilon_k^2 + |\Delta|^2 \tag{2.9}$$

where ϵ_k is the electronic spectrum of the normal state measured from the Fermi energy and Δ is the gap. This shows that the minimum energy of an excitation is Δ. Assuming a spherical Fermi surface and looking at energies close to the Fermi energy the density of states for a superconductor is then given by

$$N_S(E) = \frac{N_N(0)\, E}{\sqrt{E^2 - |\Delta|^2}} \tag{2.10}$$

for energies above the gap and is 0 for energies below the gap. $N_N(0)$ is the normal density of states and is considered constant for energies close to the Fermi energy.

For non-zero temperatures, the formalism is extended to allow for single-particle excitations with probability according to equilibrium Fermi statistics. In the weak coupling limit, $N_N(0)V \ll 1$, one can obtain

$$k_B T_C = 1.14\, \hbar\omega_D \exp[N_N(0)V]^{-1} \tag{2.11}$$

where ω_D is the Debye frequency, V is the assumed constant interaction and T_C is the critical temperature where $|\Delta|$ tends to zero. The relation between the zero temperature gap and T_C is given by $2\Delta(0) = 3.52\, k_B T_C$.

2.3.2 Green's Functions

A formalism based on Green's functions was first introduced by Gor'kov in 1958 [40] to treat superconductivity, proving important in allowing for spatial variations such as those induced by an applied magnetic field. Theoretical works devoted to the F/S proximity effect are exclusively addressed in this way and this section contains a brief introduction to the topic.

The Gor'kov equations (for a review see for example Kopnin [41], pg. 46) are written in the language of second quantization and contain normal correlation functions in terms of creation and annihilation operators of the form

$$G_\sigma(x_1, x_2) = \langle T\Psi_\sigma(x_1)\Psi_\sigma^\dagger(x_2)\rangle \tag{2.12}$$

$$G_\sigma^\dagger(x_1, x_2) = \langle T\Psi_\sigma^\dagger(x_1)\Psi_\sigma(x_2)\rangle \tag{2.13}$$

with spin $\sigma = \uparrow, \downarrow$ and "anomalous" or superconducting correlations

$$F(x_1, x_2) = \langle T\Psi_\uparrow(x_1)\Psi_\downarrow(x_2)\rangle \tag{2.14}$$

$$F^\dagger(x_1, x_2) = \langle T\Psi_\uparrow^\dagger(x_1)\Psi_\downarrow^\dagger(x_2)\rangle \tag{2.15}$$

The $\langle\,\rangle$ brackets represent statistical averages, and T is the time-order operator. The arguments include both space and time variables for each particle, $x_i = (\mathbf{r}_i, t)$. The Gor'kov equations also contain a quantity Δ, called the order parameter, which is related to the anomalous Green function according to

$$\Delta(x) = |g|F(x, x) \tag{2.16}$$

where g is the coupling constant. The above is a self-consistency equation which couples the order parameter with F, which has to be found from the Gor'kov equations containing Δ. In the non-superconducting state Δ is zero, while it is non-zero in

superconducting state. In an F/S system, one is generally interested in the behavior of the superconducting correlations, i.e. F, and the extent to which they penetrate in the ferromagnet.

Since the Fermi wavelength, λ_F is usually much smaller than the characteristic length scale associated with the variation of the order parameter, a quasi-classical approximation is invoked in order to simplify the formalism by integrating out the fast oscillations of the Green's functions on the scale of λ_F. This approach was introduced by Eilenberger (1968) [42] and extended by Eliashberg (1971) [43], and by Larkin and Ovchinnikov (1977) [44]. In the dirty limit case, treated by Usadel (1970) [45], the mean free path is short compared to the coherence length and the Eilenbeger equations are simplified considerably for s-wave superconductors, with Δ being independent of the momentum direction. The Usadel equations will be presented in Section 2.5.3 and shown how they can be used to obtain a prediction for a physically measurable quantity, such as the critical temperature of an F/S bilayer.

2.4 Normal/Superconductor

The term proximity effect typically refers to the transfer of Cooper pair correlations from a superconductor (S) to a normal metal (N) in a S/N system [46]. The spacial extent of the correlations is on the order of the coherence length, which depends on whether the system is ballistic or diffusive, and can be as large as a few microns. In this manner, the DOS and transport properties of the N material are modified [35]. Furthermore, for a thin superconductor, an inverse-proximity effect also occurs, which effectively weakens the superconducting properties close to the interface. This effect can be observed by measuring the critical temperature of an S/N bilayer, which results in a depression of T_C as compared to an isolated S layer.

The mechanism by which the superconducting correlations enter the normal material is called Andreev reflection. Figure 2.3 illustrates this process showing the DOS

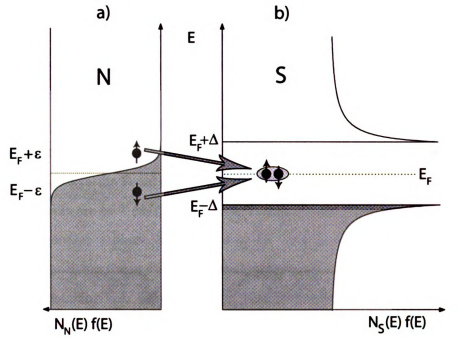

Figure 2.3: Procedure by which an incoming electron incident on an NS interface from the a) normal metal side finds no available quasiparticle states below the gap, Δ, and enters the b) superconductor by forming a Cooper pair in a process known as Andreev reflection.

multiplied by the distribution function, $f(E)$, on both sides of an ideal S/N junction. This depiction illustrates the number of available quasiparticle states and how these states are filled for both the N and S materials. For the normal material the DOS is weakly energy dependent, $N_n(E) \propto E^{1/2}$. However, for energies close to the Fermi energy, E_F, it is considered to be essentially constant. In equilibrium the filling of these levels follows the Fermi-Dirac distribution,

$$f(E) = \frac{1}{\exp\left(\frac{E-\mu}{k_B T}\right) + 1} \tag{2.17}$$

where μ is the chemical potential and $k_B T$ is the thermal energy.

On the other hand, the DOS of the superconductor has a gap according to Eqn. 2.10, and therefore transfer of single quasiparticle states from the normal metal with

energy below Δ is not allowed. As shown in Fig. 2.3, an incoming electron with energy $E_F + \epsilon$ can only be transferred through the interface by forming a Cooper pair with an electron of opposite momentum and spin with energy $E_F - \epsilon$. In this Andreev reflection process, no energy is transferred into the superconductor. From the N metal side, this can be viewed as an electron incident on the N/S interface being reflected as a hole. In the excitation picture, shown in Fig. 2.4 (a), energies are taken with respect to the Fermi energy and the wave vectors for the incident electron and reflected hole are $k_F + \delta k/2$ and $k_F - \delta k/2$, respectively. Therefore, the electron and hole accumulate a phase difference, $\phi = \delta k \cdot x$, as a function of the distance traveled and the difference in k. For electrons with energy equal to E_F, the incoming electron and outgoing hole follow the exact time reversed paths. The wave vector mismatch, linear in energy, establishes the length scale for correlations between the time reversed state of the electron and hole according to an uncertainty principle

$$\Delta\epsilon\,\Delta\tau \geq \hbar/2. \tag{2.18}$$

Substituting the time $\Delta\tau$ from above in equations equivalent to Eqns. 2.4 and ignoring the factor of 2 we obtain

$$\xi_\epsilon = \frac{\hbar v_F}{\epsilon} \quad \text{clean limit} \tag{2.19}$$

$$\xi_\epsilon = \sqrt{\frac{\hbar D}{\epsilon}} \quad \text{dirty limit} \tag{2.20}$$

where D is the diffusion constant in the normal metal. At finite temperatures, the coherence length for a normal metal is then

$$\xi_N = \frac{\hbar v_F}{2\pi k_B T} \quad \text{clean limit} \tag{2.21}$$

$$\xi_N = \sqrt{\frac{\hbar D}{2\pi k_B T}} \quad \text{dirty limit,} \tag{2.22}$$

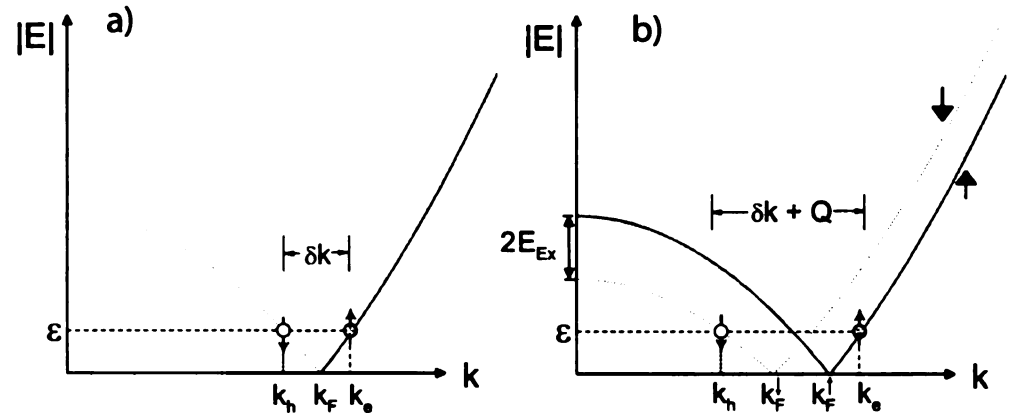

Figure 2.4: Andreev Reflection process in the excitation picture for the a) N/S interface and b) F/S interface. The incoming electron with spin ↑ is reflected as a hole with spin ↓. The Cooper pair entering the ferromagnetic region acquires a center of mass momentum $Q = 2E_{ex}/\hbar v_F$ due the energy difference between the minority and majority spin bands. All energies are taken with respect to E_F.

being set by the thermal energy, which determines the decay length of the order parameter in the normal metal. In an S/N/S system, if the thickness of the N layer is smaller than ξ_N then one can observe supercurrent transfer from one superconductor to the other, i.e. zero voltage Josephson coupling across the junction.

2.5 Ferromagnet/Superconductor

When a ferromagnet is placed in contact to a superconductor, similarly to the S/N system, the superconducting correlations traverse the interface and enter the ferromagnet. However, the presence of an exchange field in the latter preferentially selects one spin orientation over the other and in so doing introduces an additional mechanism for breaking the Cooper pair. Therefore, in addition to the normal state exponential decay, the order parameter has a modulation that is a direct consequence of the energy separation between the spin up and spin down bands associated with the ferromagnet.

2.5.1 Order Parameter

The origin of the oscillation can be understood from a conservation of energy argument, as given in the work of Demler *et al.* [47]. The spin up electron of the pair entering the ferromagnet lowers its potential energy by E_{ex}, while the spin down electron raises its energy by the same amount. In order to conserve energy, the spin up electron raises its kinetic energy and the spin down electron lowers it.

$$E_{\uparrow,\downarrow}(k) = \frac{\hbar^2 k_{\uparrow,\downarrow}^2}{2m} - E_F \pm E_{ex} \tag{2.23}$$

The Fermi momentum for each spin orientation is then

$$k_F^{\uparrow,\downarrow} = \frac{1}{\hbar}\sqrt{2m(E_F \mp E_{ex})} \tag{2.24}$$

Since $E_F \gg E_{ex}$ then

$$Q \equiv k_F^{\uparrow} - k_F^{\downarrow} = \frac{1}{\hbar}\sqrt{2mE_F} \cdot \frac{E_{ex}}{E_F} \tag{2.25}$$

As a result, the pair entering the ferromagnet acquires a non-zero center of mass momentum,

$$Q = 2E_{ex}/\hbar v_F \tag{2.26}$$

where $v_F = \sqrt{2E_F/m}$. Fig. 2.4 (b) shows the additional wave vector of the incoming electron and outgoing hole associated with the differences in energy between the two spin bands. If we consider the two-particle wavefunction as being related to the superconducting order parameter

$$\Psi(x_1 - x_2) \propto \exp[ik_F(x_1 - x_2)] \tag{2.27}$$

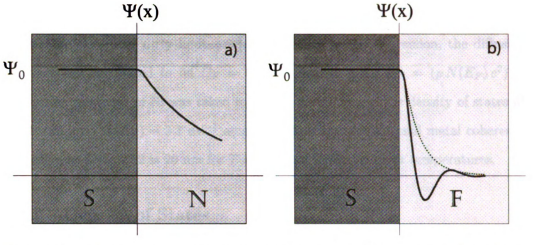

Figure 2.5: a) Order parameter decays exponentially in the N material. b) In addition to the fast exponential decay in the dirty limit, the order parameter oscillates on a length scale set by the exchange field, E_{ex}.

then upon entering the ferromagnet each electron acquires an additional wave vector, $Q/2$, therefore

$$\Psi'(x_1 - x_2) \propto \exp[i(\overline{k_F} + Q/2)x_1] \exp[-i(\overline{k_F} - Q/2)x_2] = \Psi(x_1 - x_2)e^{iQR} \quad (2.28)$$

where $R = (x_1 + x_2)/2$ is the center of mass coordinate and $\overline{k_F} = (k_F^{\uparrow} + k_F^{\downarrow})/2$. The real part of Ψ' oscillates in space with period set by Q of Eqn. 2.26. In addition to the oscillation, the order parameter also vanishes on the scale of inverse Q, i.e.

$$\xi_F = \frac{\hbar v_F}{2E_{ex}} \quad \text{clean limit} \quad (2.29)$$

$$\xi_F = \sqrt{\frac{\hbar D_F}{2E_{ex}}} \quad \text{dirty limit} \quad (2.30)$$

resulting from averaging over momentum directions for the clean case and arising naturally due to scattering for the dirty one [48]. The length scale associated with

the propagation of correlations inside the ferromagnet is therefore very short, being set by the size of the exchange energy E_{ex}. For ferromagnetic Ni, the majority spin band $v_F = 0.28 \cdot 10^8$ cm/s and $2E_{ex} = 0.23$ eV, which results in $\xi_F = 0.8$ and 2.0 nm for the clean and dirty limit, respectively. In the last expression, the diffusion constant was calculated to be $D_F = 6.7$ cm^2/sec by using $D_F = (\rho N(E_F) e^2)^{-1}$, where the resistivity of Ni was taken to be $\rho = 33$ nΩ m and the density of states at the Fermi level $N(E_F) = 3.1$ eV^{-1} atom^{-1}. The dirty limit normal metal coherence according to Eqn. 2.22 is 20 nm for $T = 2$ K and longer at lower temperatures.

2.5.2 Density of States

The result of the proximity effect on the DOS of a normal material in contact with a superconductor is generally measured by tunneling spectroscopy experiments [49]. At zero temperature, it can be shown that the differential conductance of a tunnel junction between a normal metal probe and the metal under study, as a function of voltage V, is proportional to the DOS at energy eV. This can be understood simply by the fact that sweeping the voltage changes the difference in the chemical potentials between the normal metal and the probe. Since the two are separated by an insulator, the conduction is due to the tunneling from the occupied states of one material to the empty levels of the other which is dependent on the number of available states, i.e. the DOS.

The existence of superconducting correlations in the normal metal changes the DOS by introducing a depression at zero energy similar to a gapless superconductor (Fig. 2.6 (a)). The extent and amplitude of this feature depends on the coherence length in the normal metal and the distance of the tunnel probe with respect to the S/N interface. The further away the probe is from the interface, the smaller the effect, and at distances greater than ξ_N or L_ϕ it disappears completely. Fig. 2.6 (a) illustrates the data from an experiment conducted by Guéron *et al.* [49] involving

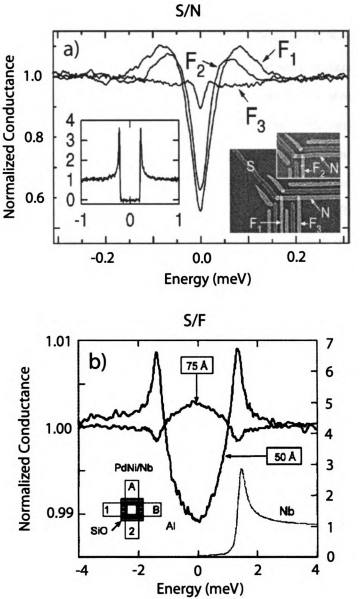

Figure 2.6: Normalized Conductance vs. Energy as a function of distance from the interface for an a) N/S system, illustrating the decay of the order parameter inside the normal metal [49]. The insert shows the conductance for the bare superconductor. For a b) F/S system, the influence upon the conductance due to the oscillation and decay of the order parameter inside the ferromagnet is shown as a function of its thickness [13] (the conductance of the bare Nb is also shown). For both the N/S and F/S case, the normalized tunneling conductance is proportional to the DOS.

a superconducting wire in contact with a very long normal wire. The normalized conductivity vs. applied voltage plots are obtained as a result of placing three normal probes (F1, F2, F3) at distances of 200, 300 and 800 nm from the N/S contact region, respectively, indicating how the proximity effect is reduced with distance.

In a similar manner, the DOS of the ferromagnet in an F/S system can also be investigated by tunneling experiments. Due to the oscillations in the order parameter, the DOS shows different behavior based on its sign. More specifically, a pseudo-gap is present when the order parameter is positive, whereas this feature becomes inverted for negative values. Although the extent of the proximity effect is reduced as compared to the N/S system, it has been experimentally verified by Kontos *et al.* [13] by performing tunneling experiments on an $Al/Al_2O_3/Pd_{1-x}Ni_x/Nb$ system with different thickness ferromagnets. The lateral dimensions of heterostructures were in the μm regime. The Al layer measured the DOS at the edge of the ferromagnet, a distance d_F away from the F/S interface, where d_F is the thickness of the ferromagnet. The choice to use weakly ferromagnetic $Pd_{1-x}Ni_x$ was made in order to increase the penetration length of the Cooper pairs inside the ferromagnet by reducing E_{ex}, and thus enabling the observation of the sign change in the DOS as a result of varying the F layer thickness.

2.5.3 Critical Temperature

In addition to changes in the DOS, another method to investigate the proximity effect in a ferromagnet is to look at the critical temperature behavior of an S/F bilayer. This section will outline in a non-rigorous manner the standard theoretical approach which uses the Green functions method introduced in section 2.3.2 to obtain the critical temperature of an F/S bilayer. According to Houzet [50] the dirty-limit

Usadel equation in the S layer can be written as

$$-D_S\partial(\hat{g}\partial\hat{g}) + [\omega_n\tau_z - i\hat{\Delta}, \hat{g}] = 0 \tag{2.31}$$

where D_S is the diffusion constant and $\omega_n = (2n+1)\pi T$ are the Matsubara frequencies at temperature T. The components of the matrix $\hat{g}$ are scalar, as follows:

$$\hat{g} = \begin{pmatrix} g & f \\ f^\dagger & -g \end{pmatrix}, \tag{2.32}$$

which represent the normal (g) and anomalous (f) correlations. The components satisfy the normalization conditions $\hat{g}^2 = 1$ and $g^2 + ff^\dagger = 1$. The 2 x 2 matrices in Eqn. 2.31 are $\hat{\Delta} = i\,(Re\,\Delta\tau_y + Im\,\Delta\tau_x)$, where $\tau_i(i = x, y, z)$ are the Pauli matrices and the self-consistency gap equation is

$$\Delta = i\pi T|\lambda| \sum_{\omega_n} f. \tag{2.33}$$

λ is the superconducting coupling constant and the sum is over all the Matsubara frequencies. Similarly, the Usadel equation for the ferromagnet is written as

$$-D_F\partial(\hat{g}\partial\hat{g}) + [(\omega_n + ih)\tau_z, \hat{g}] = 0, \tag{2.34}$$

where the exchange field in the F layer is $\boldsymbol{h} = h\hat{z}$ and D_F is the diffusion constant. Eqns. 2.31 and 2.34 assume that the exchange field is limited to the ferromagnet and the gap exists only in the superconductor. For proper solutions, boundary conditions for the normal and anomalous components must also accompany these equations, at the F/S interface as well as outer edges of both of the F and S layers.

Close to the transition temperature, $\Delta \rightarrow 0$, and the Usadel equations can be

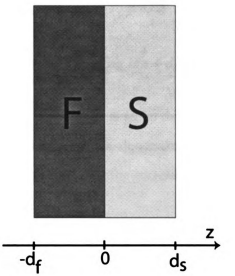

Figure 2.7: F/S bilayer where the S layer thickness is d_S and that of the F layer is d_F. The exchange field is present only in the F layer and only the S layer has a superconducting gap, Δ.

linearized, so that in terms of f one obtains

$$-D_S\partial_z^2 f + 2|\omega_n|f = -2i\Delta \quad \text{in S layer} \tag{2.35}$$

$$-D_F\partial_z^2 f + 2(|\omega_n| + i\,\mathrm{sgn}(\omega_n)h)f = 0 \quad \text{in F layer} \tag{2.36}$$

with boundary conditions at the F/S interface

$$\partial_z f_F = \frac{\sigma_S}{\sigma_F}\partial_z f_S = \frac{1}{\gamma_B \xi_S}(f_F - f_S) \tag{2.37}$$

The correlation functions in the ferromagnet and superconducting layers are f_F and f_S with conductivities σ_F and σ_S, respectively. The dirty-limit coherence length is ξ_S and the interface resistance parameter is $\gamma_B = R_b\sigma_F/\xi_S$.

The boundary condition at the outer edge of the F layer is obtained by allowing the derivative of f vanish, i.e. $\partial_z f_F(z = -d_F) = 0$, and so the solution to Usadel

equation in the F layer then becomes

$$f_F(z) = f_0 \cosh\, k(z + d_F) \tag{2.38}$$

with $k = \sqrt{2/D_f(|\omega_n| + ih\,\mathrm{sgn}\,\omega_n)}$ and f_0 is to be determined by solving the Usadel equation in the S layer. In order to do this, one makes the assumption that $d_S \ll \xi_S$ and, in so doing, using average values for the correlation function f and Δ in the S layer,

$$f_S \approx \frac{1}{d_S}\int_0^{d_S} dz\, f(z) \quad \text{and} \quad \Delta \approx \frac{1}{d_S}\int_0^{d_S} dz\, \Delta(z) \tag{2.39}$$

Similarly to the F layer, $\partial_z f_S(z = d_S) = 0$, and integrating by parts one obtains

$$|\omega_n| f_S + \frac{D_S}{2d_S}\partial_z f_S \simeq -i\Delta \tag{2.40}$$

Using the boundary conditions and the above equations one can then obtain a solution for the correlation function in the S layer,

$$f_S = -i\Delta\frac{1}{|\omega_n| + 1/\tau_0}, \qquad \frac{1}{\tau_0} = \frac{D_S\sigma_F}{2d_S\sigma_S}\frac{k\sinh kd_F}{\cosh kd_F + \xi_S\gamma_B k\sinh kd_F} \tag{2.41}$$

Using this result, the self-consistent gap equation becomes

$$1 = \pi T|\lambda|\sum_{\omega_n}\frac{1}{|\omega_n| + 1/\tau_0} = 2\pi T|\lambda|\; Re\sum_{\omega_n > 0}\frac{1}{\omega_n + 1/\tau_0} \tag{2.42}$$

The equation defining the bare superconductor with critical temperature T_{C0} is

$$1 = 2\pi T_{C0}|\lambda|\sum_{\omega_n^0 > 0}\frac{1}{\omega_n^0} \tag{2.43}$$

where $\omega_n^0 = (2n + 1)\pi T_{C0}$. Since the sums are divergent they can be cut off at high energy scales compared to the BCS pairing, i.e. the Debye frequency ω_D. Therefore,

for $T, T_{C0} \ll \omega_D$ one can write

$$1 - 2\pi T|\lambda| \sum_{\omega_n > 0}^{\omega_D} \frac{1}{\omega_n} = |\lambda| \left(2\pi T_{C0} \sum_{\omega_n^0 > 0}^{\omega_D} \frac{1}{\omega_n^0} - 2\pi T \sum_{\omega_n > 0}^{\omega_D} \frac{1}{\omega_n} \right) \simeq |\lambda| \ln \frac{T}{T_{C0}} \tag{2.44}$$

and also

$$1 - 2\pi T|\lambda| \sum_{\omega_n > 0}^{\omega_D} \frac{1}{\omega_n} = 2\pi T|\lambda| \sum_{\omega_n > 0} \left(Re \frac{1}{\omega_n + 1/\tau_0} - \frac{1}{\omega_n} \right) \tag{2.45}$$

In both Eqn. 2.44 and 2.45, expressions obtained from Eqn. 2.43 and 2.42 were substituted for the value of one, respectively. The last equivalence from Eqn. 2.44 was obtained by using the fact that

$$\sum_{x=0}^{N} \frac{1}{x + 1/2} \approx \ln(N) + 2\ln 2 + C \tag{2.46}$$

and the definition for the Matsubara frequency, as follows

$$2\pi T_{C0} \sum \frac{1}{(2n+1)\pi T_{C0}} = \sum_{n=0}^{n'} \frac{1}{n + 1/2} \approx \ln(\frac{\omega_D}{2\pi T_{C0}}) + 2\ln 2 + C \tag{2.47}$$

where $n' = \omega_D / 2\pi T_{C0}$. The ω_D cutoff was removed from the second sum in Eqn. 2.45 since it is no longer divergent. Equating Eqn. 2.44 and 2.45, and eliminating $|\lambda|$ one can then obtain

$$0 = \ln \frac{T}{T_{C0}} + 2\pi T \sum_{\omega_n > 0} \left(\frac{1}{\omega_n} - Re \frac{1}{\omega_n + 1/\tau_0} \right) \tag{2.48}$$

which gives the equation for the critical temperature, T, of an S/F bilayer

$$\ln \frac{T}{T_{C0}} + Re\, \psi \left(\frac{1}{2} + \frac{1}{2\pi T \tau_0} \right) - \psi \left(\frac{1}{2} \right) = 0 \tag{2.49}$$

where the digamma function ψ is the logarithmic derivative of the gamma function and can be expressed in terms of half-integer values as

$$\psi\left(n+\frac{1}{2}\right) = -\gamma - 2\ln 2 + \sum_{k=1}^{n} \frac{2}{2k-1} \tag{2.50}$$

The thickness dependence of the critical temperature equation is contained in τ_0 as given in Eqn. 2.41.

Equations very similar in form to Eqn. 2.49 are obtained by theoretical treatments of Tagirov [32] and Fominov [33], involving F/S/F trilayer structures. In Chapter 5, the exact form of these equations will be presented and their solution will be applied to obtain fits for T_C experiments that we have performed on Ni/Nb/Ni and $Ni_{84}Fe_{16}$/Nb/$Ni_{84}Fe_{16}$ trilayer structures.

Chapter 3

Experimental Methods

This chapter will outline the various experimental techniques utilized in sample fabrication, characterization and measurement. The types of samples that have been fabricated include those with macroscopic dimensions (mechanically patterned) as well as those with microscopic dimensions (lithographically patterned), ranging from mm to nm length scales, respectively. Ferromagnet/Superconductor/Ferromagnet trilayer structure experiments, whose results are described in the next chapter, required the fabrication of large, macroscopic samples by means of mechanical masking. Experiments searching for a triplet order parameter in conventional superconductors utilized both macroscopic and microscopic sample preparation techniques, the latter including combinations of lithographical procedures. In this chapter, the two main material deposition methods are described, namely sputtering and thermal evaporation, followed by detailed descriptions of our patterning techniques. Subsequent sections will outline sample characterization (SQUID Magnetometry) and various measurement methods.

3.1 Material Deposition

The method that has become the workhorse for most of our thin film fabrication is known as sputtering. This process involves the generation of a beam of electrons, by running a current through a Tungsten filament, which is then used to ionize Ar gas at low pressure (mTorr range). The Ar ions are in turn accelerated toward a target material by a large voltage. Permanent magnets are used to contain the plasma. Upon collision with the target, material is removed by momentum transfer or local heating, and are subsequently deposited onto a substrate nearby. The direction of incoming material arriving at the sample surface covers a range of angles with respect to the sample normal, due to collisions with the Ar gas. Therefore sputtering is a non-collimated method of deposition.

All our substrates are purchased as 3" diameter wafers of oxidized Si (100) from Silicon Quest Int'l, with thickness $13 - 17$ mils (0.001 inches) and resistivity $1 - 10\,\Omega\,\mathrm{cm}$. After dicing to desired dimensions, the substrates are subjected to a rigorous ultrasonic cleaning procedure in Alconox, followed by rinsing with deionized water (DI). The process is continued with an Acetone and then an Isopropyl Alcohol (IPA) ultrasonic cleaning. Finally, the substrates are dried with pure Nitrogen gas.

The sputtering system used for sample deposition contains four large triode sources positioned at 90° with respect to each other (see Fig. 3.1). There are also two smaller magnetron sources in the chamber, thus allowing up to six different material types to be deposited in one pump-down. All individual sources have "chimneys" designed to prevent cross-contamination and minimize the area exposed by the target material. The guns are covered by a computer-controlled shutter plate with four circular openings which can then allow or prevent deposition from the four main sources. The plasma above the larger sources is maintained during the entire sputter run, while the smaller sources are turned on only when needed. Up to 16 samples can be mounted on holders that are attached to a computer-controlled plate that rotates

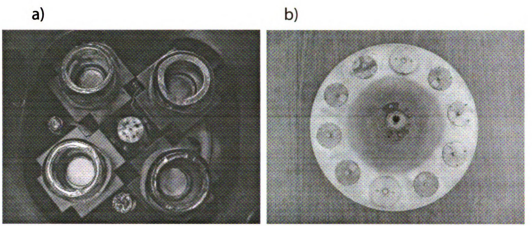

Figure 3.1: a) Top view of 4 main triode sputter sources as well as two smaller magnetron sources b) Bottom view of sample plate with individual masking system.

a few inches above the sources. Initially, all samples are covered by individual masks, which can then be selectively removed using an in-vacuum wobble-stick mechanism. In this manner, each sample can be exposed to different materials while the others are protected. Samples were sputtered using single (Fig. 3.2) or multiple-sequence mechanical masks (Fig. 3.3), producing CIP-type or CPP-type samples, with current flowing in the plane or perpendicular to the plane, respectively.

The sample plate also contains two Sycon Instruments quartz crystal monitors, which are used to measure the sputtering rate for each target. The rate of deposition is controlled by the plasma current (essentially the number of ionized Ar atoms hitting the target) as well as by the accelerating voltage which the Ar ions experience. The base pressure, obtained using a CTI Cryo-Torr high vacuum pump, is typically $3 - 4 \cdot 10^{-8}$ Torr with a slight improvement right before sputtering due to the addition of liquid nitrogen to a cold trap located at the top of the chamber. A capillary tube in contact with the cold trap carries $750 - 1000$ psi of cold nitrogen to heat exchangers on the substrate plate, keeping the temperature of the latter between -30 and $+30$°C. Upon reaching the desired sample plate temperature and base pressure, the chamber is filled with 2.5 mTorr of ultra pure Ar gas and the sputter sources are

turned on. Typical values for plasma current are $0.3 - 0.5$ Amps and accelerating voltage of $300 - 600$ Volts. Depending on the material, one needs to pre-sputter for some time in order to eliminate oxide layers formed on the targets during exposure to the atmosphere. Niobium, for example, requires a minimum of around $15 - 30$ minutes for good quality superconducting properties (bulk T_C around 9.1 K).

In addition to sputtering, thermal evaporation is another method of material deposition with typical deposition pressure around 10^{-7} Torr range. This technique involves passing a current through a boat-like container (typically Tungsten or Alumina coated) that does not form an alloy with the desired material. In this manner, the target material is melted and subsequently evaporated onto a substrate above. As a result, a directionality is instilled to the ejected material, being considered collimated over a small angle. This property is ideal for performing multiple-angle evaporations within the same vacuum pump-down. accomplished by tilting the sample with respect to each source. By this method, a good contact can be obtained between different materials, which is a desirable property when proximity effects are under investigation.

3.2 Patterning Techniques

Several methods are used to obtain the geometrical patterns of our samples and they depend on the required lateral dimensions. For macroscopic feature sizes, single or multiple mechanical stencils are typically employed. For micro and nano-scale devices, lithographical techniques are utilized. Often a combination of some or all of the above is practiced, including material removal techniques, such as ion milling.

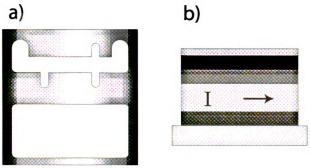

Figure 3.2: a) Mechanical mask producing a 4-terminal device for transport measurements and a rectangular film that can be used for magnetization measurements. b) Cross-section of a FSF trilayer structure with the current traveling in the plane of the sample (CIP).

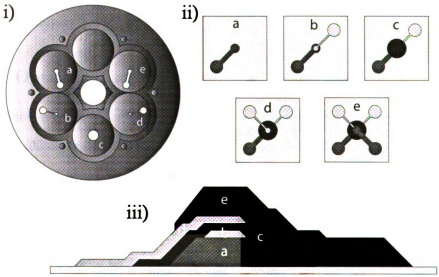

Figure 3.3: i) Multiple mechanical mask producing a 4-terminal device with separate voltage and current leads. ii) Mask sequence. iii) Sample cross-section, where current flows perpendicular to the substrate plane (CPP), from a to e, and the voltage is measured between b and d. This type of sample is used in an experiment designed to detect a triplet order parameter in conventional superconductors.

3.2.1 Mechanical Masking

Mechanical masks are the most convenient method of patterning as they do not require any additional steps outside of placing the mask on top of the substrate followed by deposition. The mask shown Fig. 3.2 is composed of a 4-terminal (CIP) geometry, used for resistance measurements of F/S/F trilayers. The same mask also contains a rectangular pattern used for a corresponding magnetic measurement of the same sample. Fig. 3.3 shows a multiple mask system, which is rotated clock-wise to expose the Si substrate sequentially, producing the pattern shown in (e). The resulting cross-section of the sample shown in the figure illustrates that the current flows perpendicular to the plane of the substrate (CPP). This mask was used for samples of the type F/S/F/S/F, where a current was flowing between the two outer ferromagnets while a voltage was measured between the two inner superconductors. This geometry was fabricated in order to detect the presence of a triplet order parameter in conventional superconductors.

3.2.2 Optical Lithography

This method is utilized for fabricating samples with lateral dimensions in the range of several millimeter down to a few microns. For this thesis, the optical lithographical process was used to define a generic lead pattern to be used in conjunction with an electron beam lithographical process (next section) to produce samples of nanometer-size lateral dimension.

The basic procedure for optical lithography involves coating a clean Si substrate with a thin polymer resist (S 1805), which is sensitive to deep ultra-violet (DUV) radiation. To pattern the resist, a mask made of a white crown substrate covered with Chrome is used. Using AutoCAD, we have designed the mask shown in Fig. 3.5 to suit our size and number of leads requirements. The mask was then commercially fabricated by Photronics Inc. Once the resist is exposed, a developer material (Mi-

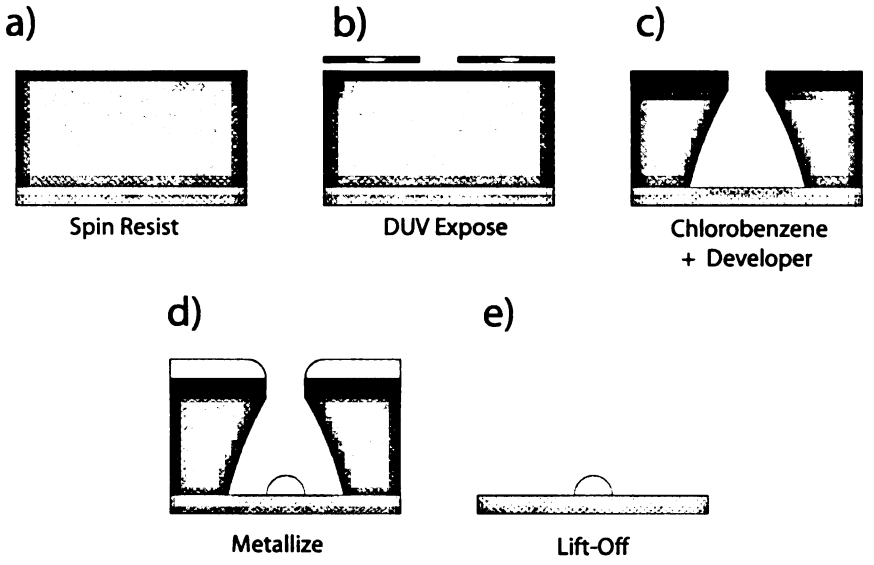

Figure 3.4: Pattern transfer sequence using optical lithography. a) Coating of the bare substrate with optical resist. b) Exposure of the sample with deep UV radiation by using an optical mask. c) Development of the exposed areas with good undercut. d) Material deposition. e) Removal of the metallized resist.

croposit 452) will preferentially remove resist from the irradiated area. In this manner the pattern of the mask is transferred onto the resist, revealing the bare substrate (see Fig. 3.4).

An important aspect needed to successfully transfer a metallized pattern by this method is the profile of the resist after development, called undercut. Using a single layer, the sidewalls of the resist are essentially perpendicular to the substrate. In the process of deposition, material will then be collected on the substrate as well as the sidewalls of the resist, which when removed will often lift the desired pattern as well. Having an undercut profile in the shape of a teardrop, as shown in Fig. 3.4 (c), will improve this lift-off process. To accomplish this, the exposed substrates are first placed in a chlorobenzene solution to toughen the top part of the resist before being immersed in the developer.

After development, the substrates are mounted in a thermal evaporator, where Ti(2 nm)/Au(30 nm) is deposited, covering the top of the unexposed resist as well

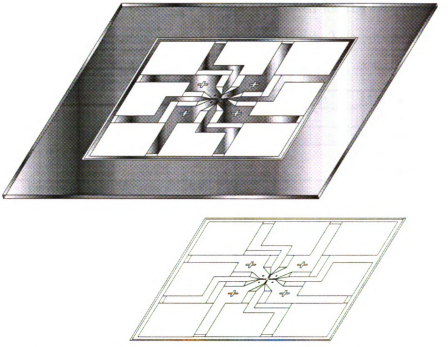

Figure 3.5: Optical pattern imprinted by deep UV exposure of the resist through openings in a Chrome covered White Crown substrate mask (smallest feature size is 3 μm). All the leads are connected via a grounding wire on the periphery for electrostatic discharge protection. The enclosing outer line is used for dicing.

as the exposed substrate. Thicker Au layers will improve the visibility of the leads with the electron microscope but may lengthen the lift-off process. Typical deposition rates for Au are $2.5 - 3.0$ Å/s, and about 0.5 Å/s for Ti. In order to avoid possible problems with contact between the leads and subsequent material to be deposited, the profile of metallized lead pattern is tapered by evaporating at a slight angle (15-30°), while continuously rotating the substrate. The choice of Au as the material to be used for the leads is due to its low resistivity and lack of oxidization. The thin Ti layer is used to improve adhesion of the Au to the Si substrate.

After the materials have been deposited, the substrates are then immersed in warm acetone and suspended upside down, which removes the metalized resist, while retaining the Ti/Au metal on the Si. Once the substrate is removed from the acetone and dried, no further lift-off can be obtained by reinserting the substrate back into

the acetone. Therefore, sufficient time should be allowed for the lift-off process so as to obtain a complete removal of all the metallized resist. This optical lithography procedure is outlined in Table 3.1 for quick reference.

Spin	S 1805 resist	4000 rpm	40 sec
Bake	Hot plate	150°C	60 min
Expose	DUV		2.8 sec
Undercut	Chlorobenzene DI		10 sec 10 sec
Develop	Microposit 452 DI		45 sec* 10 sec
Metalize	Ti(2 nm)/Au(30 nm)	P = 2-3·10^{-7} Torr	
Lift-Off	Acetone IPA DI	60°C	60 min* 10 sec 10 sec

Table 3.1: Steps for optical lithography. * as necessary.

A 3" Si wafer will produce one hundred 5 mm x 5 mm chips, each with a total of 8 leads and a smallest feature size of 3 μm. The optical pattern (shown in Fig. 3.5) also includes a series of alignment marks in the shape of crosses of size 250, 50, 6 μm. The smallest marks are used to locate the 60 x 80 μm^2 writing area at the center of the chip, where the nm-size samples are to be patterned. The alignment accuracy with respect to the Ti/Au leads is about 50 nm, being limited by the size of the smallest marks.

3.2.3 Electron Beam Lithography

The size of the smallest feature obtained with optical lithography is limited by the wavelength of light. To obtain patterns with dimensions in the sub-micron regime (for example Fig. 3.6), a similar lithographical approach is taken, whereby an electron beam is scanned across the surface of a resist material in a controlled way in order to obtain the desired pattern. In the same manner, the exposed resist will be removed by being immersed in a developer, followed by a metallization step, and then a lift-off

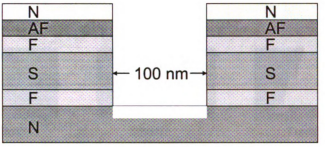

Figure 3.6: Alternative experimental geometry proposed for observation of long-range triplet superconducting correlations in an F/S/F/S/F system, requiring electron beam lithography to obtain a feature size in the nm range.

step in warm acetone for removal of the residual resist (shown in Fig. 3.7).

The lithography is accomplished by using a JEOL electron microscope (model JSM-840A) modified for computer control. The beam is generated by applying a large current through a Tungsten filament with a sharp tip. A large voltage (35 kV) will then accelerate the electrons from the cathode to the anode. A small aperture in the anode allows the electrons to travel down the microscope column. By passing through a series of lenses the electron beam is focused on the sample surface. The position of the beam is precisely controlled by a J. C. Nabity Nanometer Pattern Generation System Version 7.4 computer program, which controls the beam using deflection lenses and a blanker. The size of the smallest feature written in this manner can be around 50 nm, being limited by the size and shape of the beam when it hits the resist, the dose received per unit time and proximity effects caused by electrons backscattered from the substrate. The electron current is measured by focusing the beam at higher magnification inside a Faraday cup located on the sample holder.

Stigmation is the process by which the optimal shape of the beam (circular) is obtained by independently controlling x and y electrostatic lenses. This is performed at the highest magnification (300,000x) and usually on a sample different from the one which is to be written. The stigmation is verified visually by adjusting the

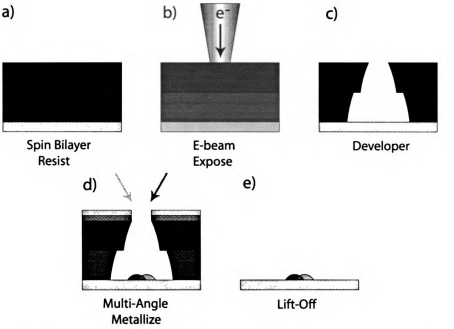

Figure 3.7: Electron Beam Lithography using a bilayer resist in a procedure with multiple-angle evaporation. Resists layers of different sensitivities create an optimized undercut. Evaporations from several angles allow for improvement of interfaces between materials as they are performed in a single vacuum pump-down.

focus back and forth and observing the changes in the horizontal and vertical edges of the feature imaged. A sign of good stigmation is when edges in both directions become visually sharp simultaneously. Once stigmated, the microscope is focused as close to the writing area as possible, either on the edge of a silver paint spot or one of the optically patterned alignment marks. For e-beam lithography, two layers of electron-sensitive resist are utilized in order to optimize the smallest feature size and shape of the undercut profile. The one at the bottom is a copolymer (COP) layer of P(MMA(8.5)MAA) 9% in ethyl lactate and the one on top is a layer of 495 PMMA 4% in chlorobenzene. The top layer of resist is more resistant to the developer (methyl isobutyl keytone diluted in isopropyl alcohol as MIBK 1 : IPA 3) as compared to the one on the bottom. The specific procedure for electron beam lithography is reviewed in Table 3.2.

Spin	COP(MAA) 9%	5000 rpm	40 sec
Bake	Hot plate	180°C	10 min
Spin	PMMA 4%	6000 rpm	40 sec
Bake	Hot plate	180°C	60 min
Expose	JEOL	bilayer undercut	250 - 300 $\mu C/cm^{2*}$ 70 - 100 $\mu C/cm^2$
Develop	MIBK IPA DI		30 sec* 10 sec 10 sec
Metalize			
Lift-Off	Acetone IPA DI	60°C	60 min* 10 sec 10 sec

Table 3.2: Steps for Electron Beam lithography. *as necessary.

The choice of COP(MAA) 9%/PMMA 4% for the bilayer resist, although slightly worse in terms of resolution as compared to a COP(MAA)9%/PMMA 2% bilayer, will give a larger undercut (as large as a few microns). This selection is necessary when considering the deposition of several materials within one vacuum pump-down. Evaporation at several angles with respect to the sample normal is a method which is preferred for improving the quality of the interface between the different materials. The e-beam process with multiple-angle evaporation is illustrated in Fig. 3.7.

Since the microscope does not continuously expose the sample when it is in the write mode, a center-to-center (c-to-c) distance as well as a line spacing (l-to-l) needs to be specified in the Nabity program [51]. The former represents the spacing between individual doses along a line, with a minimum value of 28 Å. Using a smaller c-to-c distance results in a smoother line exposure, with a shorter exposure time for each point. However, given that there is a limit to how fast the beam can be blanked, about $3\,\mu s$, the overall exposure time per point should be much longer to ensure consistency. The l-to-l determines the distance between exposure of different lines, with a minimum value of 28 Å. Typical beam current for writing is around $6 - 24$ pA and, due to drifts with time, should be measured just before exposure. Since small

feature sizes require smaller exposure doses, lower values of current as well as smaller c-to-c and l-to-l values generally yield better results.

The bilayer resist mentioned above requires an area dose of $250 - 300\,\mu C/cm^2$ for development, whereas the undercut develops with an area dose of $80 - 100\,\mu C/cm^2$. Individual line doses are usually higher ($2 - 4\,\mu C/cm$) as they do not benefit from the proximity effect due to secondary electrons from a nearby exposed area. A comparison of line dose with an area dose requires the specification of a nominal linewidth. The size of the patterns, written with DesignCAD LT2000, should not exceed the maximum allowable area for the selected magnification (indicated by the Nabity NPGS program) as this will cause an error during writing and may result in exposure of unwanted areas in the resist.

3.2.4 Alignment

Before writing, an alignment program must be utilized in order to locate and accurately make contact with the optically patterned Ti/Au leads. The alignment program is designed with "windows" and "overlays" that match existing alignment marks for different magnifications. Since at this point, the substrate has e-beam resist on it, the time taken for alignment should be as short as possible, otherwise the sensitivity of the resist will decrease and unwanted areas may be exposed.

At low magnification (roughly 20x), the microscope is changed from "Pic" to "Line" Scan mode (which reduces the exposure) and the substrate is mechanically moved and rotated such that the center of the sample roughly aligns with the CRT screen of the microscope. The leads and large alignment marks serve as guides to the eye for rough alignment. The magnification is gradually increased to 200x and adjustments are made to center the sample. Once a rough visual alignment is obtained, the beam is set to computer control, which by default is blanked. The alignment program will scan only in the selected windows showing the overlays and the real alignment

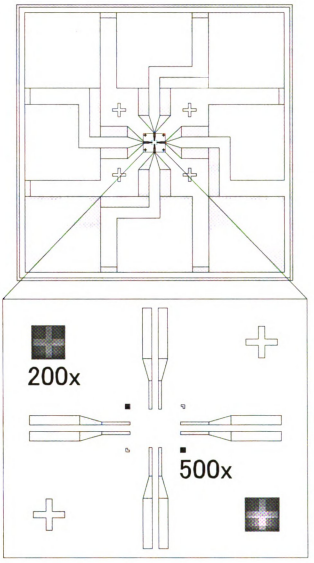

Figure 3.8: The alignment marks are found by roughly positioning the sample at low magnification, then scanning for the alignment marks at 200x and 500x, respectively (denoted by the dark squares over the marks). The rotation/translation matrix is recorded and included in the write sequence.

marks, whose locations will be different. The overlay for each individual alignment mark can be moved with the keyboard arrows, such that it coincides with the imaged mark from the sample. Pressing the "Insert" key toggles between the different marks. Once complete, the "Enter" key will record the translation/rotation matrix between the marks and overlays, which is then used to locate the smaller marks at 500x, where the alignment process is repeated. The final matrix (accounting for both magnifications) is used in conjunction with the write sequence to obtain proper alignment. The 6 μm alignment marks enable an accuracy of alignment of 50 nm [51]. It is worthy to note that there is a shift when changing magnification from 200x to 500x, which needs to be accounted for in the alignment and write program, i.e. (-3.1, 8.75) μm for the x and y directions, respectively. Compensation for the shift from 500x to 850x is (-1, +2.25) μm.

3.3 Measurements

Measurements performed on our samples were magnetic and resistive. Magnetic materials can be characterized using a variety of methods, such as surface probe techniques (Magnetic Force Microscopy) for thin films, photonic probes (using the magneto-optical Kerr effect), and SQUID magnetometry (described in the next few sections) for bulk samples. The latter technique is well suited for samples in our proximity effect experiments, giving information about the switching behavior and quality of the magnetic layers. We use this method almost exclusively for magnetic verification and it will be described in the next few sections.

Resistance measurements come in a variety of forms based on the sample type, size of the signal to noise ratio and measurement environment. For our experiments, we have used DC measurements, lock-in AC measurements and a low resistance method involving a SQUID-based potentiometer circuit. These will be described in subsequent sections.

3.3.1 SQUID

The standard technique for detecting small magnetic flux involves the use of a Superconducting Quantum Interference Device (SQUID). This device is made of a superconducting loop with one (rf SQUID) or two (dc SQUID) Josephson junctions (for review see [52]). A change in the applied flux to the loop will cause currents to flow to oppose that change. As a result, in the case of a dc SQUID, a phase difference appears across each Josephson junction which in turn gives rise to a measurable voltage across the loop.

For a constant bias current above the critical current, $I_{bias} > I_c$, the SQUID voltage, V_S, as a function of the applied flux, Φ_A, is sinusoidal with the period of a flux quantum, Φ_0 (see Fig. 3.9 (a) and (b)). To linearize the response, the SQUID is typically run in flux-locked loop (FLL) mode, where an additional modulated applied flux is used to maintain the voltage at an extremum in the V_S vs. Φ_A curve. Fig. 3.9 (c) illustrates how the SQUID is coupled inductively to the external flux and its modulating flux scheme. Due to the SQUID's sensitivity to fluctuations in magnetic field, it is shielded from other flux sources. At a minimum, the SQUID response signal occurs at twice the frequency of modulation due to the quadratic shape of the curve, and the lock-in will output no signal. However, if the dc flux strays from the extremum, then the lock-in will output a dc voltage proportional to the amplitude of the signal at the modulation frequency. The dc signal is integrated and fed back into the modulation coil, returning the flux to the value at the extremum. However, if the external flux changes too quickly, then the SQUID jumps from one extremum to another, and in so doing is said to have "lost lock."

3.3.2 Magnetic Characterization

For all our magnetic measurements we have utilized a commercial Quantum Design MPMS XL system with temperature control over the temperature range of 2-400

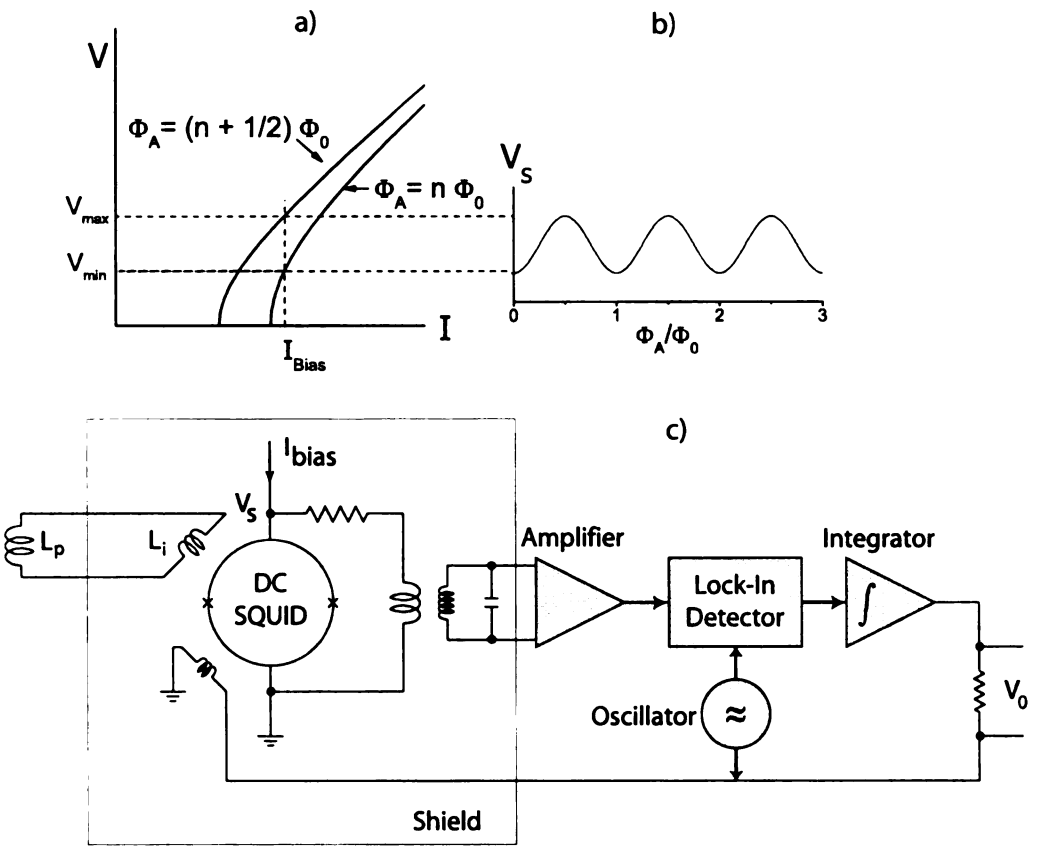

Figure 3.9: a) V-I Characteristic of dc SQUID with integer and half integer flux quantum, Φ_0, of applied flux. b) Biasing the SQUID above the critical current, I_C, and applying an external flux results in a sinusoidal behavior of the V_S vs. Φ_A curve. c) A superconducting pick-up coil couples the external flux to the input terminal of the SQUID. In flux-locked loop (FLL) mode an additional modulated flux is utilized to maintain the SQUID in an extremum of the V_S vs. Φ_A curve, obtaining a linear response of the SQUID to the applied flux.

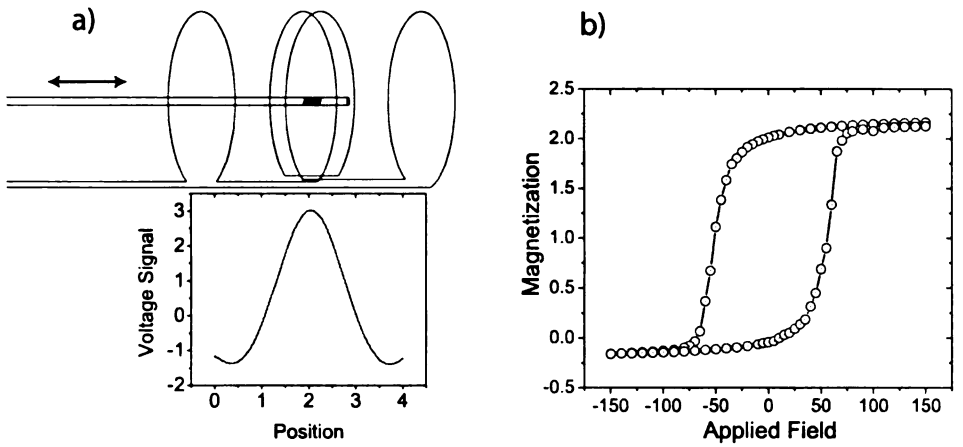

Figure 3.10: a) Voltage signal profile as a magnetic sample is moved through a second order gradiometer. The sign and size of the signal indicates the magnetic response of the sample, which is translated to a net magnetization. b) Typical ferromagnetic behavior as a function of an applied field for an F/S/F trilayer structure.

K. The measurement is performed by moving the sample through superconducting detection coils whereby the change in flux produces currents that are inductively coupled to the SQUID by an input coil (shown schematically in Fig. 3.9 (c)). The detection coils consist of superconducting wire wrapped in a second-order gradiometer configuration to reduce noise in the detection circuit. The SQUID functions as a linear current-to-voltage converter, so that current variations in the detection coils produce corresponding variations in the SQUID output voltage, which are proportional to the net magnetic moment of the sample. The typical response as a function of the position of the sample with respect to the center of the gradiometer is illustrated in Fig. 3.10 (a).

By applying an external magnetic field and measuring the SQUID response, the magnetic switching behavior for single or multilayers can be traced for temperatures as low as 2 K. Fig. 3.10 (b) shows the ferromagnetic response of a F/S/F trilayer structure, with nominally identical magnetic layers. One layer is free rotate while the other remains fixed.

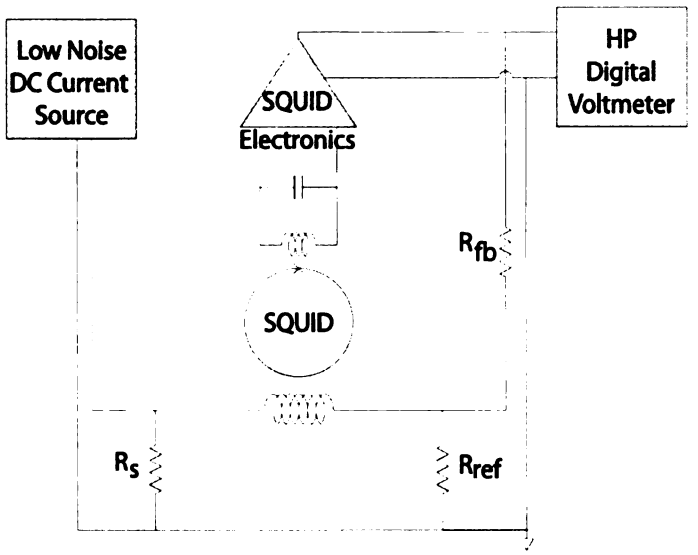

Figure 3.11: A low-temperature potentiometer circuit in feedback mode for measuring resistances in the nΩ range.

3.3.3 Low Resistance Measurement (CPP)

One very useful application for the SQUID's sensitivity to small changes in applied flux is its ability to detect extremely small resistances. Samples, such as those shown in Fig. 3.3, have currents flowing perpendicular to the several nm-thick layers, with resistances as small as a few nΩ. They require extremely sensitive, low noise measurement methods.

Fig. 3.11 shows the schematic for a SQUID-based electronics circuit which balances a low-temperature potentiometer by supplying a current into a reference resistor [53]. A low noise DC current, I_s (typically 100 mA), is provided to the unknown sample resistance, R_s. Current flowing through the inductor connected in parallel will be detected by the SQUID. The SQUID electronics then supplies a current to the reference resistor ($R_{ref} \approx 100\,\mu\Omega$) to null out the imbalance, and the voltage across the feedback resistor ($R_{fb} = 10\,k\Omega$) is measured. In equilibrium the voltage across the sample will be equal to the one across the reference resistance. Therefore, the

resistance (in nΩ) of the sample is given by

$$R_s = \left(\frac{V_{out}}{I_s}\right)\left(\frac{R_{ref}}{R_{fb}}\right) \tag{3.1}$$

where V_{out} is the output voltage (in Volts) read by the Keithley DMM. This equation is valid for sample resistances much less than 100 $\mu\Omega$. The small correction due to the finite open-loop gain of the feedback system is not included above.

3.3.4 Resistance Measurements (CIP)

All CIP resistive measurements at temperatures above 2 K were done using variable temperature Quantum Design MPMS SQUID system. In the standard way, a DC current source with current values ranging from 10 μA to 1 mA and a digital voltmeter were used, with typical sample resistances around several Ohms. No special care with respect to mounting is necessary for samples with lateral dimensions in the mm regime.

For those samples that were measured at temperatures below 2 K using a dilution refrigerator, an AC lock-in technique was utilized. Fig. 3.12 illustrates a schematic of the circuit. The lock-in provides a sinusoidal RMS voltage, where $V_0 \sim 1$ V, and the large ballast resistor ($R_B = 100$ kΩ) determines the current (typically a few μA) passing through the sample resistance, R_S. A pre-amplifier of gain (g = 100.4) boosts the signal, which is then detected by the lock-in at the driving frequency (chosen to be $f = 228$ Hz for our experiments). The output voltage of the lock-in is read by a Keithley Digital Multimeter, i.e. V_{DMM}.

The sample resistance using the lock-in is then

$$R_S = \left(\frac{R_B}{V_0}\right)\left(\frac{1}{g}\right)\left(\frac{sens}{10\,V}\right) V_{DMM} \tag{3.2}$$

where *sens* denotes the lock-in sensitivity and the 10 V is the maximum range of

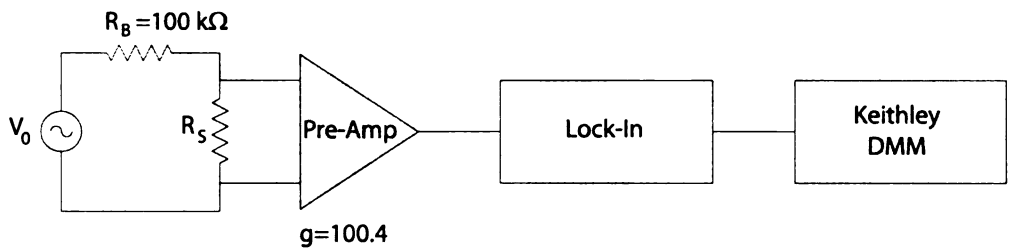

Figure 3.12: Experimental schematic of measurement circuit using lock-in. This method was utilized to measure samples at low temperatures in our dilution refrigerator.

the lock-in output. The 100 kΩ ballast resistor value, shown in Fig. 3.12 must be supplemented by a 4.5 kΩ resistance due to the filters that are present on the dilution refrigerator cryostat.

3.4 Cryogenic Methods

Standard methods for attaining temperatures below 300 K involve the use of cryogenic liquids, such as Nitrogen and Helium. All of the equipment utilized for this thesis takes advantage of the temperatures of these liquids. Liquid Nitrogen (LN_2), in addition to its ability to lower the temperature to 77 K, is used to reduce the pressure of vacuum systems by freezing out water vapor and other system contaminants.

Helium (^{4}He) is liquid at 4.2 K at ambient pressure. Obtaining a temperature below 4.2 K requires reducing the vapor pressure above the liquid, and in so doing reducing the overall thermal energy. This cooling by evaporation principle is applied to the dilution refrigerator, which will be described in the next section.

3.4.1 Dilution Refrigeration

A dilution refrigerator utilizes a ^{3}He/^{4}He mixture and takes advantage of a phase separation at low temperature to provide cooling. For all experiments in the temperature range 35 mK - 2 K, we have utilized a closed-cycle, continuous-operation,

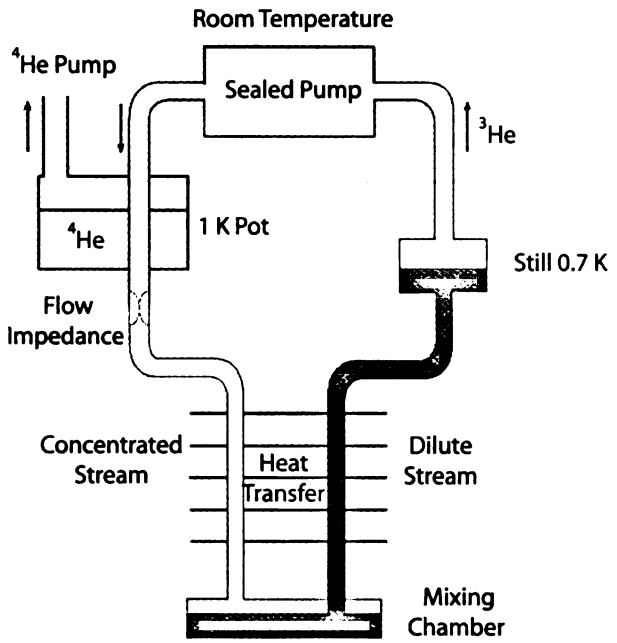

Figure 3.13: Dilution Refrigerator scheme.

top-loading Oxford system, Model 200 TLM.

At low enough temperature, phase separation occurs in a mixing chamber, where the lighter, concentrated phase is rich in ^{3}He, and the heavier, dilute phase is rich in ^{4}He. Since the enthalpy of the two phases is different, the transition from the concentrated into the dilute phase provides highly effective cooling. This process occurs even at the lowest temperatures because the equilibrium concentration of ^{3}He in the dilute phase is finite even at zero temperature. During operation, ^{3}He is extracted from the dilute phase and resupplied to the concentrated phase. The bulk of the dilute phase contains mostly ^{4}He which is inert and noninteracting, and may be neglected. The ^{3}He is pumped away from the liquid surface in a still container (kept at T $\approx$ 0.7 K for maximum efficiency). The ^{3}He evaporates preferentially about a thousand times faster as compared to ^{4}He. The ^{3}He leaving the mixing chamber is used to cool the returning flow of concentrated ^{3}He by a series of heat exchangers. A room temperature, a sealed vacuum pump is used to remove ^{3}He from the still

and compress it before passing it through impurity-removing filters and cold traps (at 77K and 4.2K) and subsequently returning it to the cryostat. The mixture is pre-cooled by the main helium bath provided by the dewar and condensed in a 1K pot. A capillary tube flow impedance is used to maintain a high pressure in the 1K pot region for the gas to condense. Fig. 3.13 illustrates the process pictorially.

The experimental device is mounted on a top-loading probe, which is then inserted directly into the mixing chamber, through the use of a dual seal, vacuum-tight load-lock system. The temperature is monitored by calibrated thermometers mounted in close proximity to the sample.

Chapter 4

Critical Temperature of FSF Trilayers

4.1 Introduction

One method of investigating the proximity effect of a ferromagnet in contact with a superconductor is to study Ferromagnet/Superconductor/Ferromagnet trilayers. This system is similar to the problem of an F/S bilayer, with the added feature that the magnetization direction of the two ferromagnetic layers becomes relevant. This aspect is illustrated in the suppression of critical temperature, T_C, which is different based on mutual orientation of the outer ferromagnets. The parallel (P) and antiparallel (AP) alignment will produce a different net exchange field experienced by the superconductor, which consequently affects the T_C differently. As the thickness of the superconductor is reduced, the sensitivity to the two orientations is enhanced and the effect becomes more pronounced. This behavior has been theoretically predicted [54, 55] and later observed in a system with a weak ferromagnet, namely Ni_xCu_{1-x}/Nb/Ni_xCu_{1-x} [11, 56].

Interest in these experiments were motivated by an intriguing theoretical prediction by Bergeret *et al.* [29], stating that a triplet order parameter can be induced in

a conventional superconductor in a F/S/F structure if the magnetization of the two ferromagnets are non-collinear. In order to provide experimental confirmation, a good F/S system must be found, which requires investigation in the parameter space of material properties and thickness ranges. The common belief that weaker ferromagnets are less devastating to superconductivity has restricted many F/S experiments to using weakly ferromagnetic alloys, with smaller exchange fields and weaker proximity effects. Therefore, the influence of strong ferromagnets on superconductivity, with their very different densities of states and Fermi velocities for the majority and minority spin bands, has neither been extensively investigated nor integrated well in theoretical treatments. It is the goal of this thesis to investigate the F/S system in the strong ferromagnet limit in order to obtain the maximum proximity effect behavior, which is needed for the observation of the predicted triplet state.

It is difficult to choose *a priori* the correct set of materials that gives the best quality interface since the transparency is intrinsically dependent on the electrostatic potential barrier between them. Miscible materials are not desired due to interfacial alloy formation while perfectly immiscible ones lead to non-wetting and island growth. Consequently, metals with restricted solubility and narrow composition ranges of intermetallic compound formation should be considered [57]. Moreover, the substrate type, surface quality, and growth conditions also affect the interface roughness and transparency. Potential choices are Fe, Co, Ni, and Gd for the ferromagnets and Nb, Pb, and V for the superconductors, producing a variety of F/S combinations.

This chapter presents the results of measurements on the T_C behavior based on the P and AP orientation of the ferromagnets for a Ni/Nb/Ni [31]. This experiment is a prerequisite to the one predicted by Bergeret *et al.*, as strong proximity effects indicate good candidates for the observation of the triplet state. Results on the $Ni_{0.8}Fe_{0.2}/Nb/Ni_{0.8}Fe_{0.2}$ system are also presented.

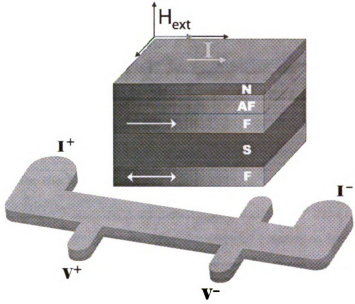

Figure 4.1: Ferromagnet/Superconductor/Ferromagnet experiment in a CIP spin-valve geometry. The top ferromagnet layer is pinned by an anti-ferromagnet and the magnetization of the bottom layer is free to rotate. The entire structure is covered with a non-superconducting metal to prevent the anti-ferromagnet from oxidation. The measurement current and applied field are both in the plane of the 4-terminal device.

4.2 Ni/Nb/Ni trilayers

In our studies, we want to understand the role that strong ferromagnets play in proximity effect experiments, specifically in the F/S/F heterostructure. For this experiment, we have fabricated macroscopic samples in the standard exchange-biased spin-valve configuration (shown in Figure 4.1) due to its well-defined magnetic structure. The first set of samples were Ni(7)/Nb(d_S)/Ni(7)/FeMn(8)/Nb(2) (all thicknesses in nm), where a variable thickness superconducting Nb layer was surrounded by two nominally identical ferromagnetic Ni layers of fixed thickness. The purpose of the FeMn is to pin the magnetization direction of the top Ni layer by exchange bias [58]. The thin Nb layer covering the entire structure is not superconducting and is used to prevent oxidation, which may affect the quality of the exchange bias.

Several experiments on the F/S system [7, 8, 57, 59] have shown T_C oscillations due to variations in the thickness of the ferromagnet. Specifically for the Ni/Nb system bilayer [57], these oscillations disappear for $d_F > 4$ nm. Therefore, we have chosen our Ni layers to be 7 nm, much longer than ξ_F, in order to eliminate variations in T_C due to small changes in the nominal thickness of the ferromagnets. The thickness of the FeMn, i.e. $d_{AF} = 8$ nm, produces a blocking temperature of around 180°C. The chosen thickness for the Ni layer combined with that of the FeMn gives an exchange bias field around 500 Oe.

The structure is sputter-deposited directly onto Si substrates in a high vacuum chamber with a base pressure of $2 - 4 \cdot 10^{-8}$ Torr and an Ar pressure of $2 \cdot 10^{-3}$ Torr. Typical growth temperatures are between 0°C and -20°C. After deposition, the samples are heated to 180°C in an evacuated pinning chamber, just above the blocking temperature of FeMn, and rapidly cooled in a field of 200 Oe applied in the plane of the sample. The entire pinning procedure takes no more than 7 minutes, thus limiting interlayer diffusion at high temperature. In this manner the magnetization of the top Ni layer gets fixed in the direction of the applied pinning field, while the bottom Ni layer is free to rotate.

4.2.1 Magnetization

Before making T_C variation studies, preliminary measurements were performed in order to verify the magnetic configuration of the multilayers. Each 0.5" x 0.5" sample chip has a 4-probe geometry as well as a 9.4 x 5.1 mm^2 rectangular pattern used for M vs. H measurements. This was achieved by simultaneous sputtering through the CIP-type mechanical mask shown in the previous chapter, Fig. 3.2 (a). Hence, both the 4-terminal T_C measurement and its magnetic behavior can be obtained for the same sample. Magnetizations were measured in a Quantum Design SQUID Magnetometer system with a temperature range of $2 - 400$ K. The samples were mounted such that

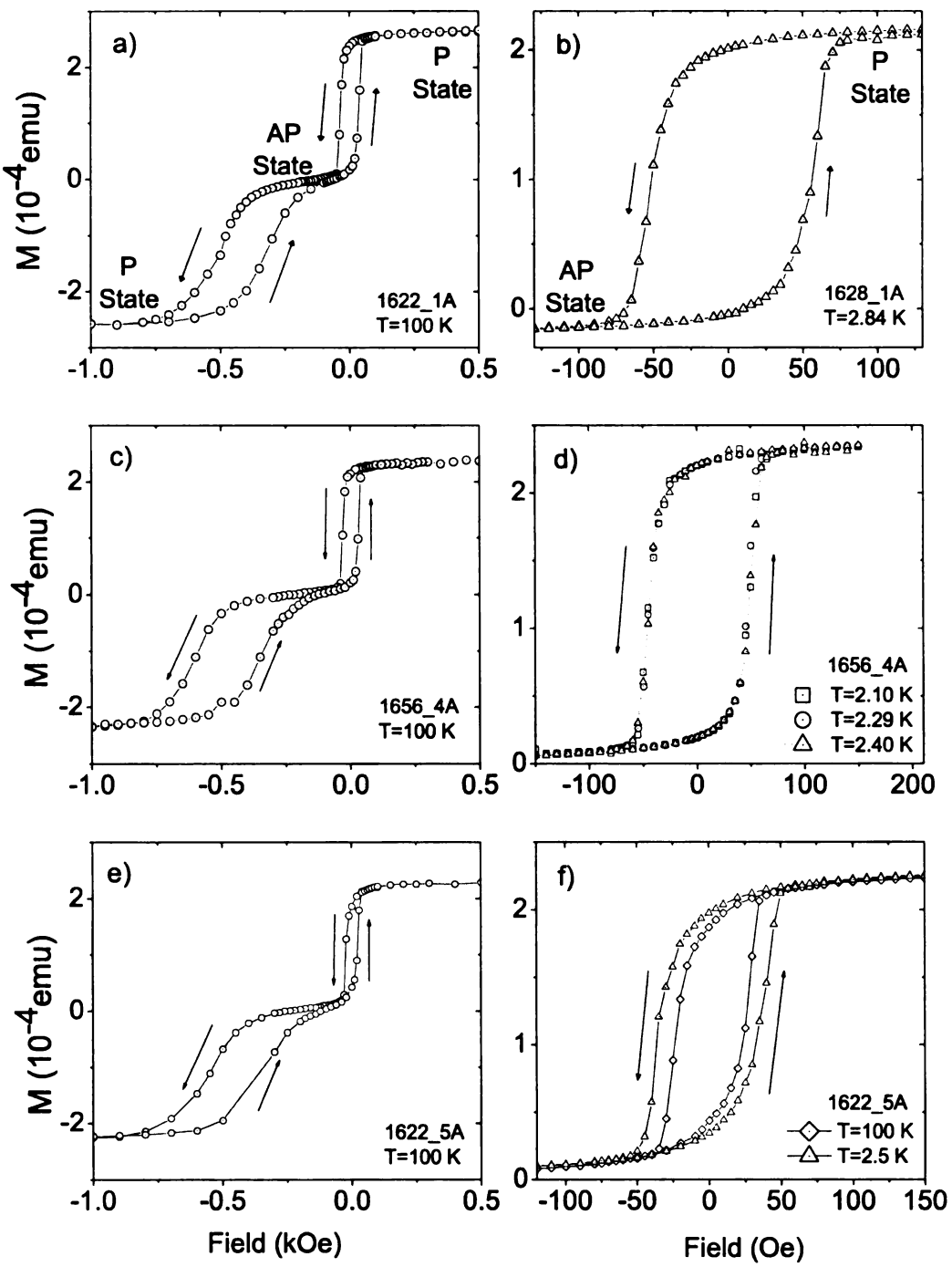

Figure 4.2: M vs. H for several Ni(7)/Nb(d_{Nb})/Ni(7)/FeMn(8)/Nb(2) samples at different temperatures The data illustrate good switching behavior and pininng of our magnetic layers. The T_C and d_{Nb} for each sample is given in Table 4.1.

the pinned direction of the top Ni layer was aligned along the positive direction of the external applied magnetic field, in the plane of the samples. Fig. 4.2 shows minor and major M vs. H curves for several Ni/Nb/Ni/FeMn samples taken at high (100 K) as well as low temperatures. Their magnetic behavior is consistent with that of a standard spin-valve.

Taken at 100 K, Fig. 4.2 (a) shows the typical full switching behavior of our heterostructures. An applied field of $H = +500$ Oe aligns both of the Ni layers parallel to each other with a saturation magnetization of $M_S = 2.66 \cdot 10^{-4}$ emu. As the field sweep is swept toward zero, the remnant magnetization is $M_R = 2.38 \cdot 10^{-4}$ emu. This result indicates good ferromagnetic behavior for the Ni layer grown directly on the Si substrate with no buffer layer. At $H = -35$ Oe the bottom free Ni layer switches abruptly and the AP state is reached. Since the net magnetization in the AP state is essentially zero, the trilayer system is fairly symmetric. Further increasing the field towards larger negative values results in a gradual depinning of the top Ni layer, with complete switching to the P state at around $H = -1000$ Oe. Upon reducing the field back towards zero, the repinning of the top Ni can be observed, with a full recovery of the AP state at around $H = -60$ Oe. At $H = +35$ Oe the free layer quickly switches back, and once again the P state is obtained. However, sweeping the field to large values against the pinning direction may affect the recovery of the exchange bias, especially at lower temperatures. Since we are only interested in the P and AP states, we have limited most of our magnetic sweeps to minor loops at low temperatures, which do not involve the depinning of the top Ni layer.

As our resistance measurements are performed at temperatures between $0.03-9$ K, the magnetic behavior must also be verified at low temperatures. In this regime, the coercivity of the ferromagnet, H_C, increases since energy due to thermal fluctuations is no longer available to assist in switching. Therefore, the hysteresis loops observed at 100 K are expected to broaden for both the free and pinned Ni layers. This is well

illustrated in the minor loops of Fig. 4.2 (f), taken at 100 K and 2.5 K, where the loop with the larger H_C corresponds to a lower temperature.

It is also important to know whether any magnetic behavior changes take place as the superconductor in our F/S/F structures undergoes a superconducting transition. Fig. 4.2 (d) shows the minor loops for a sample at three different temperatures, i.e. T = 2.10, 2.29 and 2.40 K. These correspond to temperatures below, at and above T_C for this sample with d_{Nb} = 18 nm. Care was taken to sweep the temperature to the needed value in a zero applied field to prevent the trapping of magnetic flux in the superconductor. All three minor loops are in perfect agreement, with $H_C \approx 60$ Oe. This behavior is convincing evidence that applied fields with values slightly beyond H_C will firmly place our Ni layers either parallel or anti-parallel to each other at all measurement temperatures close to the transition. Since our Ni layers are nominally identical for all of our Ni/Nb/Ni experiments, we have used ±100 Oe to obtain the P and AP states, respectively.

4.2.2 Critical Temperature

Four-probe, DC or AC resistance measurements, with the current applied in the plane of the multilayer, were performed to determine T_C. Samples had lateral dimensions of 4.3 x 1.6 mm^2 (see Fig. 4.1). The T_C of each sample was defined to be the temperature at which the resistance dropped to half its normal state value. Fig. 4.3 shows T_C vs. d_{Nb} for a series of Ni(7)/Nb(d_{Nb})/Ni(7)/FeMn(8)/Nb(2) structures. The various symbols represent different sputtering runs. All resistance measurements for samples with $d_{Nb} > 24$ nm, were taken in a constant applied field of 100 Oe in order to have consistent T_C comparison with respect to thinner samples. The choice of measurement in a finite field will be addressed in the next section. For thinner Nb samples, all measurements were done in fields of +100 Oe and -100 Oe, corresponding to the P and AP configuration, respectively. The difference in T_C between the two

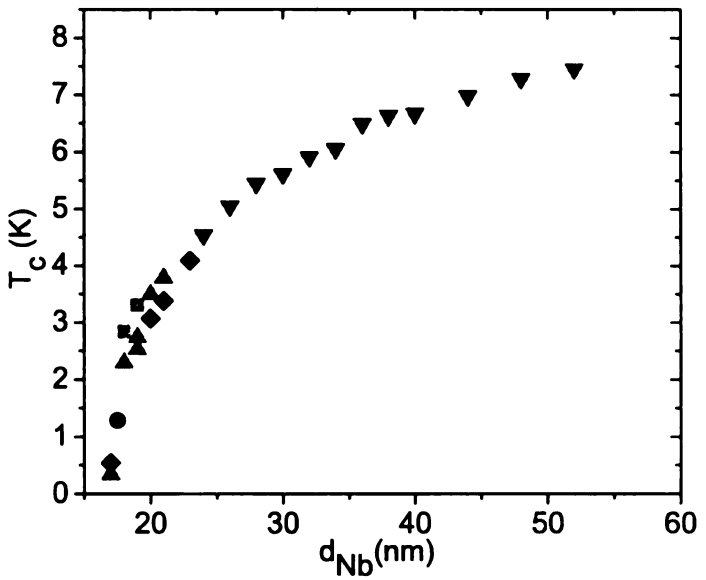

Figure 4.3: T_C vs. d_{Nb} for series of a Ni(7)/Nb(d_{Nb})/Ni(7)/FeMn(8)/Nb(2) samples. The various symbols correspond to different sputtering runs. Uncertainties in T_C are smaller than the size of the symbols.

orientations, however, is not visible on this scale.

The addition of the ferromagnets on either sides of a Nb layer suppresses its T_C from the value of an isolated film of the same thickness. For thick Nb layers, the T_C approaches a bulk value of 9.1 K. For samples with thicknesses close to a critical thickness, d_{Nb}^{cr}, the data show a very strong suppression of T_C. There is no superconductivity above 36 mK for samples with $d_{Nb} < d_{Nb}^{cr} \approx 16.5$ nm. Using the variable temperature capability of the Quantum Design MPMS system, R vs. T measurements of samples with T_C above 2 K were obtained, while a ^{3}He/^{4}He dilution refrigeration unit was used to measure those with $T_C < 2$ K.

4.2.3 ΔT_C Measurements

One important factor to consider when measuring minute differences in the critical temperature between the ferromagnet configurations, $\Delta T_C \equiv T_C^{AP} - T_C^P$, is the measurement of temperature. Performing separate R vs. T measurements for the

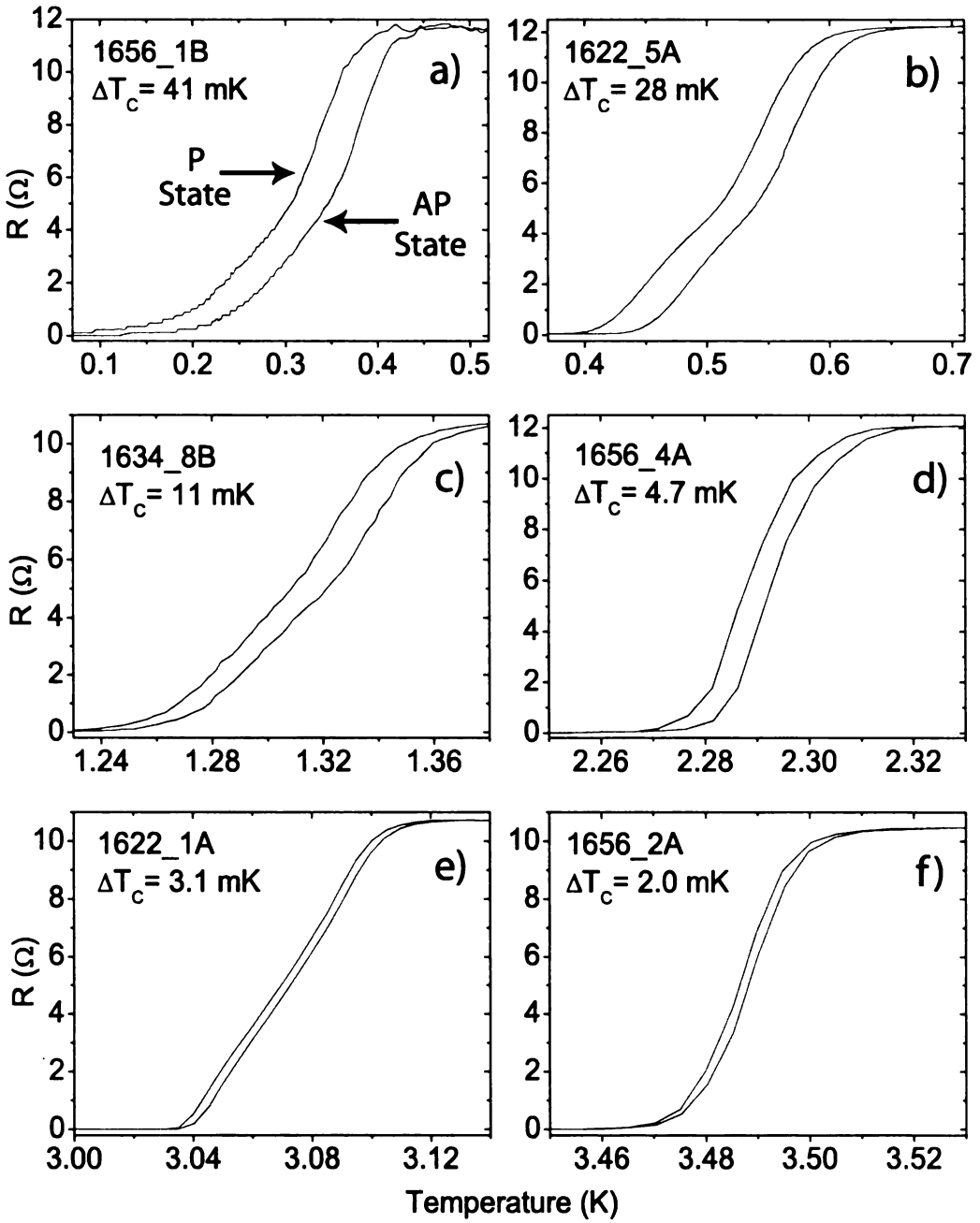

Figure 4.4: R vs. T for a set of Ni(7)/Nb(d_{Nb})/Ni(7)/FeMn(8)/Nb(2) samples in P and AP configuration. For all measurements, $T_C^{AP} > T_C^P$. Table 4.1 shows a summary of all information pertaining to each sample including d_{Nb} and the uncertainties in ΔT_C.

P and AP state may introduced unwanted errors due to drifts in the measurement of temperature from one sequence to the other, where each can take as much as an hour. Therefore, resistance measurements were always done either by fixing the temperature and measuring both field orientations, or by sweeping the temperature very slowly through the transition while alternating measurements between the two field directions. Furthermore, all samples were measured in an externally applied field, as opposed to zero field, so as to ensure that the trilayer was firmly in the P or AP state. The R vs. H data provides supporting evidence for this decision. Measurements in zero applied field, produced a slight decrease in the ΔT_C observed.

The largest shift in critical temperature should occur in samples with the Nb thickness close to d_{Nb}^{cr}. Fig. 4.4 shows data that display nonzero ΔT_C for several samples with nominal thicknesses close to d_{Nb}^{cr}, namely $d_{Nb} = 17, 17.5, 18, 19, 20$ nm. T_C varies from 330 mK to 3.49 K, with ΔT_C ranging from 41 mK down to a few mK, respectively. For all our samples, $T_C^{AP} > T_C^P$. Nominally identical samples can give significant differences in T_C and ΔT_C due to small thickness variations and the enhanced sensitivity of the Nb layer to the ferromagnets. This effect is evident by comparing the data in Fig. 4.4 (a) and (b), where both samples have nominal $d_{Nb} = 17$ nm yet the T_C and ΔT_C are quite different.

To understand our structures in more detail, we have performed a number of magnetoresistance (MR) measurements. Figure 4.5 shows four R vs. H plots, each illustrating data for temperatures at and above T_C for each particular sample. The applied field is swept from +150 Oe to −150 Oe and then back to +150 Oe. From previous M vs. H studies, this field is enough to reverse the free Ni layer while keeping the pinned Ni layer fixed. Increasing the magnetic field in the negative direction beyond −150 Oe will depin the top Ni layer and the P state can, in principle, be recovered, similarly to the major loops in the M vs. H curves. However, in order to accomplish this fields values $H > 500$ Oe are required, which in turn suppress

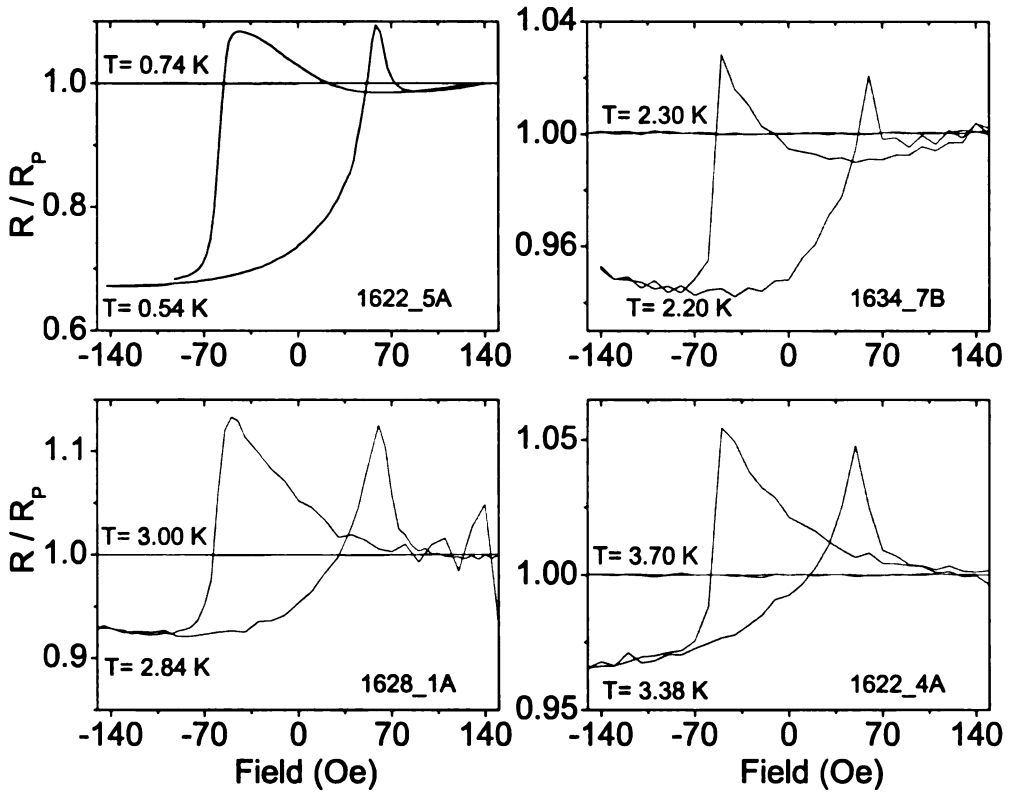

Figure 4.5: R vs. H for a set of Ni(7)/Nb(d_{Nb}))/Ni(7)/FeMn(8)/Nb(2) samples. All resistances are normalized to the P state resistance. Each plot illustrates the magnetoresistance at two temperatures corresponding to the middle and above the transition of each sample (see Table 4.1).

the superconductivity (fragile in the transition region). Consequently, the resistance increases substantially, making it difficult to observe the same P state resistance as compared to the one obtained from the minor loop. Furthermore, fully depinning the fixed Ni at such low temperature may prevent the recovery of the exchange bias. For this reason, a limited number of major loops were performed on these samples in order to verify the retrieval of the P state.

The R vs. H data is normalized to the resistance in the P state, R_P. All high temperature measurements, corresponding to the normal state for the Nb layer, show no appreciable MR on this scale. By contrast, the R vs. H measurements exhibit a significant change in resistance between the P and AP state for temperatures half-way

in the transitions. The values of the difference, ΔR, range from a few percent for samples with a high T_C up to 30% at the lowest temperature of 540 mK. Also, ΔR is somewhat sensitive to temperature over the range of the superconducting transition, depending on the shape and width of the latter. However, the general shape does not change over the transition.

One interesting feature that is present in all samples (shown in Fig. 4.5), is the behavior of the resistance as the field is swept down from +150 Oe towards −50 Oe and as the field is swept up from −150 Oe towards +50 Oe. In both cases, the resistance increases to a value higher than that of the P state after the field passes through zero. These results can be interpreted as stemming from the magnetic behavior of Ni close to the coercive field. While switching, the free Ni layer breaks up into domains whose fringing fields penetrate the adjacent superconductor, thus suppressing T_C slightly and producing a higher resistance. This was rather surprising since results from our magnetic measurements on the same samples (shown in Fig. 4.2) gave no indication of any anomalous behavior, except for the slight depression of the magnetization close to H_C from its value at saturation.

It is worth mentioning that the anomalous features in the R vs. H curves at H_C are *opposite* to what was observed by the group of Rusanov *et al.* [60, 61], where inhomogeneous magnetization led to enhanced superconductivity in F/S bilayers. In a similar work, the authors also structured Py/Nb/Py trilayers in strips of different sizes (both macroscopic and microscopic) and observed that the antiparallel alignment of the ferromagnetic Py layers yielded a higher resistance when compared to the parallel one [62]. A possible source for the difference may be related to the size of the domains in the ferromagnetic materials.

A summary of all the T_C difference data for all our Ni/Nb/Ni trilayers is shown in Fig. 4.6. ΔT_C is plotted as a function of the nominal thickness, d_{Nb}, for samples from several sputtering runs. Close to d_{Nb}^{cr} the difference in T_C increases dramatically,

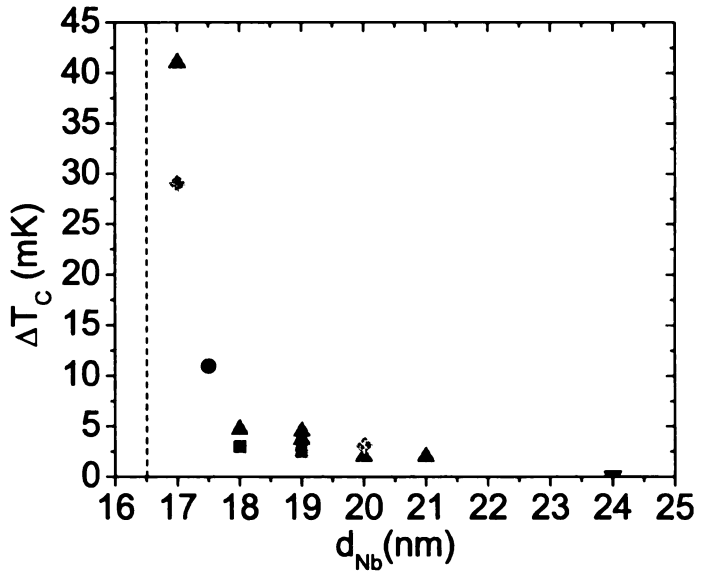

Figure 4.6: ΔT_C vs. d_{Nb} for Ni(7)/Nb(d_{Nb})/Ni(7)/FeMn(8)/Nb(2) samples. The dashed line represents $d_{Nb}^{cr} \approx 16.5$ nm. Uncertainties in ΔT_C are in the range of $0.3 - 1.0$ mK and are given in Table 4.1. Uncertainty in d_{Nb} is around 0.5 nm for all samples.

the largest value observed having $\Delta T_C = 41$ mK ($d_{Nb} = 17$ nm and $T_C = 0.33$ K). However, this value is smaller than the width of the superconducting transition for this sample. There is quite a bit of scatter in ΔT_C data, especially for samples with identical d_{Nb} close to the critical thickness. This comes from small variations in growth conditions, as well as deviations from the quoted nominal thickness, both of which strongly influence T_C in this thickness range. For those structures with $d_{Nb} \geq 24$ nm there is no observable difference in T_C between the P and AP state.

4.3 Py/Nb/Py trilayers

Permalloy (Py) is a $Ni_{0.80}Fe_{0.20}$ alloy with strong ferromagnetic properties and very low coercivity. Due to its low spin diffusion length, $l_{sf} = 5.5$ nm [63], Py is not a good candidate for a spin triplet experiment mentioned in the introduction to this chapter. However, recent intriguing results on the Py/Nb/Py system raised our interest with

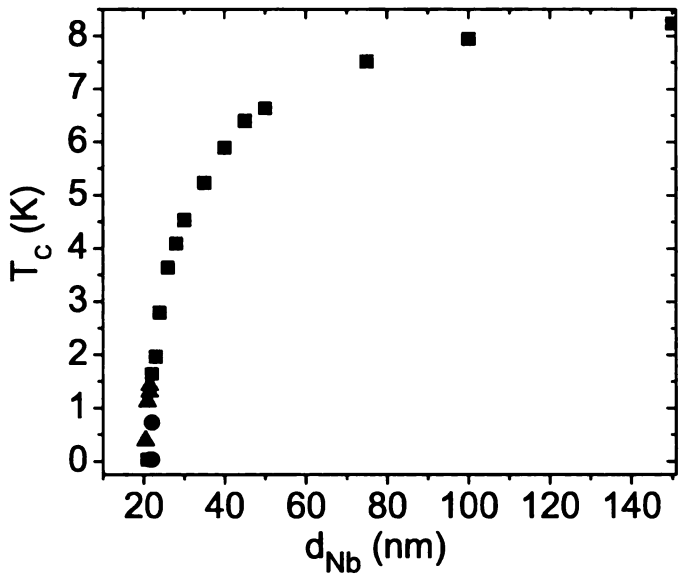

Figure 4.7: T_C vs. d_{Nb} for a series of Py(8)/Nb(d_{Nb})/Py(8)/FeMn(8)/Nb(2) samples. The various symbols represent different sputtering runs. The uncertainties in T_C are smaller than the symbol size.

regard to the Py/Nb system. In their experiment, Rusanov *et al.* [62] observed that the AP configuration of their ferromagnets was found to yield a higher resistance than the P state, a result directly opposite to what we had for our Ni/Nb/Ni structures. The two ferromagnets of their trilayer structure were fabricated with different thicknesses so that they can be switched independently by different field values. Based on their observations, the authors concluded that enhanced reflection of spin-polarized quasiparticles at the S/F interfaces of the trilayer in the AP state leads to a stronger suppression of superconductivity. The authors further suggested that the effect was generic for strong ferromagnets. These claims and observations have prompted us to fabricate of our own Py/Nb/Py spin valves in an attempt to investigate whether similar results can be obtained using Py deposited in our sputtering system.

In order to determine the optimal thickness range for the proximity effect on a Nb layer in contact with Py, we first measured T_C vs. d_{Nb} for several Py/Nb/Py trilayers. Fig. 4.7 shows the T_C for a series of Py(8)/Nb(d_S)/Py(8)/FeMn(8)/Nb(2) samples

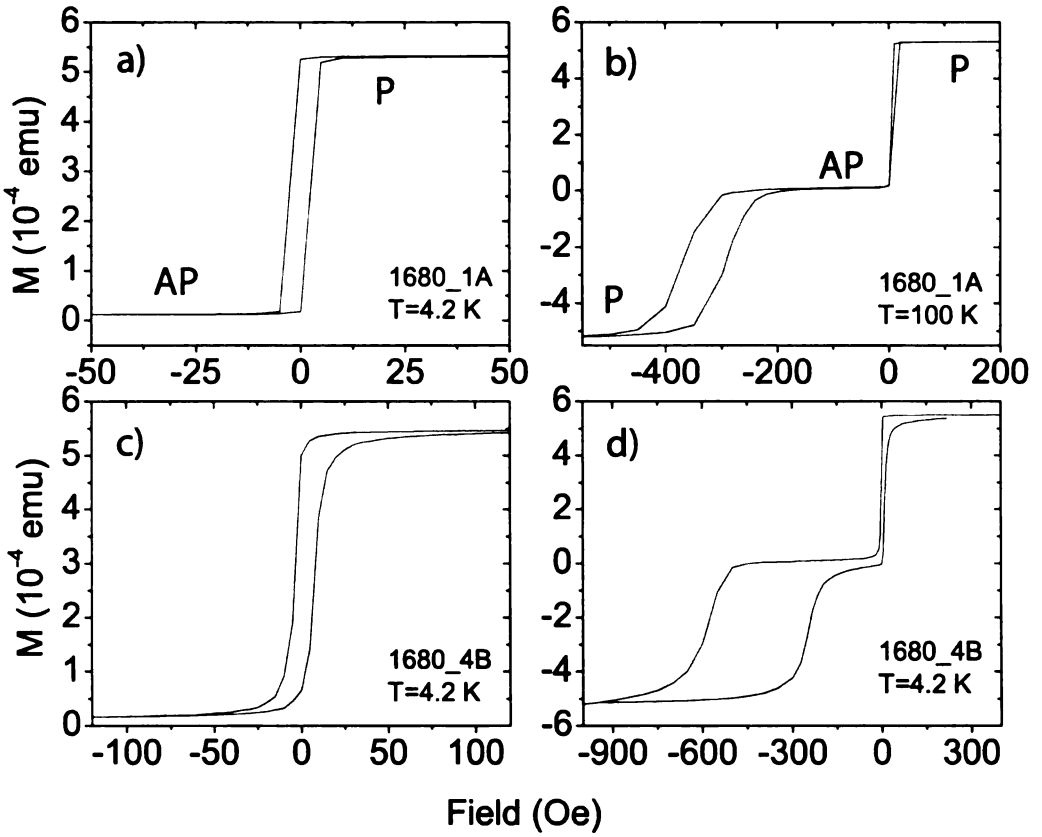

Figure 4.8: M vs. H for a set of Py(8)/Nb(d_{Nb})/Py(8)/FeMn(8)/Nb(2) samples. The top set corresponds to a sample with d_{Nb} = 23 nm while for the bottom d_{Nb} = 28 nm.

with Nb layer thickness varying from 20 to 150 nm. Our data indicate that the critical thickness below which the Nb in contact with two Py layers is not superconducting is $d_{Nb}^{cr} = 20.5$ nm.

In a similar manner as with our Ni samples, M vs. H curves were obtained for our trilayers in order to verify their magnetic structure. Fig. 4.8 shows the major and minor loops for two different samples. Fig. 4.8 (a) and (b) show the data of a sample with d_{Nb} = 23 nm taken at temperatures T = 4.2 and 100 K, respectively. Fig. 4.8 (c) and (d) shows data for a d_{Nb} = 28 nm sample taken at T = 4.2 K. Since Py is a ferromagnet with very little crystalline anisotropy, the coercive field is of the order of a few Oe, and increases only slightly at lower temperatures. Both minor loops show

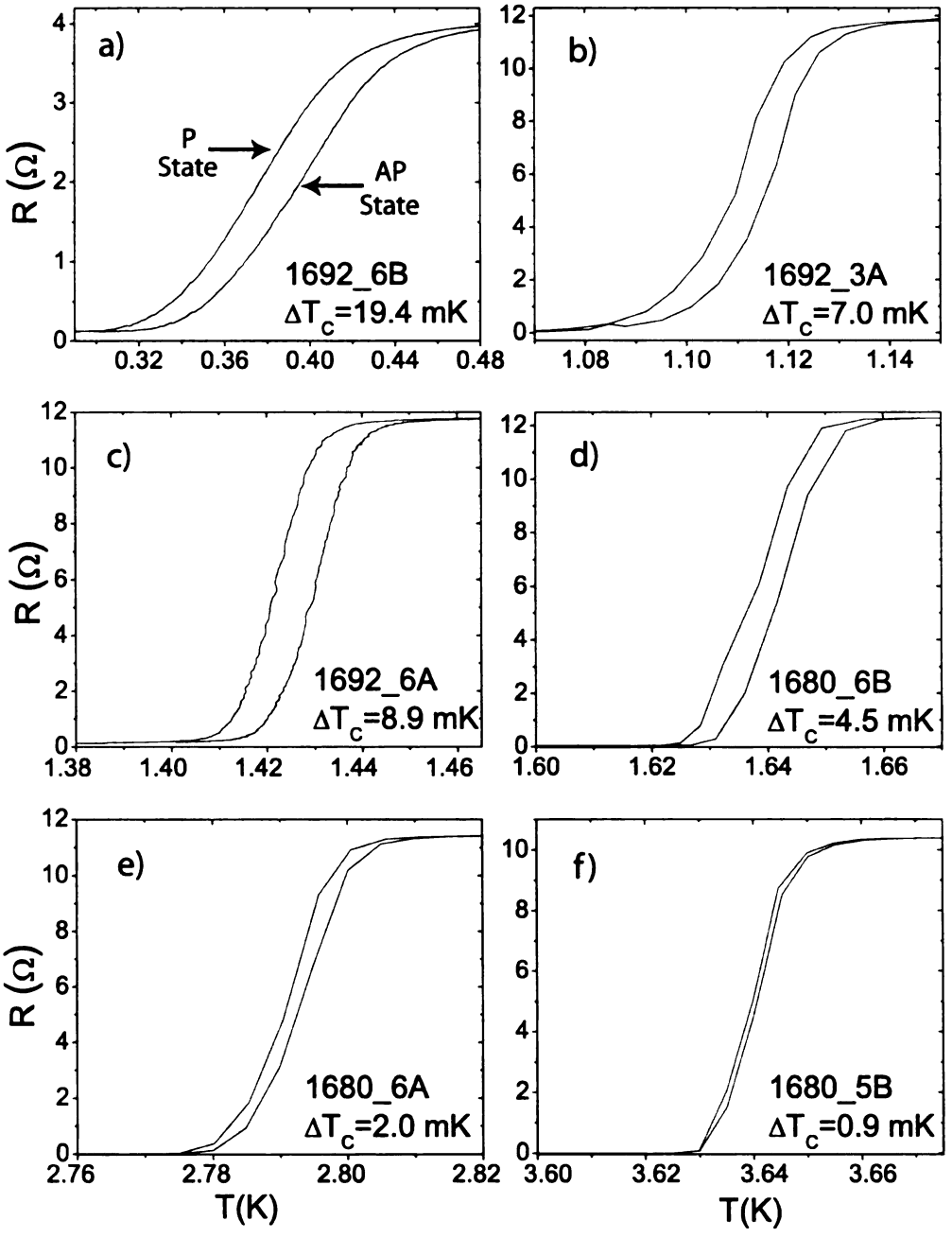

Figure 4.9: R vs. T for a set of Py(8)/Nb(d_{Nb})/Py(8)/FeMn(8)/Nb(2) samples in P and AP configuration. For all measurements, $T_C^{AP} > T_C^P$. The Nb layer thicknesses as well as the uncertainties in ΔT_C are given in Table 4.2.

switching of the free Py layer with clear distinction between the P and AP state. The major loops illustrate the magnetic behavior of the entire structure at higher field, including the depinning and repinning of the Py layer adjacent to the FeMn.

Critical temperatures in the P and AP configuration of the ferromagnetic Py layers were obtained from resistance measurements. The applied fields for the two states were +100 and -100 Oe. Fig. 4.9 shows different R vs. T curves for samples with different Nb layer thickness. Fig. 4.9 (a) shows data for a sample with $d_{Nb} = 20.5$ nm, which has the highest observed $\Delta T_C \approx 20$ mK. For thicknesses $d_{Nb} > 26$ nm corresponding to $T_C > 3.65$ K there is no measurable difference in critical temperature between the P and AP state. For all our Py/Nb/Py measurements T_C^{AP} is always greater than T_C^P, a result exactly opposite to earlier work by Rusanov *et al.*, but consistent with our Ni/Nb/Ni data.

We have also performed several R vs. H measurements on the Py/Nb/Py trilayers. These were taken for samples exhibiting a nonzero ΔT_C, at temperatures corresponding to the middle of their corresponding superconducting transitions. Fig. 4.10 shows data for three samples with $T_C = 385$, 705 and 1260 mK. Fig. 4.10 (b), (d) and (f) show minor loops with field sweeps between -100 and 100 Oe. Sample to sample variations in the magnetoresistance behavior and coercive field are much more visible as compared to data obtained from our Ni/Nb/Ni trilayers. The increase in resistance around the coercive field, which is always present in our Ni data, is pronounced in some of our Py samples, Fig. 4.10 (b), while absent in others, Fig. 4.10 (f). However, all samples clearly show a more resistive P state as compared with the AP state.

In addition, for each of these samples, their corresponding major loops were obtained at temperatures in the middle of their respective transitions, illustrated on the left hand side of Fig. 4.10. Plots 4.10 (a), (c), and (e) indicate clear transitions from P to AP and then back to P state as the field is swept from a large positive to a large negative value. This is illustrated by a sudden drop and then a broad increase

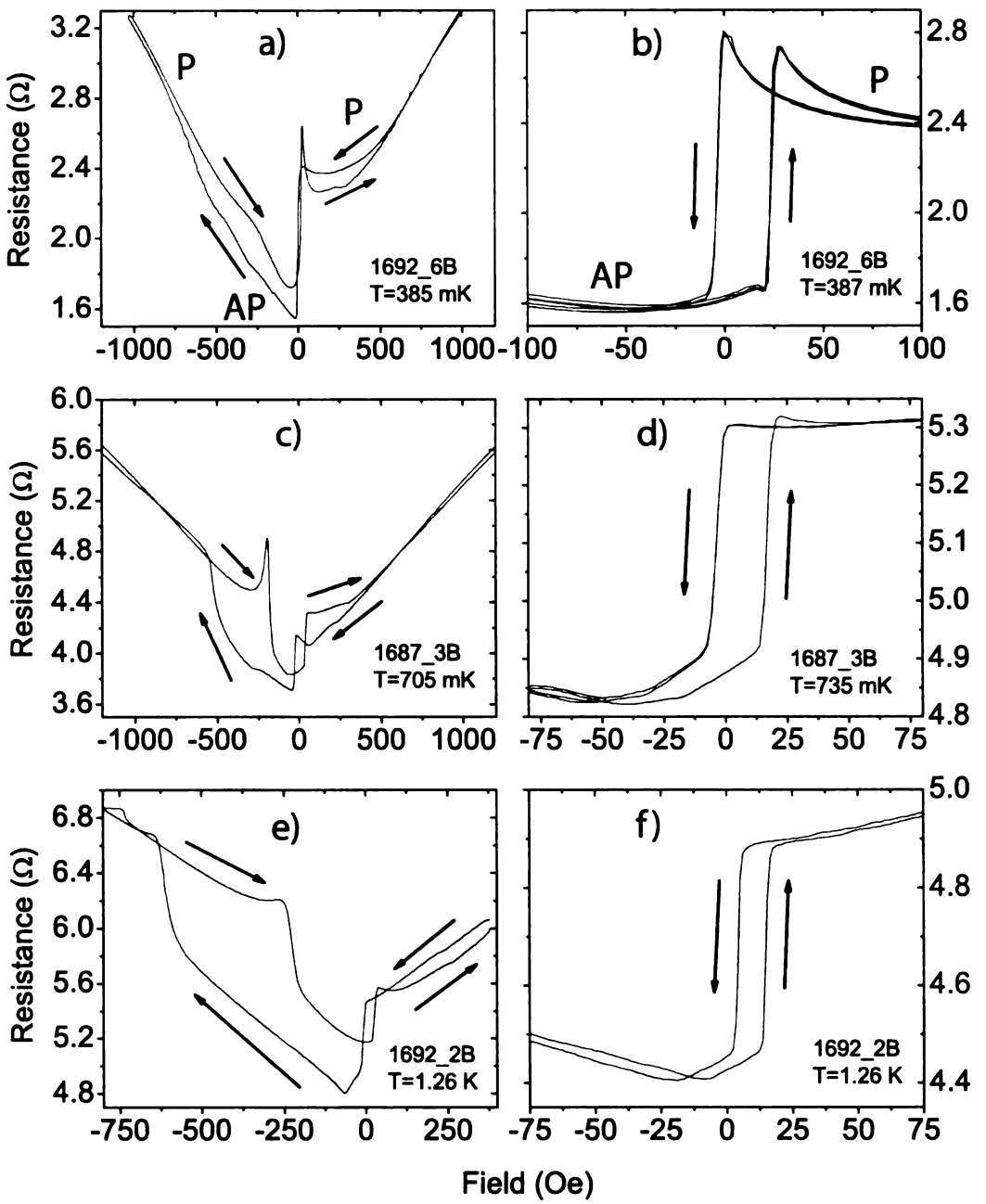

Figure 4.10: R vs. H for several Py(8)/Nb(d_{Nb})/Py(8)/FeMn(8)/Nb(2) samples. The field sweeps are taken at temperatures corresponding to the middle of the superconducting transition for each sample. The arrows represent the field sweep direction. The P state is always higher in resistance than the AP state. The Nb layer thicknesses are given in Table 4.2.

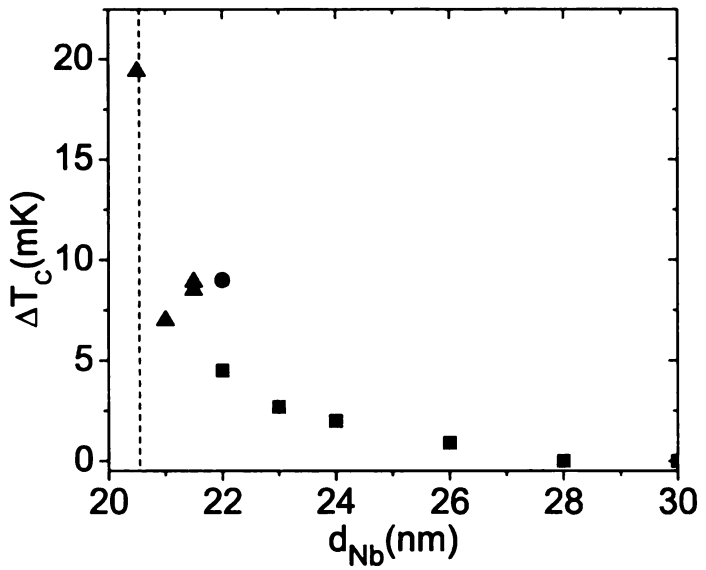

Figure 4.11: ΔT_C vs. d_{Nb} for a set of Py(8)/Nb(d_{Nb})/Py(8)/FeMn(8)/Nb(2) samples in P and AP configuration. The different symbols represent different sputtering runs and the dashed line represents $d_{Nb}^{cr} \approx 20.5$ nm below which there is no superconductivity. Uncertainties are given in Table 4.2.

in resistance, indicating the sharp switching of the free and the slow depinning of the fixed layer, respectively. The exchange bias field is around 500 Oe. The exact resistance response while repinning the top Py layer seems to be sample-dependent. The overall parabolic shape of R vs. H is due to the application of a large field, which suppresses superconductivity more strongly for both positive and negative values.

The strong dependence of ΔT_C on the Nb thickness is summarized in Fig. 4.11. The dashed line represents the minimum thickness for which superconductivity is observed, i.e. $d_{Nb}^{cr} = 20.5$ nm, for our Py/Nb/Py trilayers. The largest ΔT_C observed with Py is about 20 mK. The data appear quite scattered for thinnest Nb layers due to the increased sensitivity of T_C on small variations of thickness and growth conditions. From inspection of the R vs. H curves of Fig. 4.10, one should not be surprised about the size of the uncertainty in ΔT_C given the sample to sample variation observed in the magnetoresistance behavior. Nevertheless, the sign of ΔT_C is well established for all samples, namely that the P state is always higher in resistance than the AP one.

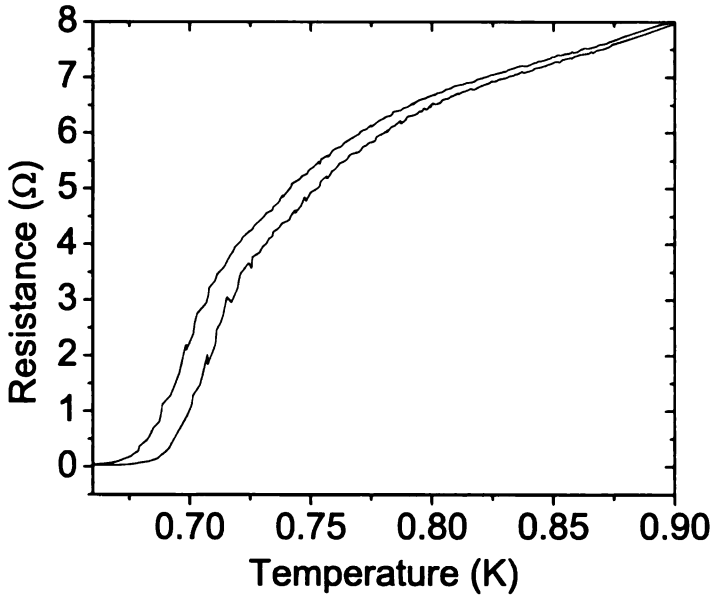

Figure 4.12: Resistance vs. Temperature for a Py/Nb/Py sample with $d_{Nb} = 22$ nm whose magnetoresistance data with respect to RMS drive is illustrated in Fig. 4.13.

Resistive determination of T_C for type II superconductors has been argued to pose some difficulties due to the presence of vortices, which are the result of quantized penetration of magnetic flux. Therefore, the measurement current applied to the superconductor becomes important as this may lead to additional dissipation due to non-equilibrium vortex motion. Although all ΔT_C data shown so far were measured using relatively small current values (10 μA AC), we have nevertheless verified the effect of different currents for a Py/Nb/Py sample with $d_{Nb} = 22$ nm, whose R vs. T data for the P and AP state is shown in Fig. 4.12 ($\Delta T_C \approx 10.5$ mK).

Figure 4.13 (a) shows several magnetoresistance curves obtained at a constant temperature that is roughly in the middle of the superconducting transition for this sample, namely $T_C = 734.8$ mK. The RMS drive amplitude was varied between 1 V and 0.124 V, which corresponds to currents between 10 μA and 1.24 μA. There is a small shift of the magnetoresistance curves towards higher resistance for data taken with a larger drive. In order to quantify the implications with respect to T_C and ΔT_C for different values of measurement current, Fig. 4.13 (b) shows the resistances for

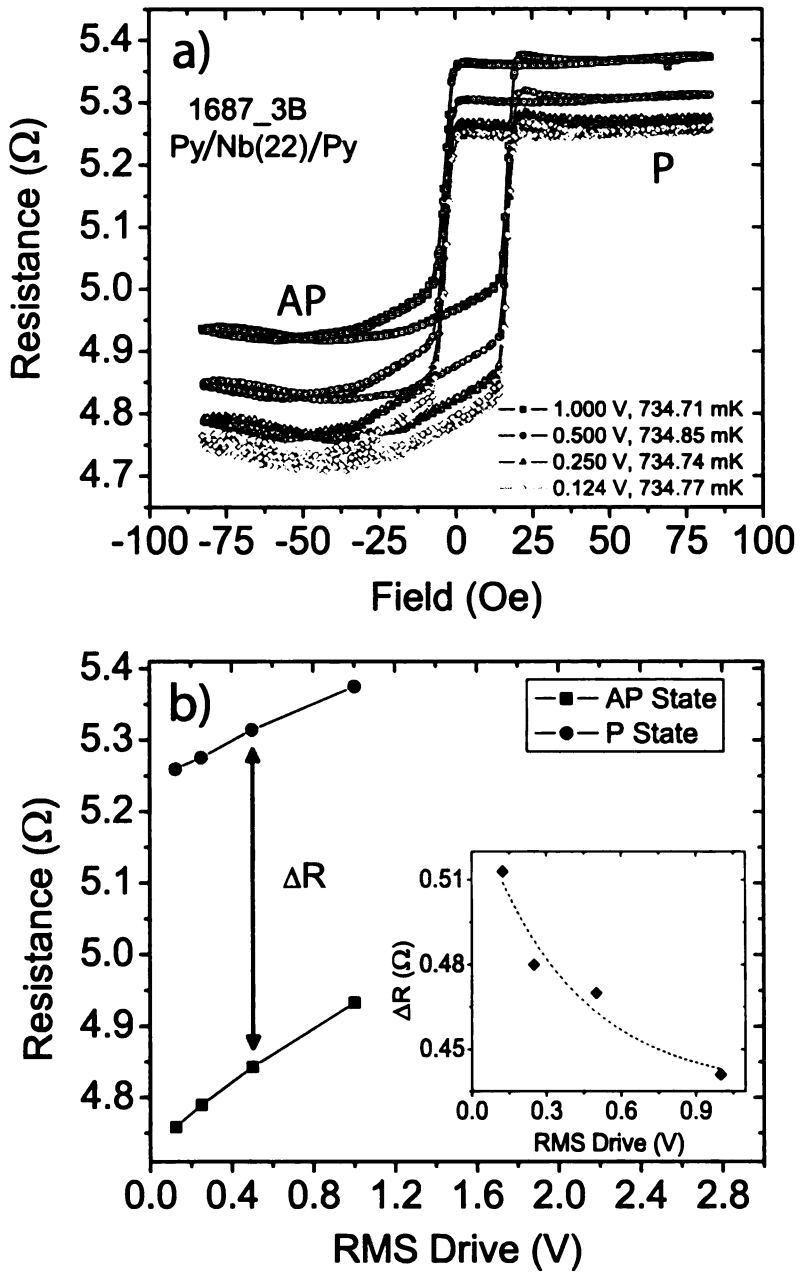

Figure 4.13: a) Resistance vs. Applied field for a Py/Nb/Py sample with $d_{Nb} = 22$ nm for several RMS drive amplitudes, ranging from 1 V to 0.124 V, corresponding to currents between 10 μA and 1.24 μA. b) R vs. RMS Drive for the P and AP states ($\pm$80 Oe). The difference in resistance between the two states as a function of drive is summarized in the insert. All measurements are taken at temperatures in the middle of the transition for this sample, $T_C \approx 734.8$ mK.

the P and AP state (at ±80 Oe) as a function of the drive. The P state resistance increases roughly linearly by 0.115 Ω between the lowest and highest drive, while that of the AP state increases by 0.174 Ω. The difference in resistance, ΔR, between the two states is plotted in the insert to Fig. 4.13 (b) for each drive amplitude. The dotted line is a guide to the eye and indicates a slightly larger ΔR for lower drives, with a difference between the highest and lowest value (1.0 and 0.124 V) of 0.072 Ω. Taking the slope of the R vs. T for this sample (Fig. 4.12) to be roughly $0.69\,\Omega/0.012\,\mathrm{K}$ at $T = 734$ mK, one can then estimate the difference in ΔT_C between the 1 V and 0.124 V drive to be about 1 mK, a value within the uncertainty. Similarly, T_C^P and T_C^{AP} decrease by 2 and 3 mK, respectively, when the drive changes from 0.124 V to 1 V. These results give strong indications that 10 μA measurement currents are low enough to be close to a linear response regime.

In summary, the results for our Py trilayer structures are different than those obtained by Rusanov *et al.*. The latter experiments involving both macroscopic and microscopic samples show an enhanced superconductivity when the two ferromagnets are in the P state, whereas we see exactly the opposite behavior in all our macroscopic samples. The only difference between our samples and those of Rusanov *et al.* is that we use exchange bias rather than different thickness ferromagnets to achieve the AP state. It is interesting to note, however, that a sample shown in that work, namely Py(50)/Nb(60)/Py(20) (all thicknesses in nm), exhibits a clear resistance dependance upon orientation of the ferromagnets even though the Nb layer is thick, whereas all sensitivity to the ferromagnets disappears for our samples with $d_{Nb} \geq 28$ nm.

Consequently, the claim made by Rusanov *et al.* that an increased polarization of the ferromagnet directly leads to an increased quenching of superconductivity, with the AP state reflecting more spin-polarized quasiparticles, is not substantiated according to our experiments, since both Py and Ni have significant polarization [64] and we do not observe this behavior.

Sample	d_{Nb} [nm]	T_C [K]	ΔT_C [mK]	$\delta\ \Delta T_C$ [mK]
1656 - 1B	17	0.34	41.0	0.3
1656 - 4A	18	2.29	4.7	0.5
1656 - 3A	19	2.74	3.7	1.0
1656 - 4B	19	2.53	4.5	1.0
1656 - 2A	20	3.49	2.0	0.5
1656 - 6B	21	3.78	2.0	0.5
1634 - 8B	17.5	1.29	11.0	0.3
1628 - 1A	18	2.84	3.0	0.5
1628 - 1B	19	3.31	2.5	1.0
1622 - 5A	17	0.54	29.0	0.3
1622 - 1A	20	3.07	3.1	0.3
1622 - 4A	21	3.38	-	-
1622 - 1B	23	4.09	-	-
1619 - 3B	24	4.54	0.1	0.1
1619 - 1B	26	5.05	-	-
1619 - 2B	28	5.45	-	-
1619 - 5B	30	5.61	-	-
1619 - 4B	32	5.91	-	-
1619 - 1A	34	6.05	-	-
1619 - 6A	36	6.49	-	-
1619 - 5A	38	6.63	-	-
1619 - 3A	40	6.67	-	-
1619 - 2A	44	6.98	-	-
1619 - 6B	48	7.28	-	-
1619 - 4A	52	7.45	-	-

Table 4.1: Summary of Ni(7)Nb(d_{Nb})Ni(7)FeMn(8)Nb(2) sample data for different sputtering runs. The uncertainty in d_{Nb} is about 0.5 nm. The uncertainty in ΔT_C is obtained by inspection of each superconducting transition.

Sample	d_{Nb} [nm]	T_C [K]	ΔT_C [mK]	$\delta\ \Delta T_C$ [mK]
1692 - 6B	20.5	0.385	19.4	0.3
1692 - 3A	21.0	1.115	7.0	0.7
1692 - 2B	21.5	1.300	8.5	2.0
1692 - 6A	21.5	1.425	8.9	0.5
1687 - 3B	22.0	0.725	10.5	1.0
1680 - 6B	22.0	1.64	4.5	0.5
1680 - 4B	23.0	1.96	2.7	1.0
1680 - 6A	24.0	2.79	2.0	0.5
1680 - 5B	26.0	3.64	0.9	0.3
1680 - 1A	28.0	4.09	-	-
1680 - 2A	30.0	4.53	-	-
1680 - 3A	35.0	5.23	-	-
1680 - 4A	40.0	5.89	-	-
1680 - 5A	45.0	6.39	-	-
1680 - 7A	50.0	6.63	-	-
1680 - 8A	75.0	7.51	-	-
1680 - 7B	100.0	7.94	-	-
1680 - 8B	150.0	8.23	-	-

Table 4.2: Summary of Py(8)Nb(d_{Nb})Py(8)FeMn(8)Nb(2) data for different runs.The uncertainty in d_{Nb} is about 0.5 nm. The uncertainty in ΔT_C is obtained by inspection of each superconducting transition.

Chapter 5

Theoretical Fits to FSF data

There are several theoretical approaches that predict the superconducting transition temperature for a F/S/F trilayer structure. We have performed initial fitting procedures to our Ni/Nb/Ni trilayer systems following the treatment of Tagirov [32, 54], modified for the clean limit. We have also utilized the dirty-limit theoretical approach of Fominov *et al.* [33] and applied it to both the Ni/Nb/Ni as well as the Py/Nb/Py data. The first section of this chapter contains an extensive parameter study, which is subsequently followed by fitting procedures and results for both Tagirov and Fominov theories.

5.1 Characterization Of Materials

Both the Tagirov and Fominov theoretical models contain several parameters that characterize the F/S material system, such as thin film resistivities, the T_C of bare Nb films, diffusion constants, coherence lengths and F/S boundary resistance. Before performing fits to the T_C vs. d_{Nb} and ΔT_C vs. T_C data obtained from our Ni and Py trilayer structures, establishment of best estimates of parameters is necessary as this reduces the number of free parameters, thus resulting in more realistic fits. Several supplemental experiments were carried out in order to obtain accurate values for the

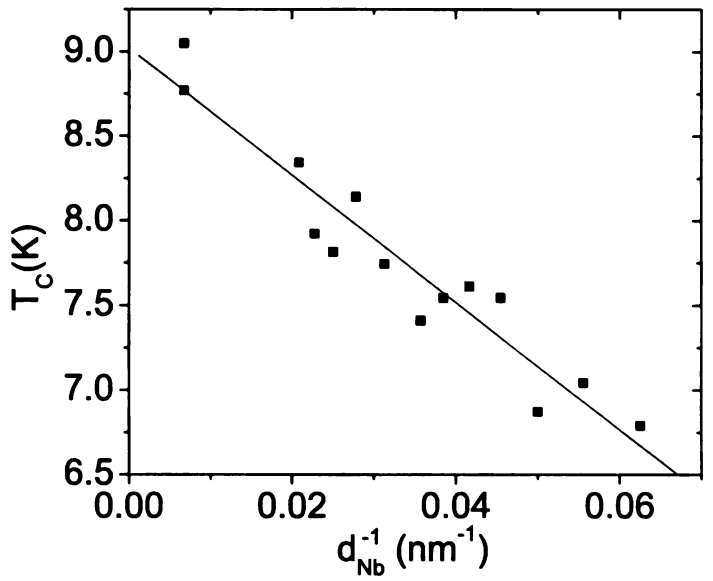

Figure 5.1: T_C vs. d_{Nb}^{-1} for isolated Nb films. The linear fit is T_C[K] = 9.09 − 42.82/d_{Nb}[nm]. If two nm are removed from the Nb thickness to account for oxidation, then the fit intercept becomes 9.02 K and the slope is 37.59 K·nm.

material parameters. These experiments and the resulting estimates are outlined in the next few sections.

5.1.1 T_C of bare Nb Thin Films

The critical temperature of the bare Nb enters both theories as a normalization to the T_C for the F/S/F trilayers. The T_C's for the bare films are thickness-dependent and subsequently had to be measured independently for a series of samples with thicknesses in the same range as our trilayers.

The results are illustrated in Fig. 5.1, with all samples shown being deposited in the same run. The data are plotted as a function of the inverse thickness of Nb and can be matched with a linear fit T_C[K] = 9.09 − 42.82/d_{Nb}[nm], where d_{Nb} is the nominal thickness of the bare Nb films. The samples with the smallest T_C correspond to a Nb thickness close to 20 nm. Since oxidation occurs and is limited to the top 2 nm, removing this thickness from the nominal values of all data points results in

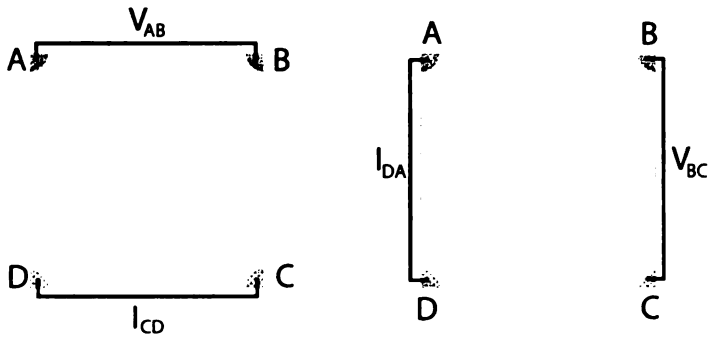

Figure 5.2: Van der Pauw resistance method to obtain resistivity for a sample of arbitrary shape.

an adjusted fit, $T_C = 9.02 - 37.59/d_{Nb}$. This second form will be utilized for all the theoretical fits, yet the correction hardly changes the fits. The scatter in the data illustrate the sensitivity of T_C on growth conditions, with samples fabricated earlier in the run having slightly lower T_C as compared to those deposited later. This is due to the fact that sputtering the Nb for a longer time eliminates more of the surface impurities from the target, acquired during the loading process. Furthermore, Nb is a "getter" material and it helps improve the cleanliness of the system by trapping impurities as it is being deposited everywhere on the substrate plate. All T_C measurements were obtained by resistive measurements on 4-terminal samples.

5.1.2 Resistivity

The resistivity of the ferromagnetic and superconducting materials enter all theoretical treatments of F/S systems employed in fitting our data, and therefore had to be measured for our samples. Making resistance measurements on 4-terminal devices of known dimensions is a good way to obtain a resistivity value, where the current path is well defined. However, the Van der Pauw [65] technique is commonly used for electrical transport measurements of thin films of arbitrary shape, where the contacts can be placed anywhere on the periphery as long as they are sufficiently small and

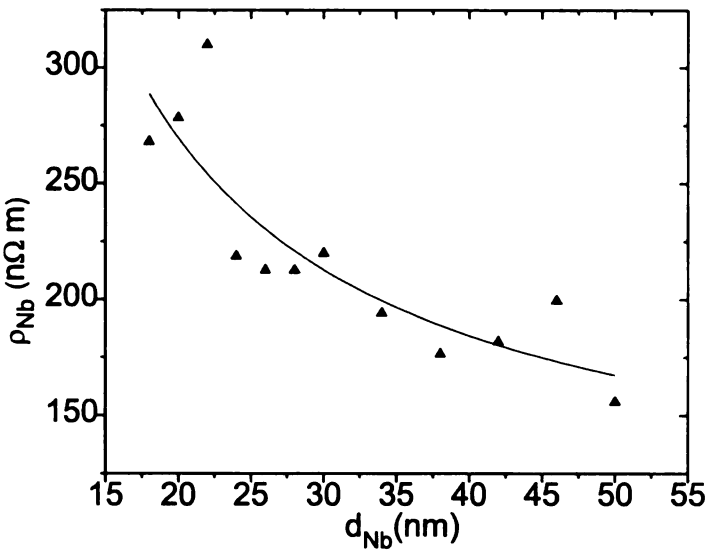

Figure 5.3: ρ_{Nb} vs. d_{Nb} for isolated Nb films obtained from 4-terminal resistance measurements at a temperature of 10 K. The trend of the data is captured by a Fuchs-Sondheimer fit: $\rho_{Nb}[\text{n}\Omega\ \text{m}] = 3414.6/d_{Nb}[\text{nm}] + 99.0$. A $d_{Nb} = 150$ nm sample with $\rho_{Nb} = 57.4$ nΩ m, measured by the Van der Pauw technique, has been excluded from the fit.

the sample is homogeneous in thickness.

The Van der Pauw resistivity for a sample of thickness d is given by

$$\rho = \frac{\pi \cdot d}{\ln 2}\left[\frac{R_{AB} + R_{BC}}{2}\right] \cdot f(R_{AB}/R_{BC}) \tag{5.1}$$

where R_{AB} and R_{BC} are the resistances measured as shown in Fig. 5.2 and $f(R_{AB}/R_{BC})$ is found by solving

$$\cosh\left[\frac{R_{AB}/R_{BC} - 1}{R_{AB}/R_{BC} + 1}\frac{ln\,2}{f}\right] = \frac{1}{2}\exp\left[\frac{ln\,2}{f}\right] \tag{5.2}$$

A rough estimate for the bulk resistivity of Nb at 10 K has been obtained by using the Van der Pauw method on a bare 150 nm thick sample with a T_C of 8.77 K, yielding $\rho_{Nb} = 57.4$ nΩ m, with $f \approx 0.95$. Similarly, the bulk resistivity of Ni at 4.2 K was obtained from a 200 nm thick sample, resulting in $\rho_{Ni} = 33.0$ nΩ m.

Since the layer thicknesses of our samples are much smaller than the bulk, we have

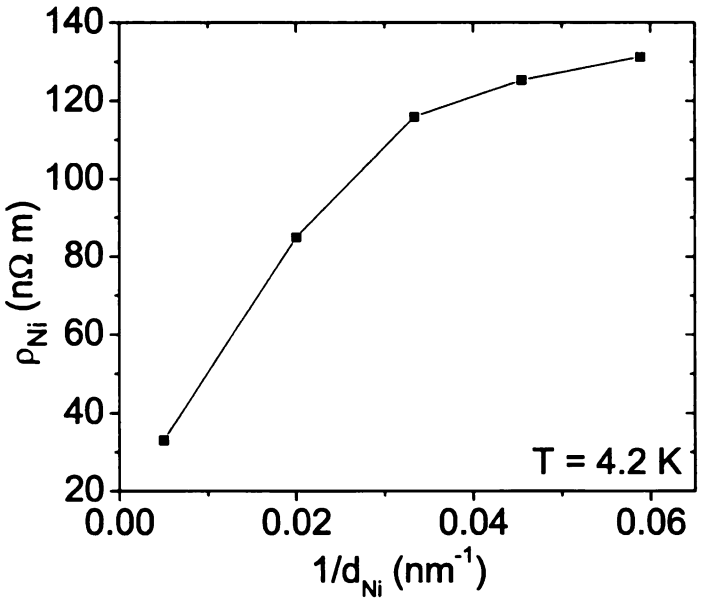

Figure 5.4: ρ_{Ni} vs. d_{Ni}^{-1} for five isolated Ni films of thickness d_{Ni} = 200, 50, 30, 22 and 17 nm. Measurements were taken at a temperature of 4.2 K on non-patterned (d_{Ni} = 200 nm) and 4-terminal samples with dimensions 3.5 x 1.8 mm^2.

investigated the dependence of resistivity on thickness in this range for both Nb and Ni. Fig. 5.3 shows a graph of ρ_{Nb} vs. d_{Nb} for patterned Nb films with thicknesses in the range of $18 - 50$ nm, with resistivities varying from about 150 to 300 nΩ m. The lateral dimensions of these 4-terminal samples are 1.6 x 4.3 mm^2. We have performed a Fuchs-Sondheimer [66, 67] fit to the Nb film data using

$$\rho = \rho_{bulk}\left[1 + \frac{3}{8}\frac{l_{Nb}}{d_{Nb}}\right] \tag{5.3}$$

where ρ_{bulk} is the bulk resistivity, l_{Nb} is the mean free path and d_{Nb} is the Nb thickness in this case. This model treats the additional contribution to the resistivity as arising from diffuse scattering of electrons at the film surfaces. The results of the fit give $\rho_{bulk} = 99.0 \pm 22.8$ nΩ m and $3/8\,\rho_{bulk}\,l_{Nb} = (3414.6 \pm 619.5)\cdot 10^{-9}$ nΩ m^2, which gives $l_{Nb} = 91.98 \pm 16.69$ nm with $\rho_{bulk} = 99.0$ nΩ m. This value of ρ_{bulk} is about twice what we have measured for our bulk film and the value of l_{Nb} that much longer than what

we obtained from an experimental estimate. An estimate for l_{Nb} was also obtained by using the value of $\rho_{Nb} l_{Nb} = 0.38$ fΩ m^2 from literature [11]. Using a value for $\rho_{Nb} = 57.4$ nΩ m measured on a thick Nb sample using the Van der Pauw technique, this resulted in $l_{Nb} = 6.6$ nm, which was used for the fits. Although the Fuchs-Sondheimer model does not yield good estimates for ρ_{bulk} and l_{Nb}, it nevertheless follows the data. Therefore, the fit will be used in subsequent theoretical treatments for the F/S/F trilayers only in the thickness range of the data.

The resistivity of Ni was also determined as a function of thickness at 4.2 K. Fig. 5.4 illustrates the resistivities of 4 samples with thicknesses $d_{Ni} = 50$, 30, 22 and 17 nm, obtained from 4-terminal devices, as well as the value of a bulk, 200 nm thick sample measured by the Van der Pauw method. The data are plotted as a function of the inverse thickness, and does not show a linear behavior of ρ_{Ni} vs. d_{Ni}^{-1}, indicating that a Fuchs-Sondheimer fit would not follow the data. In the limit of thin ferromagnet, the resistivity of Ni approaches $\rho_{Ni} \approx 130$ nΩ m. Since the thickness of the ferromagnet is always fixed for all our F/S/F trilayers, i.e. $d_{Ni} = 7$ nm, this value will be used in the theoretical fits.

5.1.3 Coherence Length from Critical Field Measurements

Ginzburg-Landau (GL) theory is a treatment of superconductivity which gives accurate predictions of critical fields and the spatial structure of the order parameter in non-uniform situations. The basic approach involves applying a variational method to an expansion of the free-energy density in even powers of the order parameter and its spatial gradient. The model requires that temperatures be close to T_C and that variations in the fields and order parameter are not too rapid (for a review see [39]). According to the theory, the in-plane coherence length, which is essentially the size of a Cooper pair, can be determined by the critical field applied perpendicularly to the sample.

Niobium is a type II superconductor and the application of an external field will not immediately drive it normal. Below a critical field, H_{C2}, the superconductor will maintain its superconducting state by allowing the penetration of flux through normal regions on a triangular lattice called vortices, each supporting a quantum of flux, Φ_0. As the field is increased to a value close to H_{C2}, the separation between the vortices decreases until superconductivity is totally suppressed. H_{C2} can therefore be estimated by essentially taking one flux quantum to penetrate an area the size of the coherence length, ξ_{GL}, as follows [68]:

$$H_{C2}(T) = \frac{\Phi_0}{2\pi\xi_{GL}(T)^2} \tag{5.4}$$

where the coherence length is temperature dependent,

$$\xi_{GL}(T) = \frac{\xi_{GL}(0)}{(1 - T/T_C)^{1/2}} \tag{5.5}$$

Substituting Eq. 5.5 into Eq. 5.4 and taking the derivative with respect to temperature, the zero temperature Ginzburg-Landau coherence length can be obtained,

$$\xi_{GL}(0) = \left(-\frac{dH_{C2}}{dT}\frac{2\pi T_C}{\Phi_0}\right)^{-1/2} \tag{5.6}$$

A comparison with the GL theory and using the relation $\xi_S = 2/\pi\xi_{GL}(0)$ from the work of Radović *et al.* [69], then the expression

$$\xi_S = \left(\frac{2}{\pi}\right)\left(-\frac{dH_{C2\perp}}{dT}\frac{2\pi T_C}{\Phi_0}\right)^{-1/2} \tag{5.7}$$

can be established for the dirty-limit coherence length for a superconducting thin film as a function of the perpendicularly applied magnetic behavior and the zero field T_C.

Figure 5.5 illustrates several R vs. T curves obtained by applying different values for the perpendicular magnetic field to a bare Nb sample, with d_{Nb} = 50 nm, and

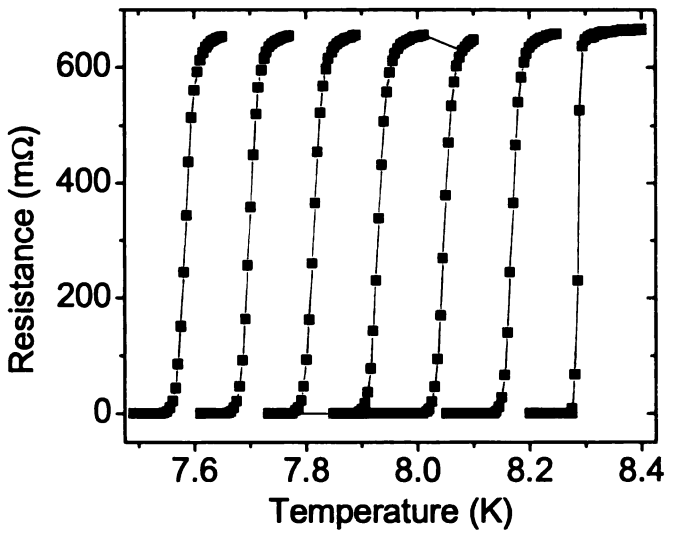

Figure 5.5: R vs. T for an isolated $d_{Nb} = 50$ nm film with field applied perpendicular to the sample. The rightmost transition is taken in zero applied field while the leftmost one is taken with $H_{\perp} = 3000$ Oe.

sweeping the temperature through the superconducting transition. Starting from right-most curve, the T_C for this sample is about 8.29 K when no field is present and 7.59 K when 3000 Oe are applied (the left-most curve).

Subjecting the sample to an applied field reduces the T_C linearly, as illustrated by the even spacings between the transitions, each separated in field by 500 Oe. Plotting the different transitions as a function of the perpendicular field a linear curve of $H_{C2\perp}$ vs. T_C can be obtained, as shown in Fig. 5.6 (c). Performing a least-squares fit to obtain the slope, a coherence length can be calculated according to Eqn 5.7, yielding $\xi_S(d_{Nb} = 50) = 6.1$ nm.

Similarly, Fig. 5.6 (a), (b), (d) illustrate data obtained from samples with $d_{Nb} =$ 20, 38, and 150 nm, which give $\xi_S = 5.8$, 6.3 and 7.9 nm. These values of ξ_S are summarized graphically in Fig. 5.8 and compared with those obtained from resistivity measurements.

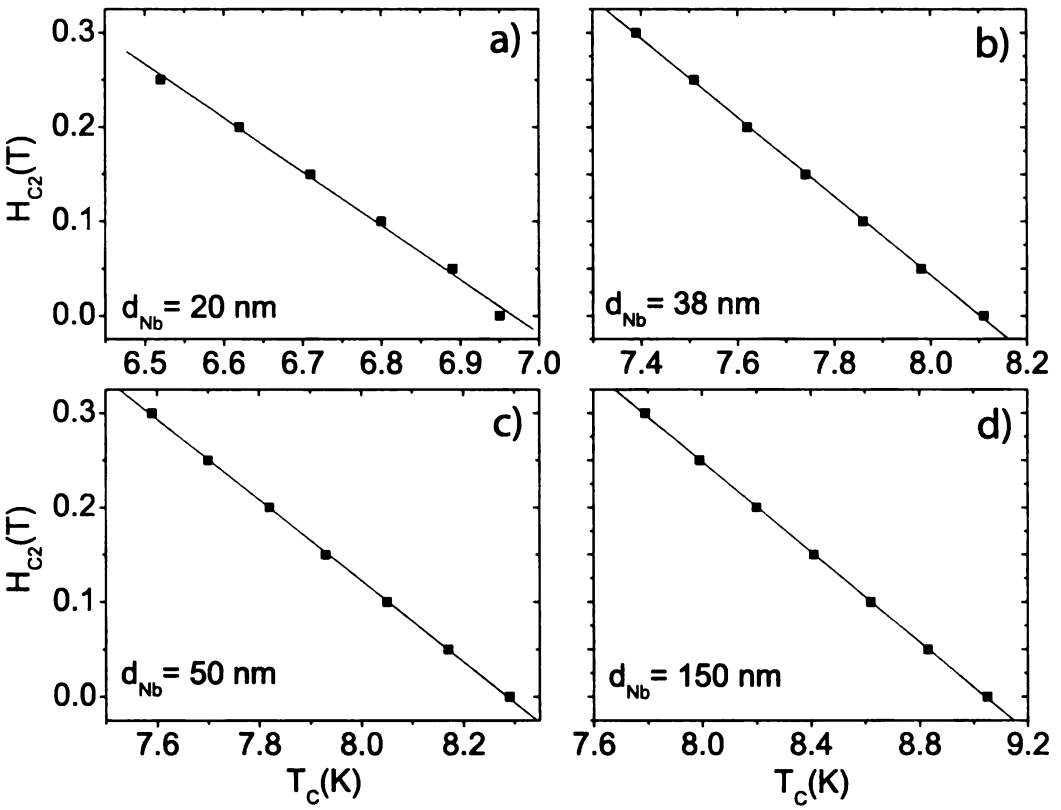

Figure 5.6: H_{C2} vs. T_C for Nb films with field applied perpendicularly to the plane. The slopes from the linear fits, $H_{C2} = m \cdot T_C + b$, are 0.57123, 0.419, 0.42804, and 0.23807 Oe/K for d_{Nb} = 20, 38, 50 and 150 nm, respectively.

5.1.4 Coherence Length from Resistivity

Another method to obtain an estimate of ξ_S as a function of the Nb thickness is to use the BCS dirty limit coherence length formula from directly, namely

$$\xi_S = \left(\frac{\hbar D_S}{2\pi k_B T_C}\right)^{1/2} = \sqrt{\pi/6\gamma}\sqrt{l_S \xi_{BCS}} \tag{5.8}$$

where diffusion constant, D_S, is given in terms of the Fermi velocity, v_F and the mean free path, l_S, according to $D_S = \frac{1}{3} v_F l_S$. The Euler constant, γ, has a value of 1.7811.

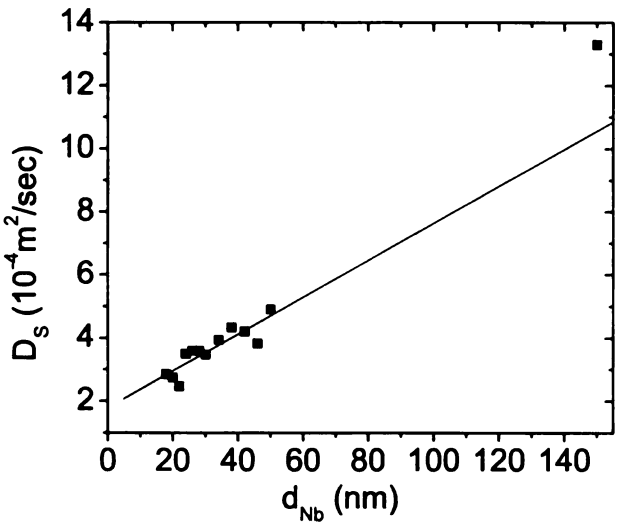

Figure 5.7: D_S vs. d_{Nb} for isolated Nb films obtained from resistivity measurements via the Einstein relation. The linear fit is $D_S\,[\mathrm{m}^2/\mathrm{s}] = 1.78 \cdot 10^{-4} + 5.86 \cdot 10^{-6} d_S$ [nm], limited to the range of the data (the $d_{Nb} = 150$ nm sample has been excluded from the fit due to its low resistivity compared with the thinner samples).

The clean-limit BCS coherence length is given by

$$\xi_{BCS} = \frac{\hbar v_F \gamma}{\pi^2 k_B T_C} \tag{5.9}$$

The dependance of T_C on the Nb thickness can be obtained from data shown in Fig. 5.1, while the dependance of D_S on the thickness is obtained from the normal resistivity via the Einstein relation

$$\sigma = N(E_F)\, e^2\, D_S \tag{5.10}$$

where σ is the conductivity and the density of states at the Fermi energy is taken to be $N(E_F) = 3.1$ eV^{-1} cm^{-3} [70]. The resulting fit of the diffusion constant as a function of thickness is $D_S\,[\mathrm{m}^2/\mathrm{s}] = 1.78 \cdot 10^{-4} + 5.86 \cdot 10^{-6} d_S$ [nm], being valid only in the thickness range of the data, $18 < d_{Nb} < 50$ nm. Using the resistivity data to obtain D_S along with the corresponding T_C, the ξ_S vs. d_{Nb} data in Fig. 5.8 is

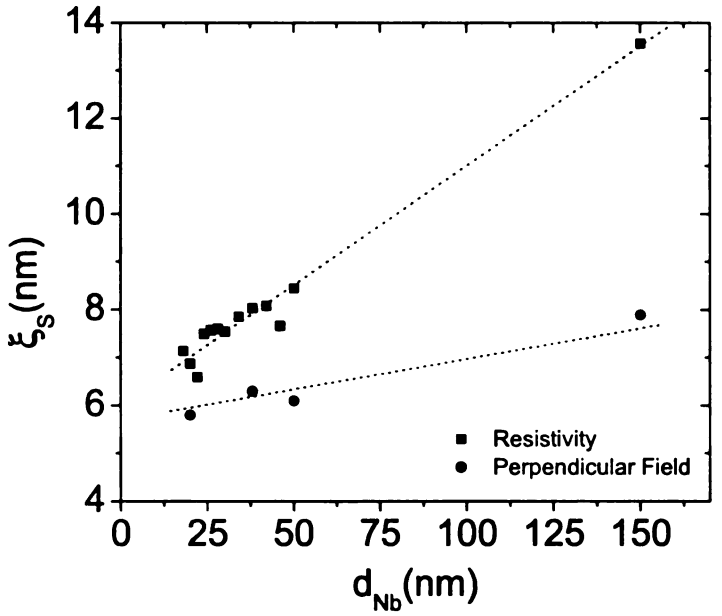

Figure 5.8: ξ_S vs. d_{Nb} for isolated Nb films obtained from resistivity and perpendicular field measurements (the dotted lines are guides for the eye).

obtained. Since ξ_S depends on the ratio of D_S to T_C, which are both dependent on thickness, then the very slight dependence of ξ_S on thickness is reasonable, namely $6.6 < \xi_S < 8.4$ nm over the thickness range $18 < d_{Nb} < 50$ nm.

Taking into consideration both the perpendicular field and resistivity data, the value of ξ_S falls in between 6 and 8 nm over the thickness range of these experiments. Therefore, a fixed value of $6 - 8$ nm was used in our fits to the FSF trilayer data.

5.1.5 Ni/Nb interface

We have carried out measurements on multilayer samples in order to obtain estimates for the interface transparency between the Ni and Nb, which were then compared with values obtained from applying the Fominov fitting method to our Ni/Nb/Ni trilayer data. By depositing a series of CPP-type samples containing Cu(10)[**Ni(8)Nb(4)**]$_N$Ni(8)Cu(10) layers between Nb(150) leads and varying the number of Ni/Nb bilayers (N), we have extracted the contribution of the interface

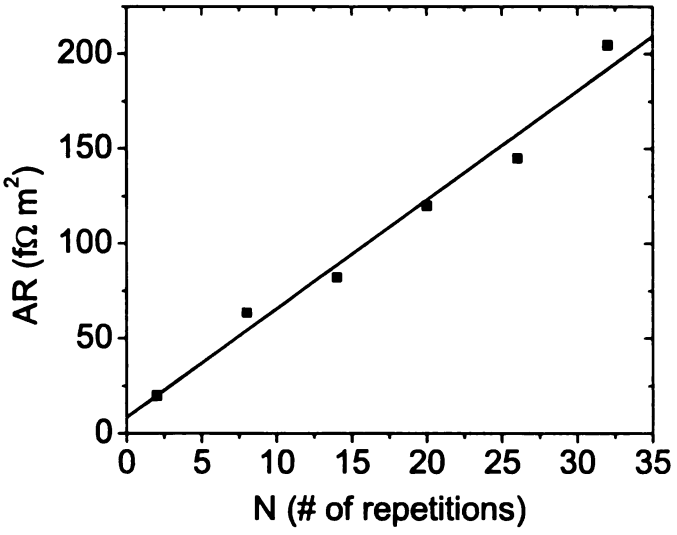

Figure 5.9: AR vs. N for Nb(150)/Cu(10)[Ni(8)Nb(4)]$_N$Ni(8)Cu(10)/Nb(150) samples, where A is the area and R is the resistance. By repeating the expression in the brackets [] a number of times (N), we add interfaces that contribute to the quantity AR. The resulting linear fit is: $AR(N)$ [fΩ m^2] =$(8.44 \pm 8.57) + (5.74 \pm 0.43) \cdot N$.

resistance from the AR vs. N plot, shown in Fig. 5.9, where AR is the product of the total resistance and the area of the sample. The bulk and interface components contributing to AR are as follows:

$$AR = 2AR^*_{Ni/Cu} + \rho_{Ni}t_{Ni}(N+1) + \rho_{Nb}t_{Nb}N + 2AR^*_{Ni/Nb}N \qquad (5.11)$$

where ρ_{Ni} and ρ_{Nb} are the Ni and Nb resistivities and the corresponding layer thicknesses are $t_{Ni} = 8$ nm and $t_{Nb} = 4$ nm. The Ni/Nb and Ni/Cu boundary resistances are $R^*_{Ni/Nb}$ and $R^*_{Ni/Cu}$. The contribution of the Cu layers to AR has been neglected since, in contact with thick Nb, they are superconducting. From all terms proportional to N in Eqn. 5.11, $2AR^*_{Ni/Nb}$ is dominant by an order of magnitude. Therefore, using the linear fit to the data, $AR(N)$ [fΩ m^2] =$(8.44 \pm 8.57) + (5.74 \pm 0.43) \cdot N$ and subtracting the contributions of $\rho_{Ni}t_{Ni}$ and $\rho_{Nb}t_{Nb}$ to the slope (totalling about 0.5 fΩ m^2), we obtain an estimate for the product of the Ni/Nb boundary resistance and the area, $AR^*_{Ni/Nb} = 2.62 \pm 0.22$ fΩ m^2.

Niobium	Value	Source
ρ_S [nΩ m]	57.4 $99 + 3415/d_S$ [nm]	Van der Pauw bulk at 10 K thin films $18 < d_S < 50$ nm
v_F [m/s]	$0.51 \cdot 10^6$	band structure [71]
$N_S(\epsilon_F)$ [eV^{-1}atom^{-1}]	1.5	band structure [70]
D_S [cm^2/s]	13.3 $1.783 + 0.059\, d_S$ [nm]	$D_S = 1/\rho_S N(\epsilon_F) e^2$ thin films $18 < d_S < 50$ nm
T_C [K]	$9.0 - 37.7\, d_S$ [nm]	thin films $18 < d_S < 50$ nm
l_S [nm]	7.8	$l_S = 3D_S/v_F$
$\rho_S\, l_S$ [fΩ m^2]	0.38	[72]
ξ_S [nm]	$6 - 8$	$H_{c2\perp}$ and ρ_S on thin films
ξ_{BCS} [nm]	42	[73]

Table 5.1: Niobium Parameter Summary

Nickel	Value	Source
ρ_F [nΩ m]	33.0 $80 - 130$	Van der Pauw bulk at 4.2 K thin films $22 < d_F < 50$
E_{ex} [eV]	0.115	photoemission experiments [74]
v_F [m/s]	$0.28 \cdot 10^6$	majority spin band [74]
$N_F(\epsilon_F)$ [eV^{-1}atom^{-1}]	3.1	band structure [75]
D_F [cm^2/s]	6.7	$D_F = 1/\rho_F N(\epsilon_F) e^2$
l_F [nm]	7.2	$l_F = 3D_F/v_F$
$\rho_F\, l_F$ [fΩ m^2]	$0.7 - 2.3$	[76]
ξ_F [nm]	0.8	$\hbar v_F/E_{ex}$
ξ_F [nm]	2	$\sqrt{\hbar D_F/E_{ex}}$
l_{sf} [nm]	≈ 21	from multilayers [77]

Table 5.2: Nickel Parameter Summary

Permalloy	Value	Source
ρ_F [nΩ m]	123 ± 40	bulk at 4.2 K
E_{ex} [eV]	0.135	photoemission experiments [74]
v_F [m/s]	$0.22 \cdot 10^6$	majority spin band [74]
l_F [nm]	0.5	minority spin band [74]
ξ_F [nm]	0.5	$\hbar v_F/E_{ex}$
l_{sf} [nm]	≈ 5	from multilayers [63]
β	0.73 ± 0.07	from multilayers [63]

Table 5.3: Permalloy Parameter Summary

5.2 Tagirov Theory Fits

The critical temperature of a F/S/F/AF structure in the P and AP states has been theoretically calculated by Tagirov [54]. Since many experiments employ ferromagnetic alloys with short mean free paths, the approach involves solving the Usadel equations in the dirty limit for both the superconductor and the ferromagnet, as shown in Chapter 2. The dirty limit applies to S when $l_S < \xi_{BCS} = \hbar v_S \gamma / \pi^2 k_B T_{C0}$, and to F when $l_F < \xi_F$, where l_S and l_F are the electron mean free paths in S and F. T_{C0} is the transition temperature of the bulk superconductor and $\gamma = 1.7811$.

In our case, however, the ferromagnetic Ni metal is both pure and strong, thus in the clean limit $l_F > \xi_F = \hbar v_F / E_{ex} \approx 1$ nm. Hence we use the theory of reference [54] modified according to section 3.2 of reference [32] in order to make it more appropriate for the clean limit. In the latter reference, Tagirov suggests changing the boundary condition (Eqn. 5.13 below) by replacing all factors of '3' with '1' for the case of magnetic stiffness length being shorter than the mean free path, i.e. the clean limit. However, this modification to the theory still does not incorporate a full description of the majority and minority spin bands of a strong ferromagnet, with different DOS, v_F, and transmission coefficients. Below, we present the formalism according to Tagirov, followed by the fits to our Ni/Nb/Ni data.

The critical temperature of the trilayer is obtained in the *single-mode* approximation [69], shown to be accurate for the case when the superconducting layer thickness is close to the coherence length, i.e. $d_S \geq \xi_S$. For temperatures close to T_C the self-consistency gap equation yields the expression that determines the reduced transition temperature, $t_c \equiv T_C / T_{C0}$,

$$\ln t_c + Re\left\{\Psi\left(\frac{1}{2} + \frac{2\phi^2}{t_c (d_S/\xi_S)^2}\right)\right\} - \Psi\left(\frac{1}{2}\right) = 0, \tag{5.12}$$

where T_{C0} is the critical temperature of an isolated Nb film of the same thickness

as the one in the trilayer. $\Psi(x)$ is the digamma function, $\xi_S^2 = \hbar D_S/2\pi k_B T_{C0}$ is the coherence length and $\phi = k_S\, d_S/2$, where k_S is the propagation momentum of the pairing function in the superconducting layer.

Using the appropriate boundary conditions at the F/S interface and the behavior of the correlation function at the edges of the F layers, the function which determines ϕ for the P state is then

$$\phi \tan\phi = R \equiv \frac{N_F D_F^+}{2N_S D_S} \left[k_F^+ d_S \tanh(k_F^+ d_F)\right] \left[1 + \frac{2D_F^+ k_F^+}{T_F v_F} \tanh(k_F^+ d_F)\right]^{-1} \tag{5.13}$$

where N_S and N_F are the densities of state of the superconductor and ferromagnet, respectively. The diffusion constant of the superconductor, D_S, is real, while that of the ferromagnet,

$$D_F^+ = \frac{1}{3} \frac{v_F l_F}{(1 + i\, l_F/\xi_F)} \Rightarrow \frac{v_F l_F}{(1 + i\, l_F/\xi_F)} \tag{5.14}$$

is complex. v_F is the Fermi velocity in the F layer. The last expression in this equation was obtained by invoking Tagirov's argument for the clean limit and dropping the factor of 3. T_F is a dimensionless transparency parameter of the F/S interface, while

$$k_F^+ = \sqrt{\frac{2iE_{ex}}{\hbar D_F^+}}, \tag{5.15}$$

where E_{ex} is the exchange energy of the ferromagnet. In the case of AP alignment, E_{ex} for the free ferromagnetic layer is negative (for the pinned layer E_{ex} is taken positive) and using the boundary conditions from above the equation determining ϕ is then given by

$$(\phi \tan\phi - R')(R' \tan\phi + \phi) - (R'')^2 \tan\phi = 0 \tag{5.16}$$

where R' and R'' are the real and imaginary parts of R from Eqn. 5.13, i.e. $R = R' + iR''$. In the limit of thick ferromagnet [32] $\tanh[k_F^+ d_F] \rightarrow 1$, and expressing R in

a more convenient form, we obtain

$$R = \frac{d_S}{\xi_S}\frac{N_F v_F \xi_S}{2N_S D_S}\frac{1}{\sqrt{1 - i\xi_F/l_F} + 2/T_F} \tag{5.17}$$

Setting the tanh functions to 1 is validated by data on Nb/Ni bilayers [57], which showed that oscillations in $T_C(d_F)$ are completely damped for $d_F > 4$ nm, and the fact that all our Ni thicknesses are 7 nm. Therefore, the dimensionless parameters that enter into this theory are the ratios d_S/ξ_S, ξ_F/l_F, the transparency T_F, and the combination $N_F v_F \xi_S / 2N_S D_S$.

The first step in applying the Tagirov theory is to obtain a fit to the T_C vs. d_{Nb} data. We will use the formulation for the P state, Eqn. 5.13, using the form of R in Eqn. 5.17, since the difference between the P and AP state is small (of order mK). To avoid fitting the data with four free parameters, we have followed the strategy outlined by Lazar *et al.* [10] and by Sidorenko *et al.* [57] in which parameter estimates were obtained from the T_C vs. d_{Nb} data, literature and values yielded by the additional experiments outlined in the previous sections.

To begin, we have utilized the superconducting coherence length, ξ_S, value obtained from measurements of the critical field vs. temperature of isolated Nb films, with the magnetic field applied perpendicular to the film plane. For films in the thickness range $20 - 50$ nm, the values of ξ_S are close to 6 nm, and we have used this number for our fits.

The next series of steps utilizes the behavior of the critical temperature close to the critical thickness, d_S^{cr}, in order to find an expression that limits the independent variation of T_F with respect to the other parameters. To find the asymptotic behavior of Eqn. 5.12 at d_S^{cr}, when t_c is essentially zero, we take

$$\ln x + Re\left\{\Psi\left(\frac{1}{2} + \frac{a}{x}\right)\right\} - \Psi\left(\frac{1}{2}\right) = 0, \tag{5.18}$$

with $x = t_c$ and $a = 2\phi^2/(d_S/\xi_S)^2$, and by expanding the digamma function for $x \ll 1$ we get

$$\ln x + Re\left\{-\ln x + \ln a + \frac{1}{24}\left(\frac{x}{a}\right)^2\right\} + C + 2\ln 2 = 0 \tag{5.19}$$

where $C = 0.577$ is the Euler constant, sometimes written as $\gamma \equiv e^C = 1.7811$. Thus,

$$\ln|a| + \frac{x^2}{24} Re\left\{\frac{1}{a^2}\right\} + C + 2\ln 2 = 0, \tag{5.20}$$

which in the limit of $x \to 0$ implies that

$$\ln|a| = -C - 2\ln 2. \tag{5.21}$$

Since $e^{2\ln 2} = 4$, the above expression becomes

$$\frac{2\phi_{cr}^2}{(d_S^{cr}/\xi_S)^2} = \frac{1}{4\gamma}. \tag{5.22}$$

which constrains the value of ϕ at the critical thickness. Substituting $d_S^{cr} \approx 16.5$ nm obtained from our T_C vs. d_{Nb} data and $\xi_S = 6$ nm in the above gives a value for ϕ^{cr}. Using Eqn. 5.13 with form of R from Eqn. 5.17 we then obtain the constraint

$$\frac{N_F v_F \xi_S}{2N_S D_S(d_S^{cr})} \frac{1}{1 + 2/T_F} \approx \frac{\phi^{cr}\tan\phi^{cr}}{(d_S^{cr}/\xi_S)} = 0.24. \tag{5.23}$$

The thickness dependent value of D_S is taken at the d_S^{cr} and ϕ^{cr} is given by Eq. 5.22. The last expression was obtained by assuming that the imaginary term is small, i.e. $\xi_F/l_F \ll 1$. The constraint gives the value of T_F in terms of the material parameters, $D_S(d_S^{cr}), \xi_S, N_{F,S}$ and v_F. The next step is to substitute realistic numbers for these in order to obtain T_F.

For ferromagnetic Ni, estimates of the product $N_F v_F$ vary substantially in the literature. From low-temperature specific heat measurements, reference [75] quotes

a value of $N_F = 1.77 \cdot 10^{48}$ J^{-1}m^{-3}, while angle-resolved photoemission experiments [74] give a majority spin band $v_F = 0.28 \cdot 10^6$ m/s. On the other hand, Fierz *et al.* [76] quote $\rho_F l_F = 0.7 - 2.3$ fΩ m^2 for Ni, which when combined with the Einstein relation $1/\rho_F l_F = N_F v_F e^2/3$ imply values $3 - 10$ times smaller for $N_F v_F$.

We have used both references to give a range for the value of $N_F v_F$. For the superconductor, we have taken $N_S = 5.31 \cdot 10^{47}$ J^{-1}m^{-3} [70] obtained from band structure calculations of bcc niobium. Using our measured $D_S(d_s^{cr}) = 2.8 \cdot 10^{-4}$ m^2/s in Eq. 5.23 and the range of estimates for $N_F v_F$ we have obtained an estimate of the transparency, $T_F = 0.05 - 0.6$. Some importance is placed on this parameter as it is an indicator of the quality of the Ni/Nb interface. A high T_F indicates a very good interface, which is required for the observation of the triplet state in subsequent experiments. However, some caution should be exercised when interpreting the absolute number as the above range of values was obtained from a constraint that uses estimates of parameters not directly measured for our sputtered materials.

In Eqn 5.17 we also require an estimate for ξ_F/l_F to solve Eqn. 5.12 for the P and AP case. The bulk resistivity of our sputtered Ni films at 4.2 K is $\rho_F = 33$ nΩ m, which leads to values of l_F between 7 and 70 nm, given the range in $\rho_F l_F$ quoted by Fierz *et al.*. Since the thickness of Ni layers used in our samples is small, l_F is probably limited by surface scattering, so we have used the lower estimate $l_F = 7$ nm, hence $\xi_F/l_F \approx 0.1$.

Putting all the estimates together we have obtained the fit for the T_C vs. d_{Nb} data, shown in Fig. 5.10. The resulting fit follows the data quite well and correctly predicts $d_S^{cr} \approx 16$ nm. However, varying T_F and ξ_F/l_F does not change the fit very much. For the fit shown, we used $\xi_F/l_F = 0.1$ and $T_F = 0.3$.

A more stringent test of the theory is the prediction of ΔT_C, which depends sensitively on both T_F and ξ_F/l_F. Thickness deviations from nominal values produce scatter in plots of T_C or ΔT_C vs. d_{Nb}, therefore 5.11 shows a plot of ΔT_C vs. T_C. If

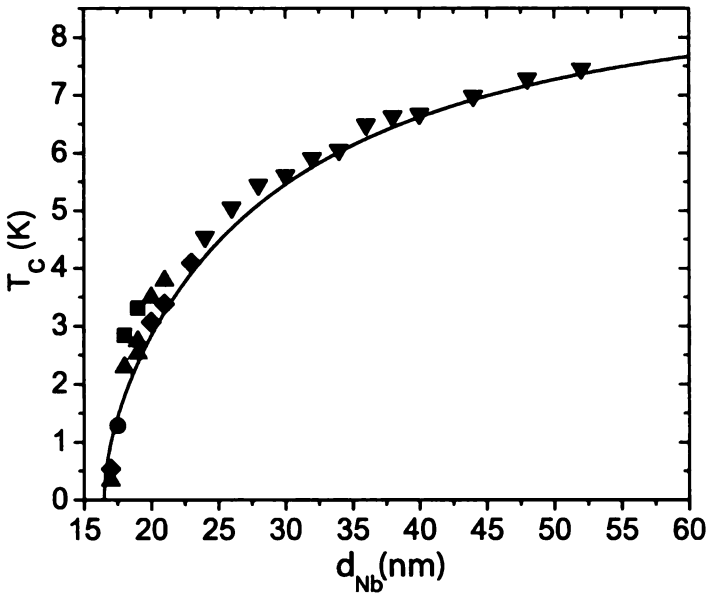

Figure 5.10: Fit to the T_C vs. d_{Nb} data for Ni/Nb/Ni with Tagirov theory using the parameters $\xi_F/l_F = 0.1$ and $T_F = 0.3$.

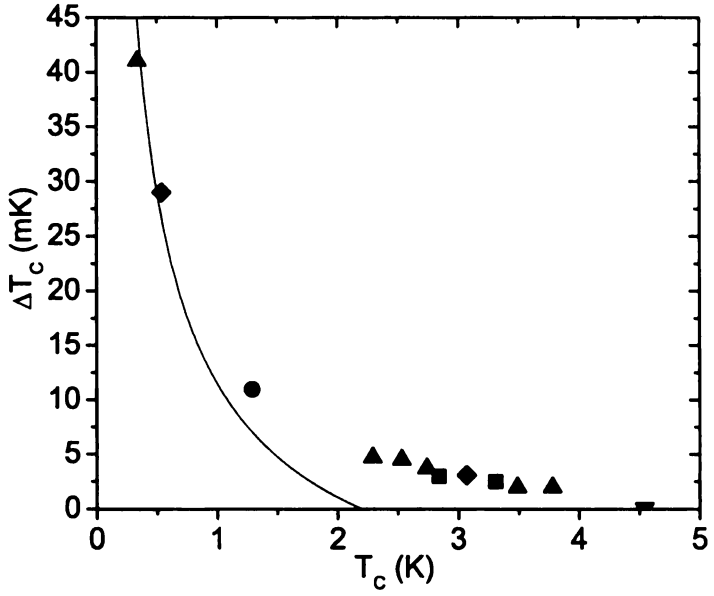

Figure 5.11: Fit to the ΔT_C vs. T_C curve for Ni/Nb/Ni using Tagirov theory using the parameters $\xi_F/l_F = 0.7$ and $T_F = 1.0$.

we calculate ΔT_C using our best estimate of $\xi_F/l_F \approx 0.1$ and the best transparency estimate, $T_F = 0.6$, the maximum value of ΔT_C is only a few mK when T_C is well below 1 mK – hardly visible at the scale shown in Fig. 5.11. If we relax the constraints we have placed on the parameters, and instead try to produce the best fit to the ΔT_C vs T_C data, we find that a moderate fit can be obtained when ξ_F/l_F is allowed to be much larger than our original estimate. Fig. 5.11 shows a fit using $\xi_F/l_F = 0.7$ and $T_F = 1.0$. Similar curves can be produced by simultaneously varying ξ_F/l_F and T_F while keeping their product nearly constant. Fitting the ΔT_C data requires letting ξ_F/l_F exceed our estimate substantially. Our l_F estimate may be too large, because the resistivity is dominated by the longer of the majority or minority band l_F, whereas the F/S proximity effect depends on the shorter of the two [10]. A shorter l_F is also implied by the observation of complete damping of T_C oscillations in Nb/Ni bilayers for $d_F > 4$ nm [57]. Nevertheless, producing a reasonable fit to our ΔT_c data entails either increasing ξ_F/l_F beyond the clean limit, or increasing T_F beyond our original estimate.

The fits using Tagirov theory should be taken with some caution as there is no distinction between the minority and majority spin bands, which cannot be ignored for strong ferromagnets. Furthermore, the prediction of ΔT_C vs. T_C gives positive values for $T_C < 2$ K but negative values for $T_C > 2$ K, a result that does not agree with our experiments.

5.3 Fominov Theory Fits

The theory of Fominov *et al.* also addresses the proximity effect of a F/S/F trilayer structure based on the mutual orientation of the ferromagnet magnetization, with the inclusion of a triplet superconducting component in the formulation. In that work, the dirty limit is considered, and near T_C the Usadel equations are linearized [33]. The following equations, which describe the critical temperature for the P and AP

cases, are obtained in the limits $d_S \ll \xi_S$, where Δ is constant, and also the strong ferromagnet limit.

$$\ln \frac{T_{C0}}{T_C^P} - Re\,\Psi\left(\frac{1}{2} + \frac{V_h}{2}\frac{\xi_S}{d_S}\frac{T_{C0}}{T_C^P}\right) + \Psi\left(\frac{1}{2}\right) = 0$$
$$\ln \frac{T_{C0}}{T_C^{AP}} - \Psi\left(\frac{1}{2} + \frac{W}{2}\frac{\xi_S}{d_S}\frac{T_{C0}}{T_C^{AP}}\right) + \Psi\left(\frac{1}{2}\right) = 0 \tag{5.24}$$

where T_{C0} is the critical temperature for the isolated superconducting layer of thickness d_S. In this formulation the dirty-limit coherence lengths of the superconductor and ferromagnet are given in terms of the critical temperature of the isolated S layer and the corresponding diffusion constant, $D_{S,F}$, as follows

$$\xi_{S,F} = \sqrt{\frac{\hbar D_{S,F}}{2\pi k_B T_{C0}}} \tag{5.25}$$

Fominov *et al.* make the important point that the existence of a pronounced angular dependence of relative magnetizations for $d_S > \xi_S$ is due to the fact that the critical temperature of the trilayer is suppressed as compared to that of the bare Nb layer, namely $T_C \ll T_{C0}$. Consequently, the condition $d_S \ll \xi_S = \sqrt{\hbar D_S/2\pi k_B T_{C0}}$ is sufficient for a thin S layer, whereas the necessary condition $d_S \ll \xi = \sqrt{\hbar D_S/2\pi k_B T_C}$ is weaker for a trilayer as $\xi \gg \xi_S$. By solving the boundary conditions, then in Eqn. 5.24

$$V_h = \frac{\gamma\,(1+i)\,k_h\xi_F\,\tanh\left[(1+i)k_h d_F\right]}{1 + \gamma_B\,(1+i)\,k_h\xi_F\,\tanh\left[(1+i)k_h d_F\right]} \tag{5.26}$$

$$W = ReV_h + (ImV_h)^2(d_S/\xi_F), \tag{5.27}$$

where, in terms of the resistivities and coherence lengths,

$$\gamma = \frac{\rho_S\xi_S}{\rho_F\xi_F} \qquad \gamma_B = \frac{R_B A}{\rho_F\xi_F}, \tag{5.28}$$

Here, $R_B A$ is the boundary resistance multiplied by the area, a parameter whose value is indicative of the quality of the interface, and γ is a measure of the strength of the proximity effect between the F and S metals. Also,

$$k_h = \sqrt{\frac{E_{ex}}{\hbar D_F}}, \tag{5.29}$$

is a dirty-limit inverse coherence length, giving the length scale of decay for the superconducting correlations, set by the exchange energy E_{ex} and the diffusion constant D_F. In the same manner as the Tagirov theory, taking the limit of $T_C \rightarrow 0$, for the behavior at the critical thickness, results in the constraints

$$d_{SC}^{P}/\xi_S = 2e^C|V_h| \qquad d_{SC}^{AP}/\xi_S = 2e^C W \tag{5.30}$$

where $C \approx 0.577$ is the Euler constant. In the limit of thick ferromagnet, i.e. $k_h d_F \gg 1$, the tanh functions are set to 1 and Eqns. 5.26 and 5.27 can be written in the form

$$V_h = \frac{\rho_S \xi_S}{(1-i)\rho_F/2k_h + R_B A} \qquad W = ReV_h \tag{5.31}$$

These are the functions that will be inserted in the Eqn. 5.24 to produce the fits. Using this result and Eqn. 5.30 for the P case, one can obtain an estimate of the boundary parameter as follows

$$R_B A = \sqrt{\left(2e^C \rho_S \xi_S \frac{\xi_S}{d_S^{cr}}\right)^2 - \left(\frac{\rho_F}{2k_h}\right)^2} - \frac{\rho_F}{2k_h} \approx 2e^C \rho_S \frac{\xi_S^2}{d_S^{cr}} \tag{5.32}$$

The last approximation was made because the first term under the square root dominates, namely

$$4e^C \frac{\rho_S}{\rho_F} \frac{\xi_S^2 k_h}{d_S^{cr}} \gg 1 \tag{5.33}$$

since, for example, for Ni and Nb system $\rho_S/\rho_F \approx 0.5$, $k_h \approx 1$ and $\xi_S^2/d_S^{cr} \approx 2$.

From our resistivity measurements, we have shown that ρ_S varies with thickness. Therefore the above R_BA value must be obtained for $\rho_S(d_S^{cr})$. Also, the explicit thickness dependence of ρ_S and T_{C0} will be inserted in Eqns. 5.31 and 5.24, namely $\rho_S[\text{n}\Omega\ \text{m}] = 99+3415/d_S$ [nm] and $T_{C0}[\text{K}]= 9.1-43/d_S$ [nm]. After constraining R_BA as shown above and using our values for measured resistivities and ξ_S, k_h remains as the only fit parameter.

5.3.1 Ni/Nb/Ni

The results for the fit of T_C vs. d_{Nb} for the Ni/Nb/Ni system are shown in Fig. 5.12 (a). Using $d_S^{cr} \approx 16.5$ nm and $\xi_S = 6$ nm in Eqn. 5.32 we obtain $R_BA = 2.3$ fΩ m^2, which is utilized to give a remarkably good fit. Similar to the method used when applying the Tagirov theory, the P state expression of Eqn. 5.24 was used to obtain the fit for T_C vs. d_{Nb}. Increasing the estimate for R_BA shifts the fit curves to the left, yielding higher T_C's for the same superconductor thickness, as a more resistive interface results in a lower influence of the ferromagnet on the superconducting layer. An advantage of this formalism, as compared with that of Tagirov, is that the fitting procedure gives a value for the interface transparency in terms of a quantity, R_BA, which can be measured independently from multilayer experiments. The results of those experiments yielded $AR^*_{Ni/Nb} = 2.62 \pm 0.22$ fΩ m^2 (section 5.1.5), a value that is close to what we obtain using the Fominov approach.

Once again, the better indicator for the quality of the theoretical prediction is reflected in the fit to the ΔT_C vs. T_C data. The result is shown in Fig. 5.12 (b), where a value of $k_h = 0.5$ nm^{-1} was necessary to obtain the fit. The result is extremely good, much improved when compared to that yielded by the Tagirov method, as the fit follows the data with the high as well as the low T_C. By utilizing Eqn. 5.29, our value for k_h obtained from the fit and the exchange energy for Ni, $E_{ex} = 0.115$ eV

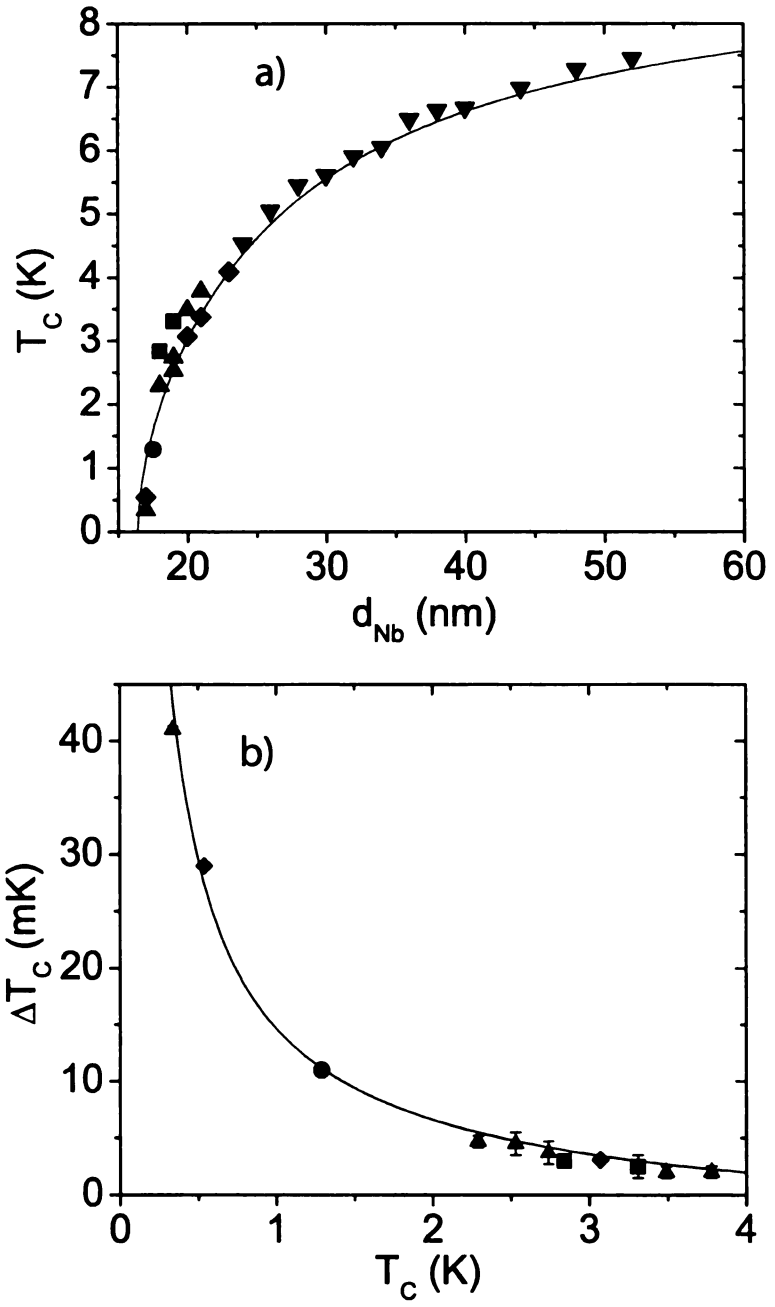

Figure 5.12: a) Fit to the T_C vs. d_{Nb} curve for Ni/Nb/Ni. The critical thickness is $d_{Nb}^{cr} \approx 16.5$ nm and it establishes $R_B A = 2.3$ fΩ m^2. Uncertainties in T_C are smaller than the symbol size. b) Fit to the ΔT_C vs. T_C curve. Estimates for the fit parameters are established experimentally, i.e. ρ_{Nb}, ξ_{Nb}, ρ_{Ni}. The value of $k_h = 0.5$ nm^{-1} is obtained from the fit.

given by Petrovykh *et al.* [74],

$$k_h = \sqrt{\frac{3}{v_F l_F}\frac{E_{ex}}{\hbar}} \tag{5.34}$$

we obtain $v_F l_F = 2.10 \cdot 10^{15}$ nm^2/sec. From literature, $v_F = 0.28 \cdot 10^{15}$ nm/sec [74] for the majority spin band and using $l_F = 7$ nm from our resistivity measurements we obtain $v_F l_F = 1.96 \cdot 10^{15}$ nm^2/sec, which is in very good agreement with the above value. The ΔT_C fit is quite sensitive to the values of $R_B A$ and k_h. Furthermore, according to Aarts *et al.* [9] the interface transparency T can be roughly related to γ_b as

$$T = \frac{1}{1+\gamma_b} \tag{5.35}$$

Entering $\rho_F = 130$ nΩ m, $\xi_F = 0.8$ nm, and $R_B A = 2300\,\Omega$ nm^2, we obtain $T = 0.04$, which is an order of magnitude smaller than the value obtained using the Tagirov theory.

5.3.2 Py/Nb/Py

Since the Fominov theory is explicitly in the dirty limit, we have also utilized it to fit our Py/Nb/Py data. After a similar procedure, the results for the fit of T_C vs. d_{Nb} are shown in Fig. 5.13 (a). Using $d_S^{cr} \approx 21.5$ nm and $\xi_S = 6$ nm we can obtain an estimate for $R_B A = 1.5$ fΩ m^2. Utilizing this value in the fits gives the correct thickness dependence as well as d_S^{cr}. Performing the fit for ΔT_C vs. T_C, shown in Fig. 5.13 (b), we obtain a value for $k_h = 1.0$ nm^{-1} with good agreement to the data. By utilizing Eqn. 5.29, our value for k_h obtained from the fit, and the exchange energy for Py, $E_{ex} = 0.135$ eV [74], we obtain $v_F l_F = 0.62 \cdot 10^{15}$ nm^2/sec. From Petrovykh *et al.* [74], the majority spin band Fermi velocity is $v_F^{\uparrow} = 0.28 \cdot 10^{15}$ nm/sec, while the minority mean free path is $l_F^{\downarrow} = 0.4 - 0.8$ nm. Since $l_F^{\uparrow}/l_F^{\downarrow} = (1+\beta)/(1-\beta) = 6.41$, where for Permalloy $\beta = 0.73 \pm 0.07$ [63], then the majority mean free path $l_F^{\uparrow} = 2.6 - 5.1$

nm. We can therefore obtain the estimate $v_F^{\uparrow} l_F^{\uparrow} = 1.08 \pm 0.35 \cdot 10^{15}$ nm^2/sec, which moderately agrees with the value using our fits.

In summary, the results of the fits according to Fominov *et al.* are impressive as they predict the correct behavior of T_C vs. d_{Nb} and ΔT_C vs. T_C for both the Ni/Nb and the Py/Nb trilayer systems, despite the fact that the theory does not distinguish between the minority and majority spin bands, which should be non-negligible for strong ferromagnets. Furthermore, the limit $d_S \ll \xi_S$, in which Eqns. 5.24 are obtained, is clearly violated if $\xi_S = 6$ nm as all the samples have Nb thicknesses at least greater than 16 nm. However, it is worth mentioning that our estimate for the coherence length is a result of in-plane resistive measurements, whereas the proximity behavior is an effect perpendicular to the plane. Due to the fact that there is a tendency for columnar growth of Nb, the in-plane mean free path can be much shorter than the out of plane one. Consequently, the error in our approximation of ξ_S may be significant as a longer perpendicular mean free path implies a larger ξ_S according to $\xi_S \propto \sqrt{l_S}$ [72].

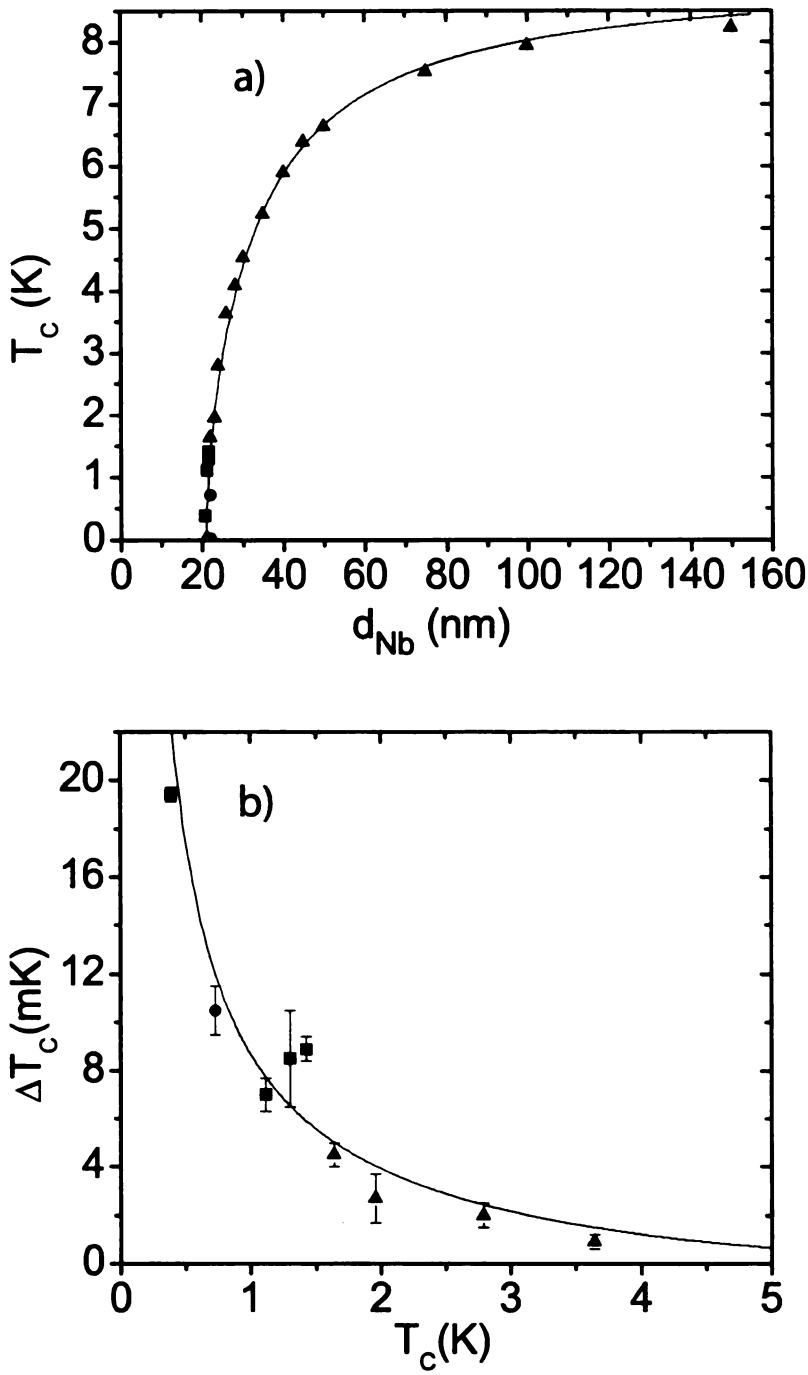

Figure 5.13: a) Fit to the T_C vs. d_{Nb} curve for Py/Nb/Py. The critical thickness is $d_{Nb}^{cr} \approx 21.5$ nm and it establishes $R_B A = 1.5$ fΩ m^2. Uncertainties in T_C are smaller than the symbol size. b) Fit to the ΔT_C vs. T_C curve. Estimates for the fit parameters are established experimentally, i.e. ρ_{Nb}, ξ_{Nb}, ρ_{Py}. The value of $k_h = 1.0$ nm^{-1} is obtained from the fit.

Chapter 6

Long range proximity effect

Given the effect of the exchange field on the Cooper pairs traversing the F/S interface, it is expected from proximity effect theory that the penetration of correlations inside the ferromagnet would be limited to the coherence length, ξ_F. For strong ferromagnets like Co and Ni, this length is limited to a few nm, at best. However, a series of surprising experiments showed that the extent of proximity effects inside a ferromagnet can be much larger than ξ_F.

In 1998 Giroud *et al.* [25] measured the temperature-dependent resistance of Co rings in contact with a superconducting Al film and found a temperature and bias-dependent differential resistance similar to the re-entrant proximity effect observed in N/S structures. The authors reported a penetration of superconducting correlations into the Co up to a distance of 180 nm. Also, Lawrence and Giordano [27] measured Ni wires in contact with Sn pads, and observed a large change in resistance below the superconducting transition which they attributed to a proximity effect that penetrated up to 46 nm into the Ni. In addition, Petrashov *et al.* [26] measured Ni wires in contact with Al films, and observed an anomalously large change in the resistance of the devices below the transition temperature of the superconductor. In that experiment it was concluded that the proximity effect penetrated up to a distance of 600 nm into the ferromagnet. However, in work done by Aumentado *et al.* [78] it

was reported that electrical transport of submicron-size Ni in contact with Al pads yielded no appreciable proximity effect. Given their multi-probe geometry the authors were able to isolate the contribution to the resistance change as stemming from the F/S interface, as opposed to the long-range penetration of correlations. They also reported that the interface resistance of their devices were sensitive to the magnetic state of their ferromagnet. Moreover, in theoretical work by Belzig *et al.* [79], the result of spin accumulation and Andreev reflection, rather than long-range proximity effect, is argued to lead to the anomalous resistance behavior.

In response to these works, we have noticed that there are two areas in which we could improve upon previous experiments in order to address the pending questions related to the origin of the long range proximity effect in F/S systems. The first would be to create a cleaner interface by depositing both materials within the same vacuum pump-down. Since the S and F materials in the proposed geometry (described below) would be patterned in different shapes, this would necessitate a multiple angle deposition process. The second improvement would require obtaining a good handle on the magnetic structure of the ferromagnet. According to theoretical work by Bergeret *et al.* [29] and Kadigrobov *et al.* [28], inhomogeneous magnetization can induce long-range proximity effects. Therefore, we want to understand the role of domain walls close to the F/S interface and their influence on the long-range proximity effect, if any. However, developing a sample fabrication method which implements all of the above changes successfully have posed serious challenges thus far. In this chapter, attempts at investigating the role of domain walls in the reported long range proximity effects are presented. Preliminary progress as well as possible future directions are reported.

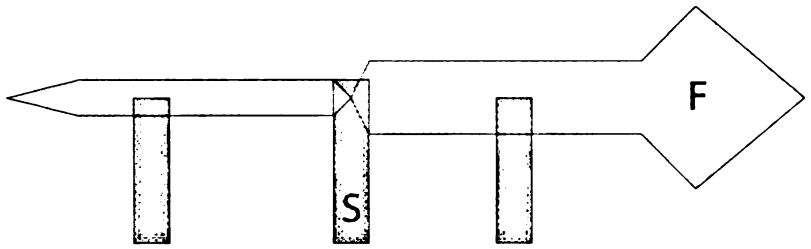

Figure 6.1: Proposed geometry for measuring the effect of a domain wall on the long range F/S proximity effect.

6.1 F/S Experiment

The unique challenges of this project range from choosing materials that give a good F/S interface and are compatible with our deposition requirements to obtaining the desired sample geometry using our nano-fabrication techniques. The proposed device for the detection of the long-range proximity effect is shown in Fig. 6.1. It includes a patterned ferromagnetic wire with a nano-constriction. In addition there are superconducting leads located on either side of the notch as well as directly on top of it. The F/S proximity effect resistance measurement is then performed between the lead making contact with the nano-constriction and either of the outer leads. An additional measurement across the constriction can be performed between the outer leads only, which can be useful in determining the magnetic state of the notch based on transport. Both types of resistance measurements mentioned are shown in Fig. 6.1 as being two-terminal for the sake of simplicity. An extension of the design to allow for four-terminal measurements poses little additional difficulty.

6.1.1 Geometry

The shapes and sizes of the features in the proposed sample geometry require the use of the e-beam lithography techniques described in Fig. 3.7 of chapter 3. Given that both the ferromagnetic and superconducting materials are to be deposited in the same vacuum pump-down, a directional deposition source is necessary for the

multiple angle evaporation. Thermal evaporation fulfills such a requirement and we have used it in combination with the lithography process. In order to accomplish the multiple angle evaporation, we have modified a Veeco 7760 Series high vacuum evaporator by implementing a rotatable sample stage that is cooled by cold N_2 gas. The maximum tilt angles are between $-70°$ and $+70°$ with respect to the source.

A two-step evaporation process is illustrated in Fig. 6.2. The first requires deposition of the ferromagnet with the source beam aligned perpendicular to the sample. This ensures that the ferromagnetic film lays flat on the Si substrate. In this manner, no additional pinning sites for the domain walls are introduced, as would be the case if the ferromagnet were deposited after the superconductor. In the second step, the superconductor is evaporated at a $30 - 45°$ angle with respect to the sample normal. This evaporation creates a shadow of the first, displaced by a distance that is dependent on the resist thickness and tilt angle.

The major challenge associated with successfully obtaining the desired geometry stems from the lithography process (dose and developing time) and obtaining good e-beam stigmation. In addition, getting a proper undercut, especially around the area of the nano-constriction, is particularly difficult as small fluctuations in the dose may produce undesired features or enlarge the notch.

6.1.2 Materials

For the ferromagnet, we have chosen Ni because it forms smooth films when evaporated and also due to the relatively low temperatures required to achieve suitable evaporation rates ($930 - 1070$°C for vapor pressures of $10^{-8} - 10^{-6}$ Torr). Another potential candidate for the ferromagnet is Co, with similar evaporator power requirements. For the superconductor, initial tests with Vanadium have produced films with T_C above 4.2 K. Another choice is Al, which can be evaporated easily but requires temperatures to be below 1.2 K in order for the Al to be superconducting.

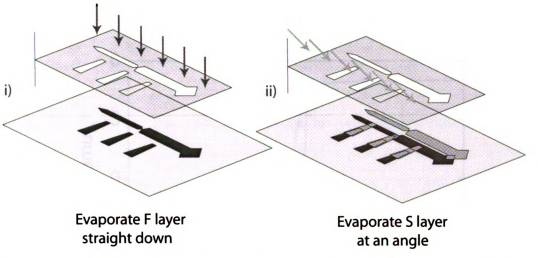

Figure 6.2: Shadow evaporation process through e-beam resist mask for long-range proximity effect experiment. i) Deposition of the F layer with source direction normal to the sample. ii) Deposition of the S layer at $30 - 45°$ angle with respect to sample normal (angle depends on the resist thickness and length of displaced shadow required).

In order to verify the magnetic qualities of the thermally evaporated Ni, we have deposited a 25 nm-thick film directly on a Si substrate, with base pressure in low 10^{-8} Torr range and a deposition pressure that is somewhat higher. Typical deposition rates are around $6 - 8$ Å/sec. Once deposited, the film is measured using a Quantum Design SQUID magnetometer giving its magnetic behavior with respect to an applied field. The results of magnetization measurements are summarized in the M vs. H plots of Fig. 6.3. Both the room temperature and low temperature data show excellent magnetic switching, with coercive fields of about 10 and 50 Oe, respectively, which indicates that the magnetic film is of good quality.

6.2 Domain Wall Trap

Since a major concern in the investigation of long-range proximity effect requires obtaining control of the magnetic structure of the ferromagnet, we have fabricated a submicron-size wire with strong shape anisotropy. Furthermore, drawing on an

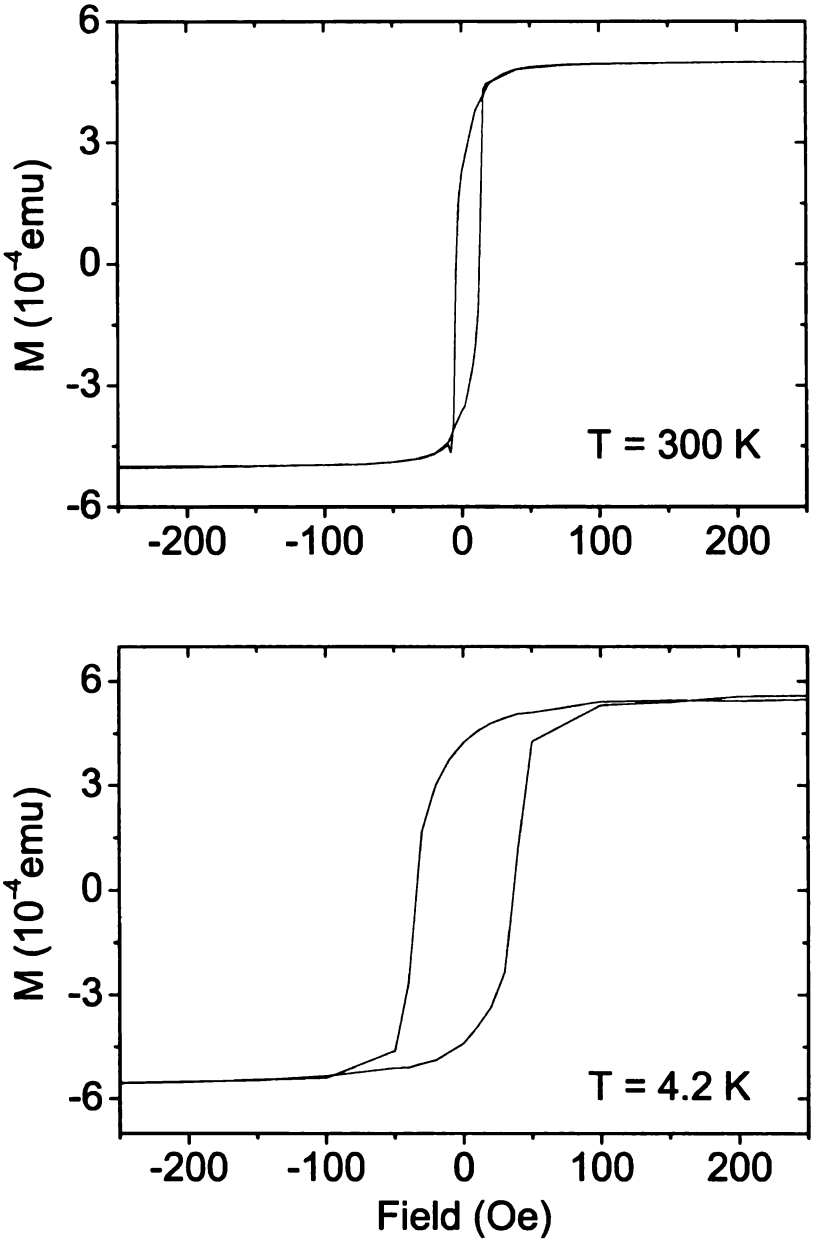

Figure 6.3: M vs. H for a thermally evaporated 25 nm-thick Nickel film deposited directly on a Si substrate. The measurements are taken at room and low temperature showing very good ferromagnetic behavior, yielding coercive fields H_C = 10 and 50 Oe, respectively.

earlier geometry by Shinjo *et al.* [80], which was designed to trap and measure the resistance of a single domain wall [81], we have implemented that design for our ferromagnets, as seen in Fig. 6.1. The ferromagnet sample geometry consists of two long "fingers" of different widths connected by a nano-constriction that serves as the domain wall trap. The large aspect ratio ensures that both fingers are single domain. The length of each finger is a few microns while the width is typically 150 nm for the small one and 200 nm for the larger one. The diamond head connected to the wider finger serves as a point for the nucleation of a domain wall. The more narrow finger switches at a higher field and its sharp tail prevents the nucleation of the domain wall there. Initially, a larger field is applied in the positive direction (to the right) so that the magnetization of both fingers are pointing to the right. Subsequently, when the magnetic field is applied in the opposite direction, a domain wall is injected from the diamond-shaped head and the magnetization reversal quickly takes place in the wider wire. Upon reaching the notch, the domain wall is trapped until the magnetic field is increased beyond the critical value necessary to sweep it past the nono-constriction.

6.2.1 Magnetic Force Microscopy

There are two methods for verification that the domain wall is trapped at the notch position. The first involves the use of a Magnetic Force Microscopy (MFM) technique, which utilizes a vibrating cantilever with a magnetically coated tip to measure the magnetic field gradients near the sample. Using this method, the presence of single magnetic domains can be detected. The MFM measurements are obtained by means of a two-pass scan method. The first pass measures the topography by tapping the cantilever directly on the surface of the sample, similarly to the Atomic Force Microscope (AFM) technique. In the second pass the cantilever is lifted to a specific height (usually around 50 nm) above the surface, being kept constant by using information from the stored topography. Fig. 6.4 illustrates how the magnetic measurement is

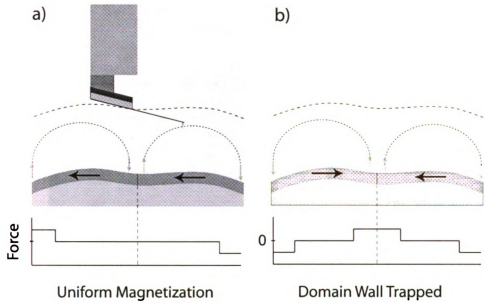

Figure 6.4: Magnetic Force Microscopy technique measuring field gradients from uncompensated magnetic poles to determine the domain structure. a) When both fingers are magnetized to the right, the only uncompensated magnetic poles are at the edges. b) When the fingers are magnetized in the opposite directions, there are also uncompensated poles at the notch area in addition to those at the edge of the sample.

performed in the second pass. The short-range Van der Waals forces are negligible and the cantilever is affected only by long-range magnetic force due to uncompensated magnetic poles.

We have used an MFM in order to observe the domain structure of the ferromagnetic fingers patterned according to Shinjo [80]. When both are magnetized along one direction, the only features visible in the MFM image are those produced at edges of the ferromagnetic sample. Fig. 6.5 illustrates a MFM image of Py fingers that are fully magnetized to the left by a large field. The image shows a bright spot at the diamond head and a dark spot at the other end, which corresponds to the schematic shown in Fig. 6.4 (a). When the magnetization directions of both fingers are pointing toward the notch, a bright spot appears at that location while the edges of the fingers are dark, as depicted in Fig. 6.4 (b). In order to apply a magnetic field while taking

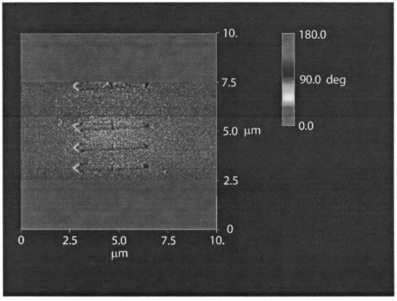

Figure 6.5: MFM image of sputtered Py fingers fully magnetized to the left corresponding to Fig. 6.4 (a). The bright and dark features are at the end of each finger illustrating that the magnetization points to the left.

an MFM image, a custom sample holder was designed and built, as shown in Fig. A.4 of the appendix, which utilizes a 1" rare earth bar magnet that moves on a calibrated track. The magnitude of field ranges from values of a few Oe up to 2000 Oe.

The difficulties associated with taking an MFM image in an external field is the fact that the magnetically coated tip responds to that field in addition to the sample field gradients. For large field values, the former may hinder the ability to obtain a good image. In addition, care must be taken with respect to the selection of the scan height of the cantilever above the sample and the oscillation amplitude. If the distance between the tip and sample is too large, the magnetic signals are too weak to be detected. However, if the distance is small, then one runs the risk of striking the surface and damaging the cantilever or picking up dirt from the surface, thus rendering the tip insensitive to the magnetic sample. Furthermore, since both the sample and the tip are magnetic, having the tip come in close proximity to the sample may affect its domain structure. Initial efforts to image a trapped domain wall at the nano-

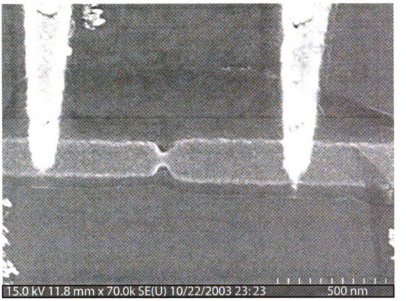

Figure 6.6: A thermally evaporated 30 nm-thick Ni wire with a notch size of around 50 nm and thick Ag contacts, fabricated using e-beam lithography and multiple angle evaporation. The resistance is measured across the notch as a function of the external field.

constriction were done using the MFM. However, it was never established whether the inability to successfully obtain such an image was due to the failure to trap the domain wall at the constriction or due to the reasons mentioned above.

6.2.2 Magnetoresistance

Another method for detecting the presence of a domain wall in the notch is to make a transport measurement across it, as shown in the device of Fig. 6.6, similar to the work of Miyake *et al.* [81]. In those experiments, a negative contribution to the resistance was observed when a 180° magnetization rotation was obtained at a nano-contact joining two NiFe wires. The authors attributed the change in the resistance due to the domain wall effect on the basis of Anisotropic Magnetoresistance (AMR). The latter effect represents the contribution to the resistivity of a ferromagnetic sample based on the orientation of the measurement current and magnetization.

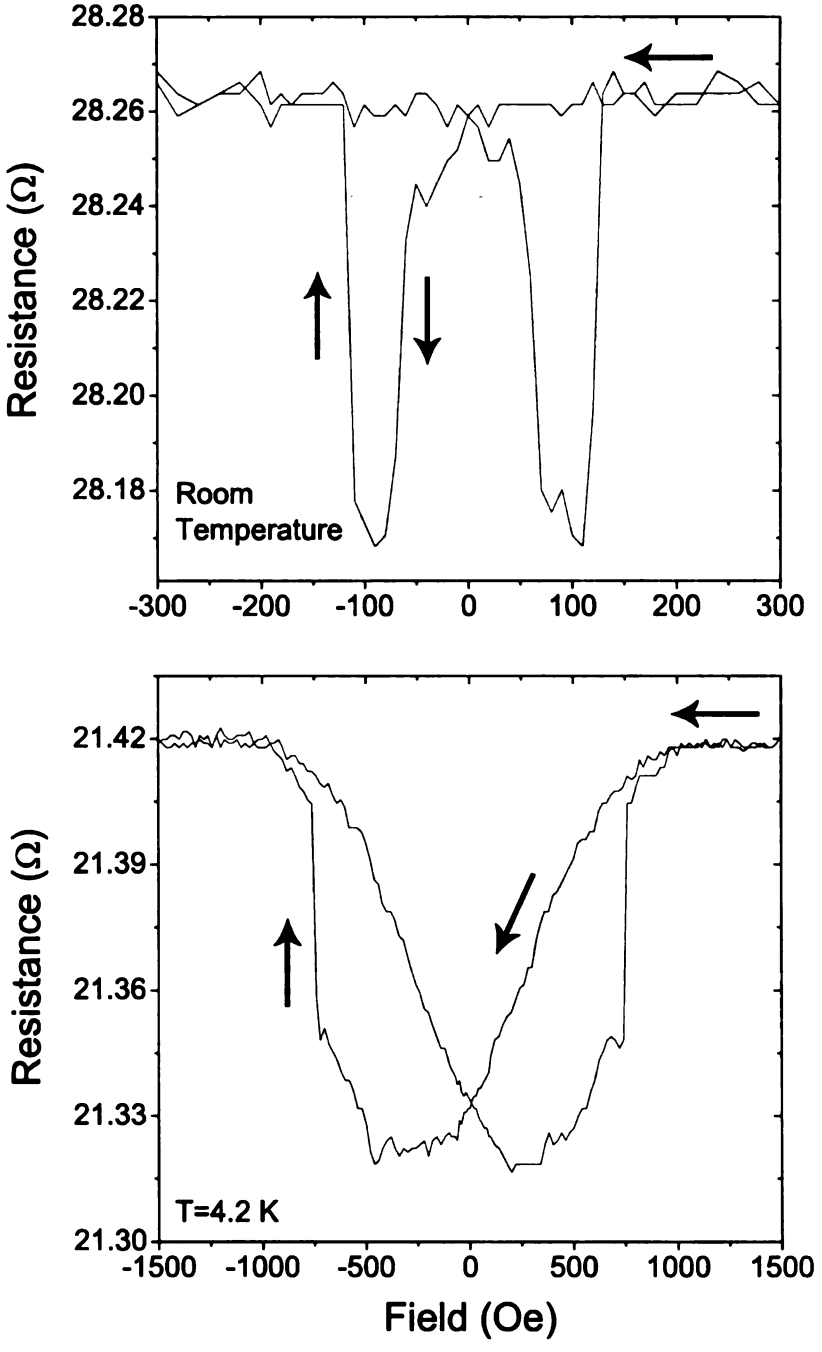

Figure 6.7: R vs. H for across a thermally evaporated 30 nm-thick Ni wire of submicron size (directly on a Si substrate) with a notch, similar to Fig. 6.6, taken at room temperature and 4.2 K. The contacting leads are 30 nm-thick Ag and the resistance measurement is AC with current of $20\,\mu A$. The arrows indicate field sweeps from positive to negative values.

We have utilized this magnetoresistance effect in order to confirm the existence of the domain wall at a notch in a ferromagnet. Fig. 6.7 shows the results of a R vs. H measurement across a notch in a 30 nm-thick Ni wire thermally evaporated on a Si substrate, similar to Fig. 6.6. The data were taken at room temperature and at 4.2 K. The contacting leads are Ag (30 nm) and the AC measurement current is $20\,\mu A$.

At room temperature, following the arrows in Fig. 6.7, a field greater than 125 Oe is enough to fully magnetize both magnetic fingers in the positive direction. Once the field is reduced to a value of ~ -50 Oe the resistance drops indicating the propagation to and presence of the domain wall at the notch. Upon further increase of the field in the negative direction, the resistance suddenly increases to the previous value, indicating the depinning and annihilation of the domain wall. The same behavior is observed when sweeping the field from -300 to $+300$ Oe.

A similar qualitative behavior is observed in the low temperature measurement. However, the field values required to fully orient both fingers in the same direction are greater than 1000 Oe. Furthermore, for the case of sweeping the field from positive to negative values, the resistance decrease takes place over a large field range, reaching a minimum at a field of -250 Oe before starting to increase somewhat. Increasing the field further, a sudden jump in the resistance up to the saturation value is observed around -750 Oe. The same behavior is observed by sweeping the field in the opposite direction. The nature and presence of the domain wall in the ferromagnetic finger influences the resistance value measured. The reason behind the gradual decrease in resistance observed over a broad field range is yet unclear. This is because once the magnetization of the fingers are saturated along one direction, it takes a field opposite to that direction to nucleate a domain wall, and once that happens, it propagates quite fast along the wires of sub-micron size [82]. One explanation may be that the magnetic structure around the notch is relaxing to an energetically favorable configuration once the field is reduced from a large value.

6.3 Future Outlook

We have successfully demonstrated the presence of a trapped domain wall at a constriction and to our knowledge this is the first such observation in a Ni wire. The width of the wall is given by the size of the constriction, roughly 60 nm for the sample that we have measured. The contribution to the resistance is negative when the domain wall is present in the notch. However, the ability to successfully trap the domain wall is directly related to the notch size and we have not been able to trap a domain wall in a notch with lateral dimension greater than 70 nm. Also, samples with notches that have smaller sizes cannot be obtained reproducibly. In addition, the effect of the measurement current becomes important, as was observed in work by Tsoi *et al.* [83]. In those experiments, their device design enabled the authors to distinguish between the various mechanisms of interaction between electric current and domain walls. They found that the current threshold for domain wall motion in a CoFe nano-constriction was found to be of the order $\sim 10^{11}$ A/m^2.

Taking into account the various complications arising from fabricating and measuring a long-range proximity effect device that can trap a domain wall in a notch, future experiments may require some simplifications in our design. Specifically, more recently it has been demonstrated that domain walls have been trapped in more simple devices, such as in wires containing bends [84] and also wires of different widths [85]. Such designs would reduce sample fabrication efforts considerably and would result in more consistent and reproducible results.

Chapter 7

Search for Triplet Pairing

In chapters 4 and 5 we described the results of an experiment where two ferromagnets were placed on both sides of a superconductor. This preliminary work was motivated by a much more difficult experiment aimed at verifying a prediction that a superconducting order parameter with spin triplet symmetry can be induced in a conventional superconductor in a F/S/F trilayer structure, where the ferromagnet magnetizations are non-collinear [29]. By proximity effect, the superconducting pair correlations with spin triplet symmetry can then propagate inside the ferromagnets at distances much larger than the conventional singlet coherence length dominated by the exchange field, namely

$$\xi_F^{singlet} = \sqrt{\frac{\hbar D_F}{2E_{ex}}} \tag{7.1}$$

as given in Eqn. 2.30. However, the successful observation of the triplet state requires probing the parameter space for the optimal material combinations and thicknesses. This chapter will describe the theoretical prediction of the triplet state and also the experimental conditions required for its direct observation.

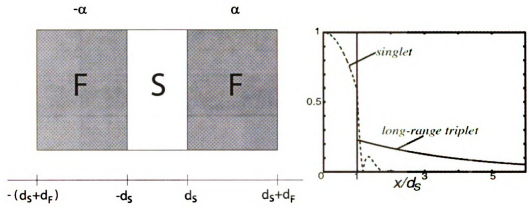

Figure 7.1: The proposed mechanism for inducing a triplet state in a conventional superconductor, where α is the angle between the ferromagnet magnetization and the vertical axis, by Bergeret *et al.* [29]. The triplet state penetrates inside a ferromagnet over a much longer length scale.

7.1 Bergeret/Volkov/Efetov Prediction

In their theoretical work, Bergeret *et al.* [29] show that in a multilayered superconductor-ferromagnet structure with a noncollinear alignment of the magnetizations of the ferromagnetic layers, as shown in Fig. 7.1, a triplet superconducting condensate that is odd in frequency is generated. In a system that utilizes a conventional superconductor, both singlet (SC) and triplet (TC) condensate components are shown to coexist. In the case of collinear magnetization ($\alpha = 0, \pi/2$), both components decay inside the F layer over a length scale set by the exchange field, Eqn. 7.1. However, if the magnetization directions are not collinear, the TC appears with a non-zero projection and the correlations penetrate over a longer length scale,

$$\xi_F^{triplet} = \sqrt{\frac{\hbar D_F}{2\pi k_B T}} \tag{7.2}$$

which is the same as the normal coherence, ξ_N, given in Eqn. 2.22. To obtain an estimate for its value in Ni, we use $D_F = 6.7$ cm^2/s which gives $\xi_F^{triplet} = 20$ nm at $T = 2$ K. At dilution refrigerator temperatures, this length exceeds 140 nm.

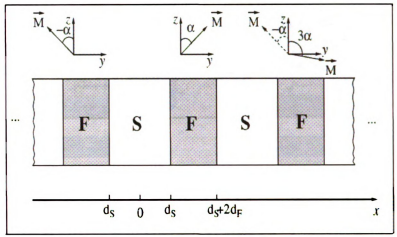

Figure 7.2: Multilayer geometry proposed by Volkov *et al.* [30] for the observation of the triplet state. The triplet correlations induced by non-collinear ferromagnets can penetrate the inner ferromagnet over a longer length scale as compared to the singlet ones, and Josephson couple the two superconductors.

The existence of superconducting correlations in the ferromagnet results in the modification of the density of states (DOS), which at large enough distances from the F/S interface is only due to the triplet condensate. However, the resulting change in the DOS as compared to that of the normal ferromagnet is predicted to be rather small, of order $\sim 10^{-3}$. Since measurements of the DOS are usually performed using tunneling spectroscopy experiments, which pose their own challenges, and given the size of the signal, we have not attempted to observe the triplet state by this method.

Another implication of the existence of long range coherence of the triplet state is that it should lead to a Josephson coupling between the superconductors separated by a ferromagnet of thickness greater than $\xi_F^{singlet}$, in a geometry such as that shown in Fig. 7.2 [30]. This can be intuitively understood by the fact that an exchange field will inherently break a singlet Cooper pair consisting of two electrons with opposite spins, whereas a triplet pair will not be affected in this manner, and will propagate in the ferromagnet over a longer distance. If the angles of the magnetizations of the ferromagnets with respect to the vertical axis are $-\alpha$, α and $-\alpha$, respectively, then the system is said to have negative chirality, while for $-\alpha$, α and 3α then the

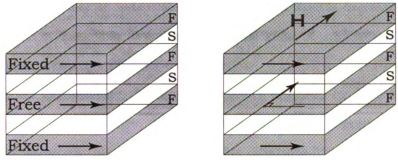

Figure 7.3: Magnetic structure for triplet experiment. Both outer ferromagnets are adjacent to an anti-ferromagnet that fixes their direction by exchange bias. The inner ferromagnet is free to move by a magnetic field. In this manner, the negative chirality proposed by Volkov *et al.* is obtained.

system has positive chirality. Consequently, depending on the mutual direction of the ferromagnetic moments, the Josephson coupling can be both of 0 and of π type for different signs of the order parameter. The successful observation of this effect implies, however, that spin coherence in the F layer as well as across the F/S interface be maintained.

7.2 Preliminary Work

In the proposed multilayer by Volkov *et al.* [30], the Josephson junction voltage measurement is taken across the two inner superconducting layers. For this reason, we have designed the device as illustrated in Fig. 3.3, containing a 5 component masking system that results in samples with separate voltage and current leads. In addition to the configuration of the leads, there is the requirement for the magnetic structure of the device. The presence of a triplet component to the order parameter requires that the arrangement for the magnetizations of the ferromagnets must have the positive or negative chiralities shown in Fig. 7.2. In order to obtain the needed magnetic

configuration, the ability to independently control each layer is necessary and can be done through exchange bias or by varying the thickness of the ferromagnets, thus providing different coercive fields for each layer.

The method for obtaining the negative chirality proposed by Volkov *et al.* is illustrated in Fig. 7.3 illustrates. The outer ferromagnets are deposited next to an anti-ferromagnet, which then sets their respective directions by exchange bias, while the inner one is able to rotate freely. After an in-field pinning procedure at 180° C, all ferromagnets are pointing along the same direction. However, once a magnetic field is applied in the plane of the films at a right angle with respect to the pinning direction, the non-collinear configuration can be achieved. Consequently, by rotating the field in the plane of the sample one can switch between having a singlet order parameter only and inducing a triplet state.

7.2.1 Singlet Josephson Junctions

In the early stages of this work, Nb/Co was the first system used in the investigation of the proposed triplet component to the order parameter described in the previous section. As a first step, the establishment of the length scale over which the conventional singlet state penetrates a ferromagnet was required. In order to do that, we have fabricated conventional S/F/S Josephson junctions, whose typical V-I characteristics are illustrated in Fig. 7.4. The data shown is from a sample with Nb(150)Cu(5) current and voltage leads on either side of a Co(4)Cu(5) layer. The thin Cu layers deposited on the ferromagnet and superconductors are utilized in order to prevent oxidation, and they are rendered superconducting due to the conventional S/N proximity effect. The sample geometry is given in the insert to Fig. 7.4, showing that the current is flowing perpendicular to the layers through an area of about 1.2 mm^2. The critical current, I_C, for the sample shown is around 30 mA measured at 4.2 K. The V vs. I plot shows a zero voltage drop for $I < I_C$ and recovering an Ohmic behavior

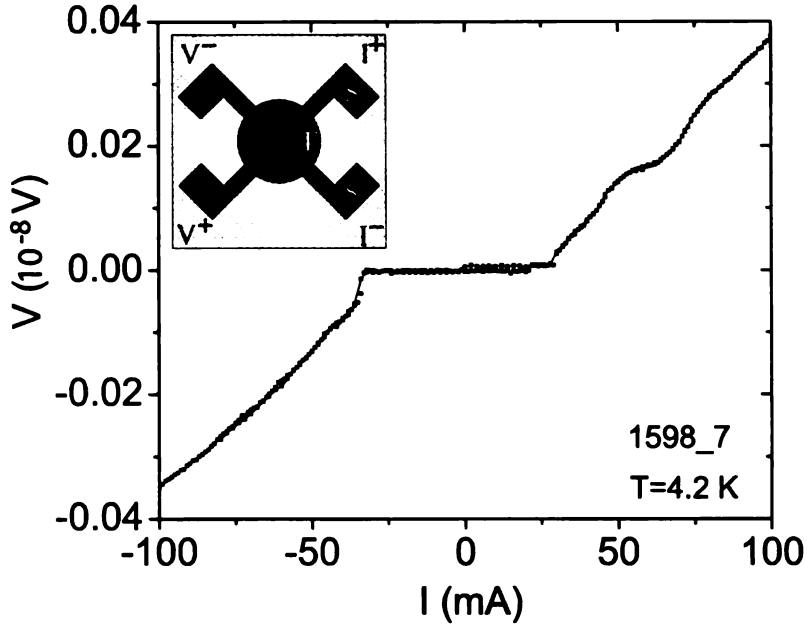

Figure 7.4: V vs. I for a Superconductor/Ferromagnet/Superconductor Josephson junction made of Nb(150)Cu(5)/Co(4)Cu(5)/Nb(150)Cu(5). The sample geometry is shown in the insert, with the current flowing perpendicular to the plane (CPP). The area of the junction is around 1.2 mm^2.

for $I \gg I_C$.

By performing similar measurements, one can trace the dependence of the critical current on the thickness of the Co layer. Fig. 7.5 shows the R vs. I results for Nb(150)/Cu(5)Co(d_{Co})Cu(5)/Nb(150) samples. I_C varies from around 25 mA for $d_{Co} = 4$ nm all the way to zero for $d_{Co} \gtrsim 10$ nm. The resistances of these samples are shown to be in the nΩ regime, and therefore required the SQUID measurement techniques described in Chapter 3. All of the sample measurements were made at 4.2 K. Based on information from these S/F/S samples, we concluded that there is no super-current due to conventional superconductivity for samples where d_{Co} is larger than 10 nm. Therefore, making the ferromagnet layer larger than this thickness and observing a zero voltage Josephson effect will ensure that it is only the triplet component which contributes to the super-current.

Another important parameter for the triplet state experiment is the thickness of

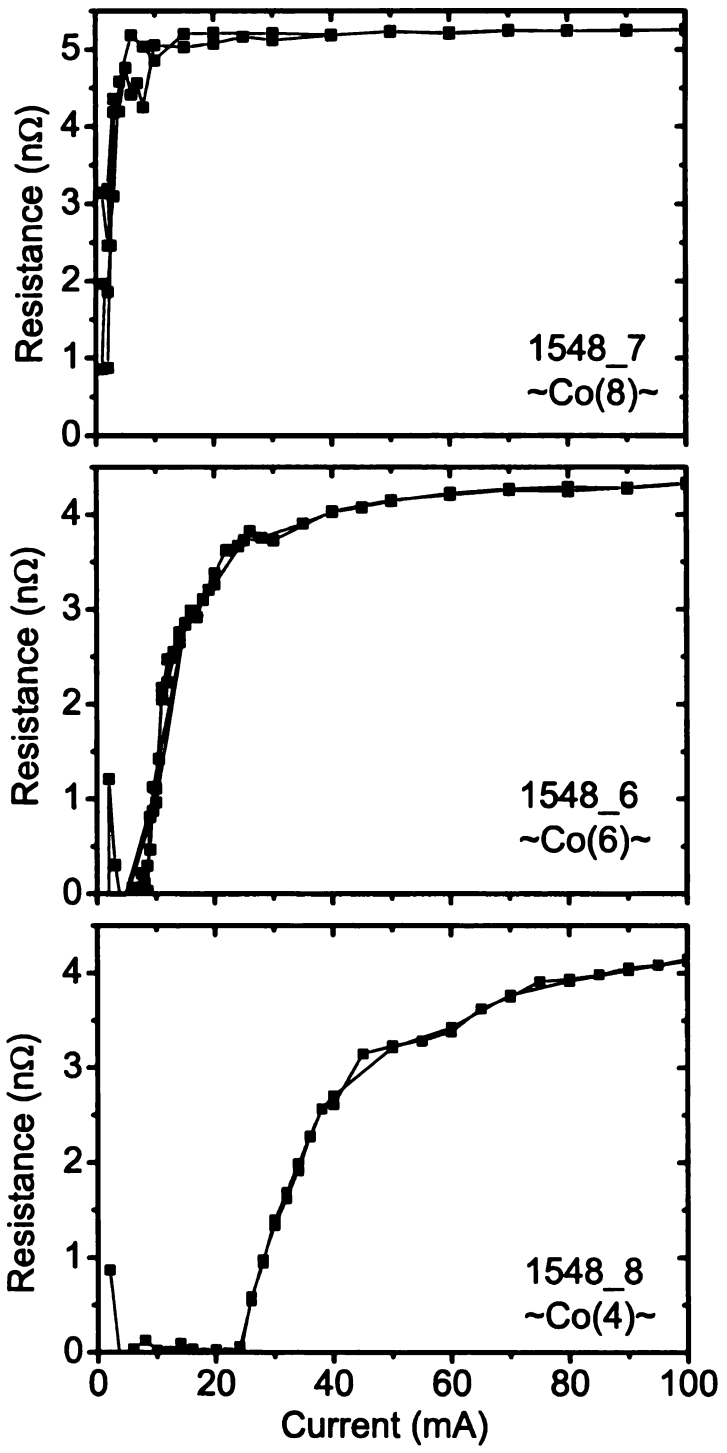

Figure 7.5: R vs. I for Nb(150)/Cu(5)Co(d_{Co})Cu(5)/Nb(150) samples with different Co thicknesses in the geometry shown in the insert to Fig. 7.4. The data illustrate Josephson junction behavior, showing a decrease in critical current, I_C, as d_{Co} is increased. No supercurrent is detected for $d_{Co} \gtrsim 10$ nm. All measurements are taken at T=4.2 K.

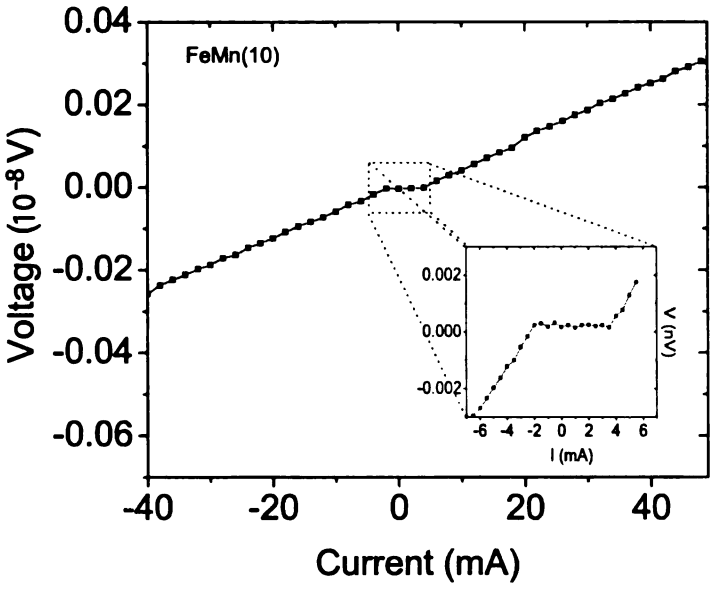

Figure 7.6: V vs. I for a Superconductor/Anti-Ferromagnet/Superconductor Josephson junction made of Nb(150)Cu(5)/FeMn(10)Cu(5)/Nb(150)Cu(5) with $I_C = 3$ mA.

the superconducting layers, d_S. Making the layers too thin will risk their not being superconducting at the temperature of our experiment, while making them too thick will render them insensitive to the magnetization of the ferromagnets that surround them. Therefore, we have fabricated Cu(20)Co(3)Nb(d_{Nb})Cu(2)Co(3)Cu(20) multilayer test samples in order to establish the dependence of the critical temperature on d_{Nb}. The T_C was obtained by 4-terminal resistive methods. The results yielded $T_C(d_{Nb} = 30, 33, 36 \text{ nm}) = 5.0$, 5.3, 5.6 K. Utilizing a value for d_{Nb} near 30 nm will ensure that the S layers are superconducting at the liquid helium temperature. Extending our SQUID capability to our dilution refrigerator will allow the fabrication of samples with thinner d_{Nb}.

One issue of concern is the presence of pinholes in our thin Co layer that separates the superconductors, which would weakly link the latter and give a Josephson behavior in the V-I measurement. The dirty limit coherence length for Co is estimated to be around 2 nm using $v_F \sim 2 \cdot 10^6$ m/s and $E_{ex} = 120$ meV [86], and so the singlet order parameter should decay on this length scale. Since the critical current scales

exponentially with the ferromagnet thickness, $I_C \propto \exp(-d_{Co}/\xi_F)$, the existence of super-current in the data of Fig. 7.5, for a Co thickness that is greater than a couple of nm, seems to indicate the presence of weak links between the superconductors. To verify this, we performed an additional test by making an Superconductor/Anti-Ferromagnet/Superconductor junction using a 10 nm thick $Fe_{50}Mn_{50}$ layer. The anti-ferromagnetic alloy may cause strong enough spin-dependent scattering so that no Josephson current should exist for thick FeMn layers. This is supported by experiments of Bell *et al.* [87] in which a coherence of 2.4 nm was found in a disordered fcc γ-$Fe_{50}Mn_{50}$ alloy. Our V-I measurement seemed to confirm suspicions for the presence of pinholes, as a small Josephson current of 3 mA was indeed observed through a thicker FeMn layer in a Nb(150)Cu(5)/FeMn(10)Cu(5)/Nb(150)Cu(5) sample, as shown in Fig. 7.6.

The presence of pin-holes in our proposed experiment can prevent the observation of the triplet state, as the size of the signal that we would be measuring can be small. Therefore, in addition to increasing the Co thickness, one method for limiting the number of pinholes that can couple the two superconductors is to reduce the area of the junction.

7.2.2 Triplet Josephson Junctions

Using the preliminary data from S/F/S Josephson junctions, we then fabricated the proposed devices illustrated in Fig. 3.3, using the Nb/Co system. Fig. 7.7 shows the V vs. I characteristics for samples taken at 4.2 K, whose lead configuration and descriptions are given in Table 7.1. The data sets are taken for samples with $d_{Nb} = 35$ nm and $d_{Co} = 6$ and 15 nm. Each plot shows the V-I measurements taken in zero field as well as in a 500 Oe applied field, as described in Fig. 7.3, corresponding to a parallel and negative chirality magnetic configuration, respectively. The latter set of data are displaced vertically in the V vs. I plot for clarity. For the sample

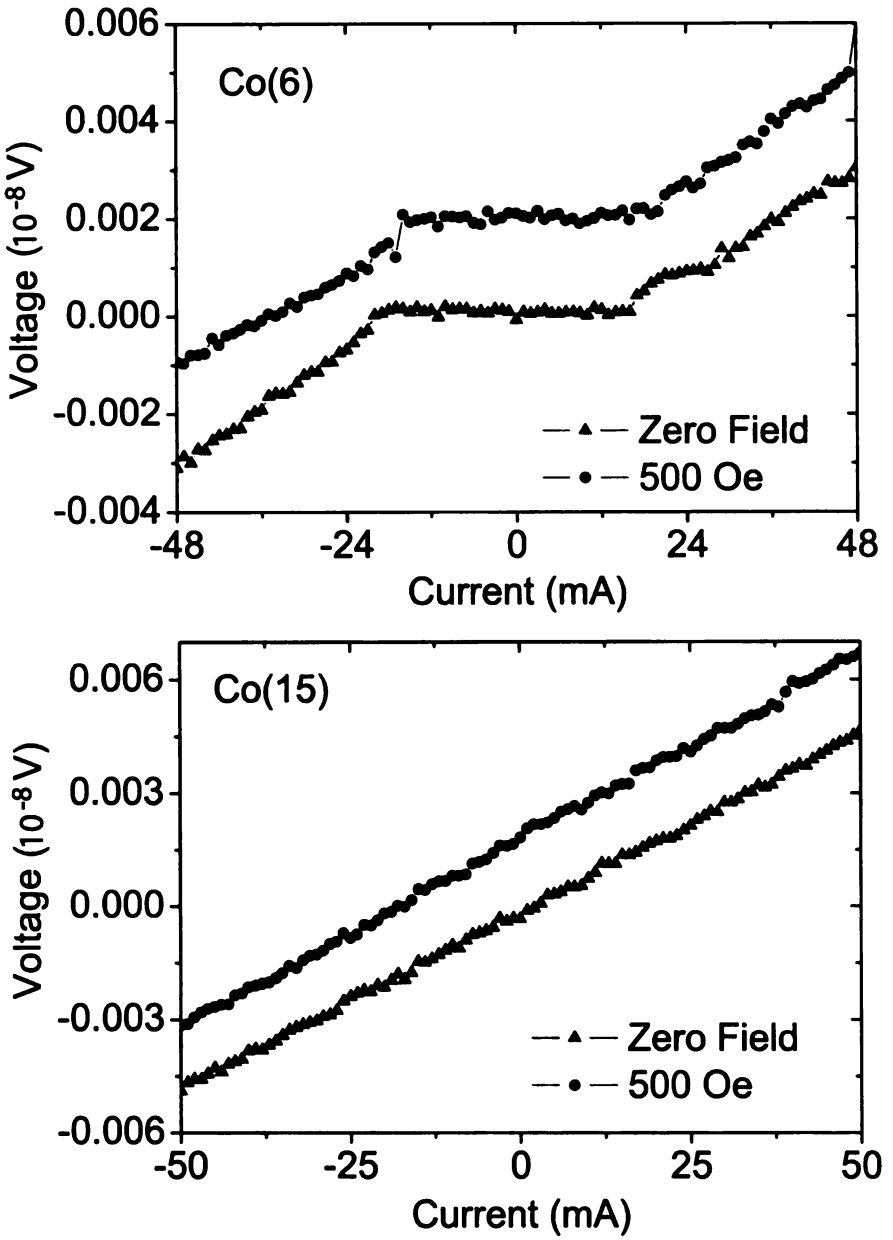

Figure 7.7: V vs. I for devices made according to Fig. 3.3 where the layers are as follows: i) Nb(100). ii) Cu(10)FeMn(8)Co(5)Cu(5)Nb(35)Cu(5). iii) Co(d_{Co})Cu(5) iv) Nb(35)Cu(5)Co(5)FeMn(8)Cu(10). v) Nb(100). The top plot shows a Josephson junction for a sample where the inner Co layer is 6 nm thick, with no appreciable difference between the 0 field (parallel) and the one taken in 500 Oe (perpendicular). The bottom plot shows standard Ohmic behavior for a device with $d_{Co} = 15$ nm. There is no change in behavior with an applied field. The in-field plots are vertically displaced for clarity.

with d_{Co} = 6 nm, a Josephson junction is visible for both field orientations, with no detectable difference in I_C. The existence of long range triplet state would, in principle, increase I_C. In addition, for d_{Co} = 15 nm, an Ohmic behavior is observed for both configurations, and thus showing no indication of the existence of triplet state Josephson coupling the two superconductors.

Step		Description
i	Nb(100)	I^+
ii	Cu(10)FeMn(8)Co(5)Cu(5)Nb(d_{Nb})Cu(5)	V^+
iii	Co(d_{Co})Cu(5)	–
iv	Nb(d_{Nb})Cu(5)Co(5)FeMn(8)Cu(10)	V^-
v	Nb(100)	I^-

Table 7.1: Triplet sample description.

Subsequent samples were made with reduced thickness for the superconducting layers, namely d_{Nb} = 27.5 and 25 nm. In order for the Nb layers to be superconducting, the measurements were performed at temperatures below 4.2 K in a modified Quick Dipper system built by W.P. Pratt, designed to reach a base temperature of 1.6 K by pumping on He^4. The results of those experiments, however, were similar to the ones quoted above in that no indication for the presence of a triplet order parameter penetrating a ferromagnet over a long range was detected. However, as we have argued before, the sensitivity of the superconductor to the ferromagnets must be further enhanced by reducing the thickness. Consequently, experiments similar to those performed in chapter 4 will need to be performed in order to establish whether the Co/Nb system is a viable candidate for the observation of the triplet state.

7.3 Alternative Experiment

After performing the Ni/Nb trilayer experiments described in chapter 4, the degree to which the critical temperature is suppressed by the addition of ferromagnetic Ni on both sides of the superconducting Nb is known. From the data we have extracted

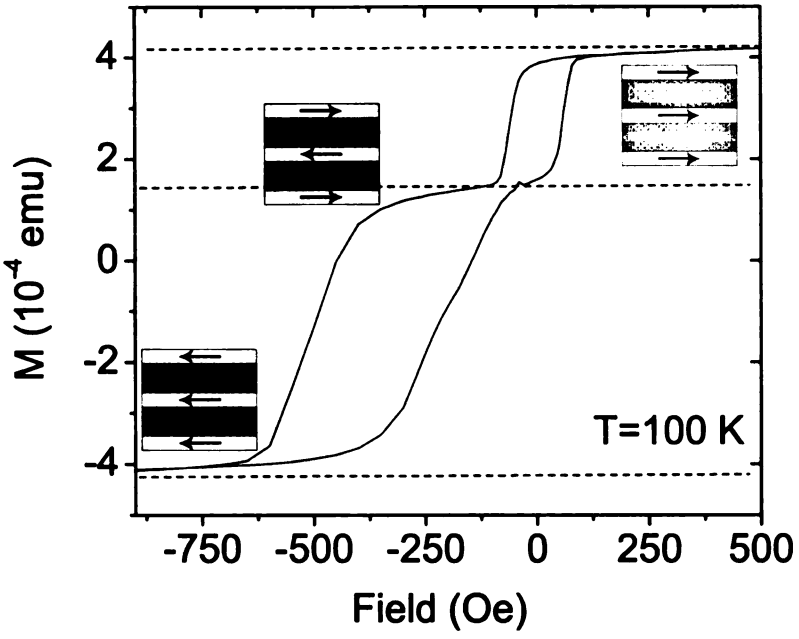

Figure 7.8: M vs. H for a FeMn(8)Ni(8)Nb(25)Ni(8)Nb(25)Ni(8)FeMn(8)Nb(2) structure taken at 100 K, which was grown on a Nb(5)Cu(10) buffer layer. The minor loop demonstrates the switching of the free layer while the major loop represents the almost simultaneous switching of both pinned layers.

the critical thickness for which superconductivity is almost fully suppressed. If we wish to observe the triplet state using this F/S system, we must work close to the critical thickness and hence at low temperature, where the Nb is most sensitive to the orientation of the two ferromagnets.

Similar to the previous section, in order to obtain the negative chirality, a possible device arrangement is FeMn/Ni/Nb/Ni/Nb/Ni/FeMn. Here, again, the two FeMn layers serve to fix both of the outer Ni ferromagnets while the inner one is left free to rotate. Since FeMn usually grows well on Cu, a deposition in this manner results in good exchange bias properties. However, its behavior due to deposition on top of a multilayer stack terminating in Ni is not known. Therefore, in order to be sure that proper pinning of both ferromagnets in our proposed heterostructure is accomplished, a FeMn(8)Ni(8)Nb(25)Ni(8)Nb(25)Ni(8)FeMn(8)Nb(2) test sample was grown on top of a Nb(5)Cu(10) buffer layer. After pinning, the magnetic behavior of the structure

was measured (shown in Fig. 7.8). The field is applied along the direction of the pinned ferromagnets. The buffer layer is to ensure that the bottom FeMn layer is not deposited directly onto the Si substrate, which may affect its ability to pin the direction of the ferromagnet above it. After inspecting the M vs. H data, the free layer switches at around 60 Oe and the exchange bias of both pinned layers cannot be distinguished at 500 Oe, which indicates very good magnetic switching of the entire structure.

Similar to the Nb/Co devices of Table 7.1, one can replace the Co with Ni and use $d_{Ni} \geqslant 15$ nm for the inner F layer and $d_{Nb} \gtrsim 17$ nm for the S layers. The latter thickness choices are made in accordance with the results of chapter 4, which ensure a junction free of pinholes and allows for a maximum sensitivity of the Nb layers to the ferromagnetic Ni with critical temperature between $0.5 - 1.5$ K. Since the resistance measurements are in the nΩ range, the use of a SQUID device is required and we are currently in the process of adding this capability to our top-loading dilution refrigerator, and thus combine an ultra-low temperature capability with a low resistance measurement scheme (Appendix A).

Alternatively, a slight modification to the geometry can be made in order to avoid the difficulty of measuring very low resistance samples at the lowest temperatures of our dilution refrigerator. Therefore, instead of using a CPP-type geometry, a modified CIP-type can be utilized, as shown in Fig. 7.9, which is intended to increase the normal state resistance of the device. The magnetic behavior of this device is already known from studies of Ni/Nb/Ni trilayers, and therefore no further measurements are required. Making the samples involves the deposition of a 4-terminal Cu(30)/Ni(8)/Nb(17-19)/Ni(8)/FeMn(8)/Nb(2) multilayer structure (with all thicknesses in nm) patterned by e-beam lithography and lift-off process, with an area of 10 x 2 μm^2 (shown in Fig. 7.9). In a subsequent lithographical step, a line in the resist is written across the center of the device. Using the e-beam resist as a mask,

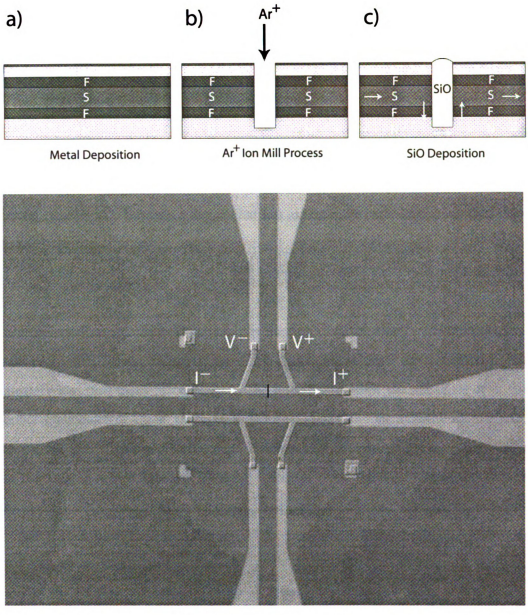

Figure 7.9: Proposed 4-terminal device to observe triplet superconductivity. a) Deposition of Cu(30)/Ni(8)/Nb(17-19)/Ni(8)/FeMn(8)/Nb(2) multilayer. b) Ion Mill process creating a trench of around 100 nm lateral dimension down to the bottom Cu layer. c) SiO deposition to prevent oxidation of exposed layers around the trench. Each chip contains two 4-terminal devices. The current is perpendicular to the layers near the trench, in the plane in the bottom Cu layer, and shorting through the superconductor elsewhere in the device.

an ion-mill process eliminates the top Ni/Nb/Ni/FeMn/Nb layers in the form of a 100 nm wide trench (as shown in 7.9 (b)), so that the current connecting the now separated superconducting layers has to travel through the bottom ferromagnet and Cu layers, respectively. Care must be taken to calibrate the ion-mill rates for the different materials, as small errors in the mill time compound quickly while ion-milling through the entire structure. After the removal of the desired material, the trench is covered with an insulating SiO layer in order to prevent the oxidation of the exposed materials around the trench. Each chip contains two samples, which can serve to make a comparison between a device that has an ion-milled trench and one that does not.

The existence of a triplet state will Josephson couple the two superconductors through the CPP Ni(8) / CIP Cu(30) / CPP Ni(8) layers, respectively. The normal resistance will essentially be dominated by the thin Cu layer which is left after the ion-mill process. However, an important factor that limits coherence is the amount spin memory loss that takes place either at the interface between the materials or in the bulk. The choice of Cu as the bottom layer is due to its long spin-diffusion length, $l_{sf} \approx 500$ nm. This is necessary for maintaining spin coherence over the length of the trench, whose smallest attainable size by current lithographical methods is around $60 - 100$ nm. Multilayer experiments based on the Giant Magnetoresistance (GMR) effect have measured the spin diffusion length of Ni, yielding $l_{sf} \approx 21$ nm [77]. However, the geometry proposed above has two Ni/Cu interfaces in addition to the Ni/Nb ones. Consequently, the contribution to the spin memory loss by the interfaces may prove to be the dominant in these devices.

Chapter 8

Summary of Results

The main aim of this thesis has been to study proximity effect resulting from placing a ferromagnet in contact with a superconductor. Initial experimental interests focused on determining whether the presence of a domain wall in the vicinity of an F/S interface has any influence on the proximity effect and if a long-range penetration of correlations in the ferromagnet could be observed, as reported by several other groups. Our goal was to obtain unambiguous experimental evidence by fabricating samples in which the ferromagnet magnetization could be clearly defined and well controlled. In addition, we wanted to take advantage the expertise acquired by our group in multiple-angle lithography techniques in order to obtain a pristine F/S interface by depositing both materials within the same vacuum. The latter required the refurbishing of a thermal evaporator with the high power capabilities and also the addition of a multiple-angle sample mounting system.

The appearance of a new and perhaps related opportunity in F/S systems, along with technical difficulties associated with the long-range proximity effect project, resulted in a redirection of the experimental studies. Specifically, Bergeret *et al.* [3] made the prediction that a triplet pairing mechanism can be induced in a conventional superconductor by the presence of inhomogeneous magnetization in the contacting ferromagnet. This can be accomplished by fabricating F/S/F trilayer structures,

where the magnetization of the ferromagnets are non-collinear. In such a system, the triplet state correlations, composed of electrons with the same spin direction, are affected in the same way by the exchange field of the ferromagnet. Therefore, the extent of their penetration can be much longer as compared to a singlet Cooper pair. Bergeret *et al.* proposed that the triplet state is responsible for the long-range proximity effects observed in the F/S experiments of Giroud *et al.* [25], Petrashov *et al.* [26] and Lawrence *et al.* [27]. In addition, in an F/S/F/S/F multilayer structure, a Josephson current solely based on triplet correlations may be observed between the superconductors when the thickness of the ferromagnet that separates them is larger than the penetration of the singlet order parameter [30].

Initial attempts proved inconclusive as no Josephson coupling based on the triplet state was observed in a Co/Nb/Co/Nb/Co system with non-collinear directions for the ferromagnet magnetizations. It turns out, however, that the problem is much more difficult as there are many parameters, including layer thicknesses and interface transparency, which influence the nature of the propagation of the order parameter. Consequently, a much simpler experiment was devised in order to establish the range of relevancy for the various variables associated with the F/S system. Specifically, it has previously shown using weak ferromagnets [11] that in a F/S/F trilayer structure, the critical temperature, T_C, depends on whether the orientation of the outer ferromagnets is parallel (P) or anti-parallel (AP). The AP state gives a gives a higher T_C as compared to the P state since the net field to the two ferromagnetic layers is slightly lower. Therefore, for a chosen F/S system, obtaining a large difference in the critical temperature, $\Delta T_C \equiv T_C^{AP} - T_C^P$, based on the orientation of the ferromagnets would indicate a good candidate for the triplet experiment.

For performing the F/S/F experiment, we decided that Ni/Nb system would provide a good starting point, as previous experiments on bilayers indicated good interface transparency between the two materials. We have chosen to work with strong

ferromagnets since a large exchange energy results in more pronounced proximity effects. Since our ultimate goal is the observation of a triplet order parameter, with a penetration length is dominated by temperature according to

$$\xi_F^{triplet} = \sqrt{\frac{\hbar D_F}{2\pi k_B T}}, \tag{8.1}$$

a strong effect of the ferromagnets on the superconductor is desired. The limiting factor is the ability to retain superconductivity at the base temperature of our measurement capability.

In chapter 4, the results of T_C measurements on the Ni/Nb/Ni are outlined [31], yielding a ΔT_C as large as 41 mK between the P and AP states of the magnetization for the two ferromagnets, the largest observed at a lower temperature [31]. The latter occurs close to the critical thickness for Nb in contact with two Ni layers, namely $d_{Nb}^{cr} = 16.5$ nm. The temperatures needed to observe the transitions close to this thickness (around 300 mK), however, require the use of dilution refrigeration methods, as superconductivity is strongly suppressed by the presence of the ferromagnets. From our experiments, we observe no difference between the two magnetization states for thicknesses above 21 nm for the Nb layer. Therefore, for the triplet experiment, one must work in the lower part of the narrow thickness range ($17 - 21$ nm), where the superconductor feels the effect of the ferromagnet magnetizations the most.

We have also performed measurements on a $Ni_{0.80}Fe_{.20}$/Nb/$Ni_{0.80}Fe_{.20}$ system, which yielded a $\Delta T_C = 20$ mK, where the Nb thickness close to $d_{Nb}^{cr} \approx 20.5$ nm. The results are consistent with our Ni/Nb system but opposite to ones reported in experimental work by Rusanov *et al.* [60]. In that work, the P state was shown to have a *higher* T_C than that of the AP state for the same trilayer system. This indicates that there are still unanswered questions in F/S, which may be related to materials' issues. In attempting to find other potential candidates for the triplet experiment, we have also performed preliminary studies on Co/Nb/Co and Gd/Nb/Gd trilayers. These

have given critical thicknesses around $d_{Nb}^{cr} \approx 22 - 24$ and $d_{Nb}^{cr} \approx 25 - 27$ nm for the complete suppression of T_C, respectively. However, the ability to successfully acquire the AP state and thus measure a nonzero ΔT_C has yet to be realized in these systems. In the case of Co, this may help explain why initial efforts aimed at confirming the existence of a triplet state in Co/Nb/Co/Nb/Co samples were unsuccessful.

We have applied the theories of Tagirov [32] and Fominov [33], which are formalisms based on the Green's functions method to treat superconductivity. We have obtained fits for our T_C vs. d_{Nb} and ΔT_C vs. T_C data obtained for the Ni/Nb/Ni and $Ni_{0.80}Fe_{.20}$/Nb/$Ni_{0.80}Fe_{.20}$ systems. Although neither theory takes into account the difference between the minority and majority spin bands, which should be non-negligible for strong ferromagnets, we have obtained good agreement to our data. Fits using the Fominov method yielded an interface parameter, R_BA, which can be used to quantify the quality of the F/S interface and compare it with values obtained from multilayer experiments. The fits indicated a value $R_BA = 2.3$ fΩ m^2 for the Ni/Nb interface, while for $Ni_{0.80}Fe_{.20}$/Nb, $R_BA = 1.5$ fΩ m^2.

8.1 Future Directions

Considering the progress achieved in the Ni/Nb/Ni trilayers, the first set of experiments will utilize this system in the proposed geometry of Volkov *et al.* [30], aimed at verifying the existence of the triplet state and its ability to propagate over a long length scale inside a ferromagnet. Given that the sample resistances are in the nΩ range and that the largest proximity effects are observed at the lowest temperatures, the triplet experiment will require the implementation of SQUID capability in our dilution refrigerator. Current efforts are already underway, as the fabrication of new probe and load-lock system, which deliver the sample inside the dilution refrigerator, are nearing completion (see Appendix). We have purchased a SQ1200 dcSQUID from STAR Cryoelectronics, LLC fitted with Model PFL−100 Program-

mable Feedback Loop, PC−100 single-channel electronics and control software, which await implementation and testing.

As illustrated in chapter 7, an alternative lateral sample design can be utilized in order to accomplish a geometry similar to the one suggested by Volkov *et al.* for the observation of the triplet state. The slight modification in the proposed layer structure, namely F/S/F/N/F/S/F instead of F/S/F/S/F, should not significantly affect the triplet Josephson current between the two superconductors. If a judicious choice is made with respect to the N material being used, no significant spin memory loss should take place in the bulk of N layer, although the additional F/N interfaces may prove to be the limiting factor with regard to spin memory. A good candidate is Cu, with has a long spin diffusion length, $l_{sf} = 500$ nm. An advantage of this sample design is that it utilizes currently available measurement capabilities and thus could be attempted right away. Fabrication efforts of this sample type are currently ongoing as well.

Appendix A

Appendices

A.1 Dilution Refrigerator Probe with SQUID

The following represent the work that is in progress on a dilution refrigeration probe designed to have a dc SQUID with the capability of making ultra-low temperature measurements on samples with resistances in the nΩ range. The probe represents the delivery mechanism for the sample and its respective wiring inside the dilution refrigerator. Since the sample is directly inserted in the He^3/He^4 mixture and can be removed in order to measure another while the system is cold, a load-lock mechanism must be provided in order to make a seal between the atmosphere and the mixing chamber. The probe and load-lock system are shown in A.1.

The probe design was based on an existing model manufactured by Oxford to supplement the dilution unit. However, given the size of the SQUID device with its shield housing, we have purchased a 73' long 7/8" diameter stainless steel tube with a 0.030" wall thickness. The finish of the tubing must be pristine as scratches along the length may result in leaks. The tubing is to be attached to an already existing lower insert by way of a welded or soldered metallic bushing, Fig. A.2 (b). The 22.9" long lower insert contains thermal anchors made of Cu and G10 insulating cylinders, shown in Fig. A.2 (a), whose largest outer diameter is 0.865". The way in which the SQUID housing is attached to the top of the insert (made of Cu) is shown in A.2 (b).

The top of the probe contains a commercially available vacuum manifold in the shape of a 4-way NW 25 cross, seen in Fig. A.2 (c). The stainless tube is welded to one of the openings, while the others serve as connection points for experimental wiring. The NW blanks can be fitted with standard ISO-KF flange connectors (for example www.sercoseal.com) as well as filtered connections (for example Glenair Pi filter hermetic connectors) secured with epoxy.

In addition to the probe, the load-lock is made of a stainless steel 1" diameter tube with a long flange NW25 stub welded at one end and a custom-made sliding seal at the other (Fig. A.3). The gas handling manifold (Fig. A.1 (e)) uses stainless Swagelock valves attached to 1/4" stainless tubing in order to switch between evacuating the sliding seal or the inside of the load-lock chamber. The sliding seal contains two Teflon rings used to guide the 7/8" tubing without producing scratches that may result in leaks. The two inner O-rings, held in place by two custom-made brass pieces, provide

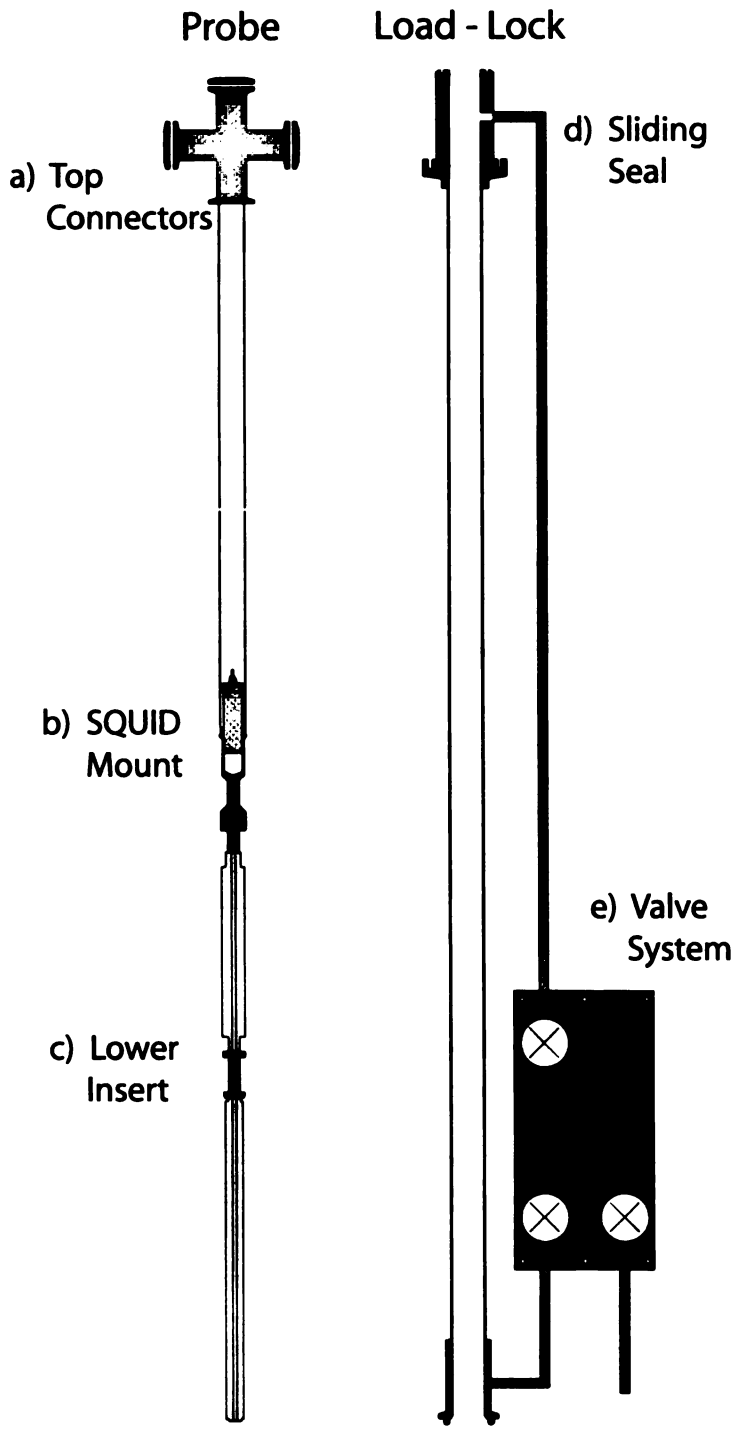

Figure A.1: Dilution refrigerator probe with SQUID capability and load-lock system (not drawn to scale). a) Filters and wire connections. b) SQUID mounting. c) Lower probe to which the experimental wiring and sample are attached. d) Load-lock system with dual sliding seal. e) Gas handling manifold.

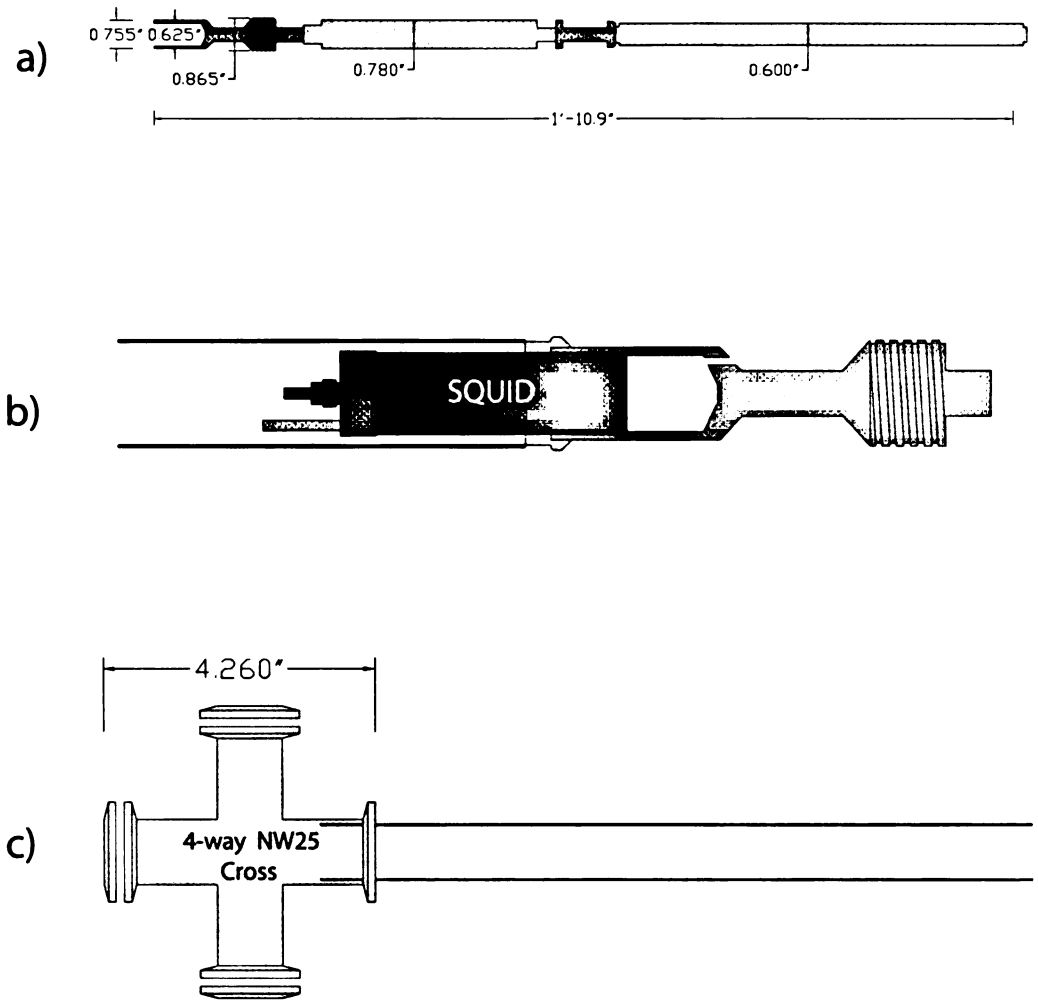

Figure A.2: a) Lower probe dimensions. b) SQUID mounting and connection between lower probe and stainless steel tubing. The wires of the SQUID are directed up the probe. c) Top of the probe made of a 4-way NW25 cross and blanks. Vacuum-compatible connectors can be attached to the NW25 blanks using epoxy.

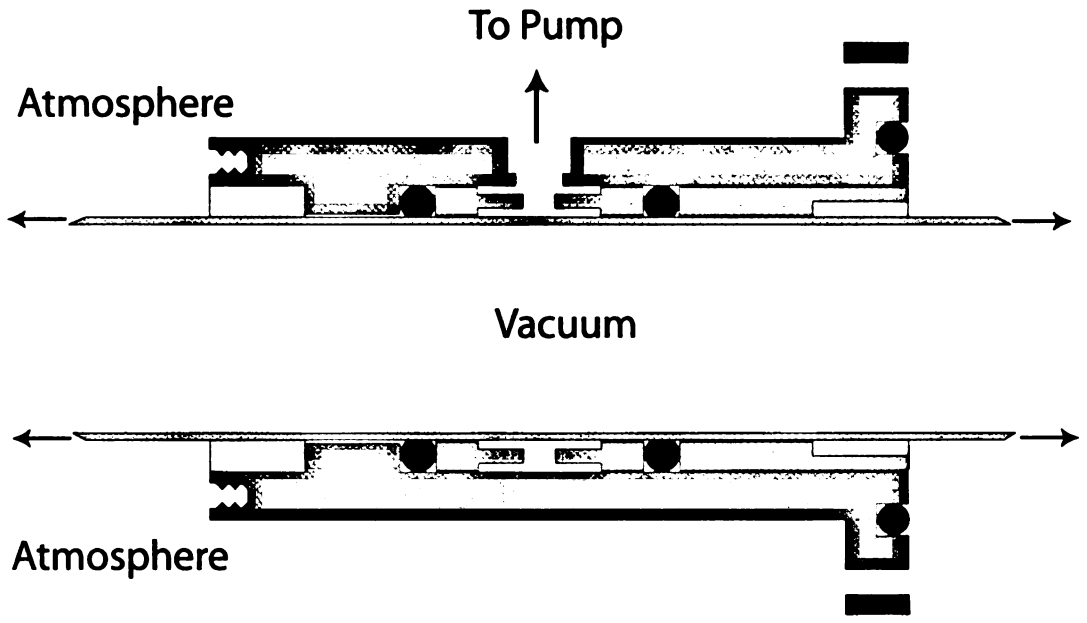

Figure A.3: Load-lock sliding seal. Two O-rings define a volume which isolates the vacuum inside the probe from atmosphere. Any leak into this volume during the loading and unloading process is removed by a vacuum pump.

a volume that isolates the atmosphere from the vacuum. An air leak between the latter spaces will traverse the volume that separates them, and will be pumped away during the loading or unloading process.

A.2 MFM sample holder

Our experiments on magnetic thin films have required the addition of a magnetic field capability to an existing Digital Instruments Atomic Force Microscope (AFM). The AFM is fitted with a magnetic cantilever for measuring magnetic signals from the sample under study. Given the limited space around the sample area, we are unable to implement a Helmholtz coil system. Consequently, we have designed an Al sample holder to rest directly on the current one. The sample holder has a built-in, movable NdFeB rare-earth bar magnet, with dimensions 3/8" x 3/8" x 1". The magnetic field generated at the poles of the magnet are in the plane of the sample, with a range from a few Oe up to 2000 Oe. The sample is attached by double-sided tape to a small piece of Al, which is secured to the large holder by a set screw. Removal of this smaller piece allows for the calibration of the generated magnetic field as a function of the distance, using a Hall probe. The position of the magnet is controlled by a long, threaded screw made of steel, which pushes towards or pulls the magnet away from the sample.

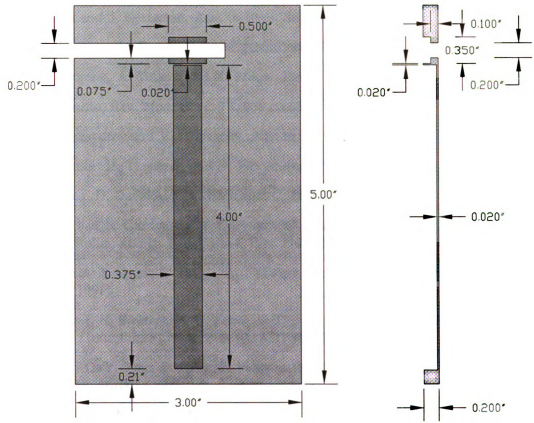

Figure A.4: MFM sample holder with a track for a NdFeB rare-earth bar magnet with dimensions 3/8" x 3/8" x 1". The magnet is brought towards or away from the sample using a long threaded screw. The applied fields range from a few Oe up to 2000 Oe.

References

[1] B. Jin and J. Ketterson, Adv. in Phys. **38**, 189 (1989).

[2] Y. Izyumov, Y. Proshin, and M. Khusainov, Physics-Uspekhi **45**, 109 (2002).

[3] F. Bergeret, A. Volkov, and K. Efetov, Rev. Mod. Phys. **77**, 1321 (2005).

[4] A. Buzdin, Rev. Mod. Phys. **77**, 935 (2005).

[5] I. Kyuksyutov and V. Pokrovsky, Adv. in Phys. **54**, 67 (2005).

[6] J. Hauser, H. Theuerer, and N. Werthamer, Phys. Rev. **142**, 118 (1966).

[7] J. Jiang, D. Davidovic, D. Reich, and C. Chien, Phys. Rev. Lett. **74**, 314 (1995).

[8] T. Mühge, N. Garifyanov, Y. Goryunov, G. Khaliullin, L. Tagirov, K. Westerholt, I. Garifullin, and H. Zabel, Phys. Rev. Lett. **77**, 1857 (1996).

[9] J. Aarts, J. Geers, E. Brück, A. Golubov, and R. Coehoorn, Phys. Rev. B **56**, 2779 (1997).

[10] L. Lazar, K. Westerholt, H. Zabel, L. Tagirov, Y. V. Goryunov, N. Garif'yanov, and I. Garifullin, Phys. Rev. B **61**, 3711 (2000).

[11] J. Gu, C.-Y. You, J. Jiang, J. Pearson, Y. Bazaliy, and S. Bader, Phys. Rev. Lett. **89**, 267001 (2002).

[12] A. Buzdin, Phys. Rev. B **62**, 11377 (2000).

[13] T. Kontos, M. Aprili, J. Lesueur, and X. Grison, Phys. Rev. Lett. **86**, 304 (2001).

[14] B. Josephson, Phys. Lett. **1**, 251 (1962).

[15] L. Bulaevskii, V. Kuzii, and A. Sobyanin, Pis-ma Zh. Eksp. Teor. Fiz. **25**, 314 (1977).

[16] A. Buzdin, L. Bulaevskii, and S. Panyukov, Pis-ma Zh. Eksp. Teor. Fiz. **35**, 147 (1982).

[17] A. Buzdin and M. Kupriyanov, PIs-ma Zh. Eksp. Teor. Fiz. **53**, 308 (1991).

[18] T. Heikkilä, F. Wilhelm, and G. Schön, Europhys. Lett. **51**, 434 (2000).

[19] N. Chtchelkatchev, W. Belzig, and C. Bruder, JETP **74**, 323 (2001).

[20] A. Golubov, M. Kupriyanov, and Y. Fominov, JETP **75**, 588 (2002).

[21] Z. Radović, N. Lazarides, and N. Flytzanis, Phys. Rev. B **68**, 014501 (2003).

[22] V. Ryazanov, V. Oboznov, A. Rusanov, A. Veretennikov, A. Golubov, and J. Aarts, Phys. Rev. Lett. **86**, 2427 (2001).

[23] V. Ryazanov, V. Oboznov, A. Prokof'ev, V. Bolginov, and A. Feofanov, J. Low Temp. Phys. **136**, 385 (2004).

[24] V. Oboznov, V. Bol'ginov, A. Feofanov, V. Ryazanov, and A. Buzdin, Phys. Rev. Lett. **96**, 197003 (2006).

[25] M. Giroud, H. Courtois, K. Hasselbach, D. Mailly, and B. Pannetier, Phys. Rev. B **58**, R11872 (1998).

[26] V. Petrashov, I. Sosnin, I. Cox, A. Parsons, and C. Troadec, Phys. Rev. Lett. **83**, 3281 (1999).

[27] M. Lawrence and N. Giordano, J.Phys: Cond. Matt. **11**, 1089 (1999).

[28] A. Kadigrobov, R. Shekhter, and M. Jonson, J. of Low Temp. Phys. **27**, 760 (2001).

[29] F. Bergeret, A. Volkov, and K. Efetov, Phys. Rev. Lett. **86**, 4096 (2001).

[30] A. Volkov, F. Bergeret, and K. Efetov, Phys. Rev. Lett. **90**, 117006 (2003).

[31] I. Moraru, W. Pratt, and N. Birge, Phys. Rev. Lett. **96**, 037004 (2006).

[32] L. Tagirov, Physica C **307**, 145 (1999).

[33] Y. Fominov, A. Golubov, and M. Kupriyanov, JETP Lett. **77**, 510 (2003).

[34] D. Thouless, Phys. Rep. **13**, 93 (1974).

[35] B. Pannetier and H. Courtois, J. of Low Temp. Phys. **118**, 599 (2000).

[36] R. Soohoo, *Magnetic Thin Films*, 1st ed. (Harper and Row, New York, 1965).

[37] V. Moruzzi, J. Janak, and A. Williams, *Calculated Electronic Properties of Metals* (Pergamon, New York, 1978), p. 168 and 180.

[38] J. Bardeen, L. Cooper, and J. Schrieffer, Phys. Rev. **108**, 1175 (1957).

[39] M. Tinkham, *Introduction to Superconductivity*, 2nd ed. (McGraw Hill Inc, New York, 1996).

[40] P. Gor'kov, JETP **7**, 505 (1958).

[41] N. Kopnin, *Theory of Nonequilibruim Superconductivity*, 1st ed. (Clarendon Press, Oxford, 2001).

[42] G. Eilenberger, Z. Phys. **B214**, 195 (1968).

[43] G. Eliashberg, Zh. Eksp. Teor. Fiz. **61**, 1254 (1971).

[44] A. Larkin and Y. Ovchinnikov, *Nonequilibrium Superconductivity* (Elsevier, Amsterdam, 1984).

[45] K. Usadel, Phys. Rev. Lett. **25**, 507 (1970).

[46] G. Deutscher and P. de Gennes, in *Superconductivity*, edited by R. Parks (Marcel Dekker, Inc., New York, 1969), Vol. 2, p. 1005.

[47] E. Demler, G. Arnold, and M. Beasley, Phys. Rev. B **55**, 15174 (1997).

[48] T. Kontos, Ph.D. thesis, University Paris XI, France, 2001.

[49] S. Guéron, H. Pothier, N. Birge, D. Esteve, and M. Devoret, Phys. Rev. Lett. **77**, 3025 (1996).

[50] M. Houzet, private communication.

[51] J. C. Nabity Nanometer Pattern Generation System, Version 7.4 page 8-2.

[52] W. Jenks, S. Sadeghi, and J. Wikswo, J. Phys D: Appl. Phys. **30**, 293 (1997).

[53] D. Edmunds, W. Pratt, and J. Rowlands, Rev. of Sci. Instr. **51**, 1516 (1980).

[54] L. Tagirov, Phys. Rev. Lett. **83**, 2058 (1999).

[55] A. Buzdin, A. Vedyayev, and N. Ryzhanova, Europhys. Lett. **48**, 686 (1999).

[56] A. Potenza and C. Marrows, Phys. Rev. B **71**, 180503 (2005).

[57] A. Sidorenko, V. Zdravkov, A. Prepelitsa, C. Helbig, Y. Luo, S. Gsell, M. Schreck, S. Klimm, S. Horn, L. Tagirov, and R. Tidecks, Ann. Phys. (Leipzig) **12**, 37 (2003).

[58] J. Nogués and I. Schuller, J. Mag. Mag. Mat. **192**, 203 (1999).

[59] L. Mercaldo, C. A. C. Coccorese, L. Maritato, S. Prischepa, and M. Salvato, Phys. Rev. B **53**, 14040 (1996).

[60] A. Rusanov, M. Hesselberth, J. Aarts, and A. Buzdin, Phys. Rev. Lett. **93**, 057002 (2004).

[61] R. Kinsey, G. Burnell, and M. Blamire, IEEE Trans. App. Supercond. **11**, 904 (2001).

[62] A. Rusanov, S. Habraken, and J. Aarts, cond-mat 0509156 (2005).

[63] S. Steenwyk, S. Hsu, R. Loloee, J. Bass, and W. Pratt, J. of Magn. Magn. Matt. **170**, L1 (1997).

[64] R. Soulen, J. Byers, M. Osofsky, B. Nadgorny, T. Ambrose, S. Cheng, P. Broussard, C. Tanaka, J. Nowak, J. Moodera, A. Barry, and J. Coey, Science **282**, 85 (1998).

[65] L. van der Pauw, Philips Res. Rep. **13**, 1 (1958).

[66] K. Fuchs, Proc. Cambridge Phil. Soc **34**, 100 (1938).

[67] E. Sondheimer, Advan. Phys **1**, 1 (1952).

[68] T. P. Orlando and K. A. Delin, *Foundations of Applied Superconductivity* (Addison Wesley Publishing Company Inc, Reading, 1991).

[69] Z. Radović, L. Dobrosavljević-Grujić, A. Buzdin, and J. Clem, Phys. Rev. B **38**, 2388 (1988).

[70] A. Jani, N. Brener, and J. Callaway, Phys. Rev. B **38**, 9425 (1988).

[71] L. Mattheiss, Phys. Rev. B **1**, 373 (1970).

[72] J. Gu, J. Caballero, R. Slater, R. Loloee, and W. Pratt, Phys. Rev. B **66**, 140507 (2002).

[73] C. Strunk, C. Sürgers, U. Paschen, and H. Löhneysen, Phys. Rev. B **49**, 4053 (1994).

[74] D. Petrovykh, K. Altmann, H. Höchst, M. Laubscher, S. Maat, G. Mankey, and F. Himpsel, Applied Phys. Lett. **73**, 3459 (1998).

[75] J. Connolly, Phys. Rev. **159**, 415 (1967).

[76] C. Fierz, S.-F. Lee, J. Bass, J. W. P. Pratt, and P. A. Schroeder, Journal of Phys: Cond. Matt. **2**, 9701 (1990).

[77] C. Moreau, I. Moraru, W. Pratt, and N. Birge, (manuscript in preparation).

[78] J. Aumentado and V. Chandrasekhar, Phys. Rev. B **64**, 054505 (2001).

[79] W. Belzig, A. Brataas, Y. Nazarov, and G. Bauer, Phys. Rev. B **62**, 9726 (2000).

[80] K. Shigeto, T. Shinjo, and T. Ono, Appl. Phys. Lett. **75**, 2815 (1999).

[81] K. Miyake, K. Shigeto, K. Mibu, T. Shinjo, and T. Ono, J. of Appl. Phys. **91**, 3468 (2002).

[82] G. Beach, C. Nistor, C. Knutson, M. Tsoi, and J. Erskine, Nature **4**, 741 (2005).

[83] M. Tsoi, R. Fontana, and S. Parkin, Appl. Phys. Lett. **83**, 2617 (2003).

[84] C. Faulkner, M. Cooke, D. Allwood, D. Petit, and D. Atkinson, J. of Appl. Phys. **95**, 6717 (2004).

[85] T. Kimura, Y. Otani, I. Yagi, K. Tsukagoshi, and Y. Aoyagi, J. of Magn. Magn. Mat. **272-276**, e1347 (2004).

[86] I. Baladié and A. Buzdin, Phys. Rev. B **67**, 014523 (2003).

[87] C. Bell, E. Tarte, G. Burnell, C. Leung, D.-J. Kang, and M. Blamire, Phys. Rev. B **68**, 144517 (2003).